POLITECNICO DI MILANO

Facoltà di Ingegneria Industriale

Corso di Laurea Magistrale in Ingegneria Aeronautica

Global linear stability of axisymmetric coaxial jets

Relatore: Prof. Franco AUTERI
Co-relatore: Dr. Marco CARINI

Tesi di laurea di:
Jacopo CANTON
Matr. 787629

Anno Accademico 2012 - 2013

Abstract

This work is concerned with the numerical investigation of the stability properties of two viscous, incompressible, coaxial jets. Starting from a Finite Element base flow solver, the necessary tools for a linear analysis are developed and thoroughly validated. A Hopf bifurcation point is located in the parameter space, and its neutral curve is traced in the Reynolds number-velocity ratio plane, thus allowing to compute the minimum values of the parameters necessary for the onset of the linear instability. In the unstable regime, for a unitary velocity ratio, a von Kármán vortex-street is originated in the wake of the duct wall separating the two streams. In this condition the eigenvectors and the structural sensitivity parameter associated with the critical eigenvalue closely resemble those observed in flows around bluff bodies. When the velocity ratio is increased, the vortex dynamics tends more and more to the one produced by a Kelvin–Helmoltz instability. In this configuration the shape of the unstable eigenmode is altered, and the structural sensitivity parameter clearly highlights a modification of the region where the 'wavemaker' is located. In addition, the results show that large transient growth may occur in the subcritical regime, amplifying the kinetic energy of perturbations by up to twelve orders of magnitude. This research is completed by a study on the influence of domain truncation, a relevant issue in weakly nonparallel flows, and by a comparison with the results obtained by DNS.

Keywords: Coaxial jets, Navier–Stokes equations, Modal stability, Hopf bifurcation, Nonmodal stability, Structural sensitivity.

Sommario

Questo lavoro si occupa dell'analisi numerica delle proprietà di stabilità di una coppia di getti coassiali incomprimibili e viscosi in funzione del numero di Reynolds associato al getto interno e del rapporto fra le velocità massime nei due getti all'ingresso del dominio. Partendo da un solutore agli Elementi Finiti per il calcolo del flusso base, vengono sviluppati e validati gli strumenti necessari per un'analisi lineare della corrente. Viene individuato, nello spazio dei parametri, un punto di biforcazione di Hopf, la cui curva neutra viene tracciata nel piano numero di Reynolds-rapporto di velocità, permettendo di calcolare i valori minimi dei parametri necessari per l'instabilità lineare. In regime instabile, per un rapporto di velocità unitario, una scia di von Kármán ha origine a valle del setto che separa i due condotti di ingresso. In questa configurazione gli autovettori ed il parametro di sensitività strutturale associati all'autovalore marginalmente stabile assomigliano a quelli osservati nella scia di corpi tozzi. Quando il rapporto di velocità viene incrementato, la dinamica degli anelli vorticosi tende a quella prodotta da un'instabilità di Kelvin–Helmoltz, la forma dell'autovettore critico viene modificata ed il parametro di sensitività strutturale evidenzia un sensibile mutamento della regione ove ha sede il meccanismo di instabilità. Inoltre, i risultati mostrano che un'ampia crescita transitoria può aver luogo in regime subcritico, e che l'energia cinetica delle perturbazioni può essere amplificata fino a dodici ordini di grandezza. L'indagine viene completata da uno studio sull'influenza del troncamento del dominio, un aspetto importante per le correnti debolmente non parallele, e da un confronto con i risultati ottenuti tramite DNS.

Keywords: Getti coassiali, Equazioni di Navier–Stokes, Stabilità modale, Biforcazione di Hopf, Stabilità non modale, Sensitività strutturale.

to Agnese

I would like to thank my supervisor, Prof. F. Auteri, for the constant support and his invaluable knowledge. I'm indebted to Dr. M. Carini for the numerous discussions and the help he gave me when I was writing the code. I'm also grateful to Prof. L. Quartapelle for the illuminating advices and his teachings on the art of writing with LaTeX. Finally, I owe my family for supporting me during my studies.

Contents

Introduction

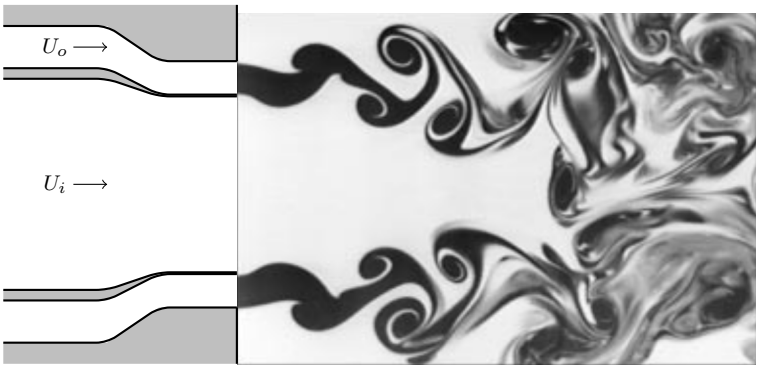

Figure 0.1 *Flow visualization taken from [46]. The annular jet is seeded with a fluorescent die, the velocity ratio is $r_u = U_o/U_i = 4$ and the Reynolds number based on the inner jet is $Re_i = 1\,000$.*

Coaxial jets are generated when combining two streams: an inner one, originating from a circular pipe of diameter D_i and flowing at velocity U_i, and an outer one, issuing from an annular-section pipe of diameters $D_{o,1}$ and $D_{o,2}$ and flowing at velocity U_o. Annular jets correspond to the case when there is no inner fluid stream, namely, $U_i = 0$, and, depending on the application, the wall separating the jets may be reduced to a sharp edge so that $D_{o,1} = D_i$, as depicted in figure 0.1. The two streams need not have the same fluid properties, however, the present investigation is restricted to the case of identical fluids and uniform temperature.

Coaxial jet flows are often used in industrial applications as an effective way of mixing two different fluid streams: important examples are found in the fuel-air mixing process which takes place inside jet engines, as well as in the gas assisted spray formation, known as airblast atomization. In fact, the coaxial jets flow, operating with a large outer to inner momentum ratio

is used for its ability to destabilize, fragment and mix the central stream in the outer, rapid stream [46]. Furthermore, much aeronautical interest lies in the noise reduction characteristics achievable by coaxial jets. The effect of noise reduction by the addition of a surrounding coaxial stream to a single jet has been known for several years (see, for instance, [49]). In particular, it has been suggested [31, 19] that the aerodynamic noise produced by coaxial jets is related to the dynamics of large-scale vortical structures generated by the instability of the shear layers; moreover, it is well known (see, *e.g.* [27]) that large scale mixing is controlled by coherent structures of relevant size. It is therefore very important to understand the detailed dynamics of these structures, even in simple flow configurations (*i.e.*, constant density and low Reynolds numbers).

Despite its relatively simple configuration, the coaxial jets flow is governed by eleven independent quantities, which are functions of both nozzle geometry and fluid properties. The present investigation is limited to the case of non-swirling, viscous, incompressible jets separated by a duct wall of rectangular geometry, and thus accounts for four parameters only, reported in table 0.1. As a consequence of the noteworthy number of involved parameters, coaxial jets allow to study the onset of turbulence beyond a description based on the Reynolds number alone.

$\mathrm{Re}_i = \dfrac{U_{0i} D_i}{\nu}$	Reynolds number of the central jet
$r_u = \dfrac{U_{0o}}{U_{0i}}$	velocity ratio
$\beta = \dfrac{D_{o,2}}{D_i}$	diameter ratio
$s = R_{o,1} - R_i$	height of the separation wall

Table 0.1 *Governing parameters.*

The stability properties of this class of flows have been investigated experimentally by several authors [3, 37, 38, 39] in various geometrical configurations and for different values of the aforementioned parameters. Based on experimental measurements and analytical inviscid approximation [26, 41], these authors have argued that, in the case of a thick wall separating the nozzles, coaxial jets present a locally absolutely unstable region immediately downstream of this wall. This region is responsible for the oscillator-type behaviour of the flow which is rather insensitive to external perturbations. One of the objectives of the present investigation is to further contribute to these assessments and to characterize the jets from the stability point of view.

The existence of two shear layer regions, one between the inner jet and the outer jet, and the other between the outer jet and the surrounding quiescent medium, was highlighted by Ko and Kwan [20, 22]; these authors measured two different frequency peaks, corresponding to the presence of vortices originated from the inner and outer shear layers. They also observed the formation of two potential cores[1], separated by the inner shear layer.

The complex interaction of the instabilities originating from the shear layers have been initially documented in [8] and [46]. These articles evidence the importance of the outer to inner velocity ratio $r_u = U_o/U_i$. In addition Rehab et al. [30] have determined the existence of a critical value r_{uc}, lying in the range $5 < r_{uc} < 8$ and depending on the inflow velocity profiles, above which a reverse flow region develops within the inner jet.

For $r_u \ll 1$, the outer stream acts mainly as a "coflow", without modifying substantially the inner jet dynamics [10] nor the main instability, which is driven by inner shear layer [37].

For larger, but still less than 1, velocity ratios ($0.59 < r_u < 0.71$) the outer shear layer instability rolls up into axisymmetric vortex rings that turn further downstream into a helical-shaped structure. The inner shear layer, on the other hand, has a lethargic behaviour and never rolls up into vortical structures before being dominated by the outer helical vortices [7].

At $r_u \approx 1$ a pattern similar to that of the von Kármán vortex street develops behind the wall separating the nozzles; the blunt-edge wake instability is found to be the dominant mechanism affecting both the inner and the outer shear layers [37].

For large velocity ratios ($r_u > 2.56$) the inner shear layer also rolls up into ring-shaped vortices which interact with the outer vortex structures. In this case the outer shear layer dominates the dynamics of the flow by forcing the inner shear layer and leading to a characteristic lock-in phenomenon [7].

For velocity ratios above the critical value, the inner potential core is truncated and a large recirculating bubble, having a size of the order of the inner jet diameter, is formed a few diameters downstream of the nozzles. A characteristic feature of this backflow region is the fact that it oscillates and rotates at the same frequency in a pure precession mode, this frequency is fixed by D_i and U_i [30].

The influence of the separation wall has been thoroughly studied in the experiments performed by Segalini [37]. The wake produced by a wall of relevant height ($s \approx D_i/10$) affects the flow for intermediate velocity ratios, showing a maximum effect for $r_u \approx 1$. In this regime the wake instability is responsible for the main fluctuations in the flow field.

[1]Here "potential" denotes a region of low turbulence, not irrotationality.

Based on the above cited experimental results, the present work is aimed at investigating the coaxial jets flow by means of a global stability analysis. The main purpose is indeed to provide useful information for the understanding of the origin of the various documented regimes and of the underlying physical mechanism of instability.

Different approaches, whose theoretical foundations are presented in Chapter 1, have been adopted to tackle the problem. Details of their numerical implementation are given in Chapter 2, while Chapter 3 is devoted to a thorough validation of the developed software with different geometries and flows. Finally, Chapter 4 presents the study of the behaviour and stability characteristics of coaxial jets with respect to the parameters describing the flow. The flow is approximated as incompressible and axisymmetric and, as already mentioned, the fluid dynamic properties of the inner and annular jets are considered identical. The assumption of axisymmetry is justified at least in the initial jets region since it has been observed from the experiments [8, 30] that the structures developing from the rollup of the two shear layers remain axisymmetric over a distance of a few diameters.

The numerical tools employed in this thesis have been implemented in a program written in Fortran 2003 and C programming languages starting from a Finite Element code provided by Prof. Quartapelle. The most computational intensive parts, *i.e.*, the matrix operations and the solution of linear systems, have been parallelized using the MPI and OpenMP libraries.

CHAPTER 1

Problem formulation

This Chapter provides some basic elements of the theory of nonlinear dynamical systems. Moreover, the abstract formulation of the mathematical problems occurring in the present investigation is introduced, following, amongst many, [21, 17, 44].

1.1 Dynamical system theory

Consider a dynamical system given by the triple $\{T, H, \mathcal{S}(t)\}$, where T is a *time set*, H is a *phase (or state) space*, and $\mathcal{S}(t) : H \to H$ is a *family of evolution operators* parametrized by $t \in T$ and satisfying the following semigroup properties:

$$\mathcal{S}(0) = \mathcal{I}$$
$$\mathcal{S}(t+s) = \mathcal{S}(t) \circ \mathcal{S}(s) \quad \textit{i.e.}, \text{ the system is } \textit{autonomous}.$$

In the continuous-time case, the action of the evolution operator $\mathcal{S}(t)$ on a state $\boldsymbol{x}_0 \in H$ can be described by the solution of a (partial) differential equation with initial conditions of the form:

$$\begin{cases} \dfrac{\partial \boldsymbol{x}}{\partial t} + \mathcal{N}(\boldsymbol{x}; \boldsymbol{\lambda}) = 0, \\ \boldsymbol{x}(\boldsymbol{r}, 0) = \boldsymbol{x}_0(\boldsymbol{r}). \end{cases} \tag{1.1}$$

The solution $\boldsymbol{x} = \boldsymbol{x}(\boldsymbol{r}, t)$ belongs to the phase space H, and $\mathcal{N}$, which does not explicitly depend on time, the system being autonomous, is a family of

mappings of H into itself depending on the (vector) parameter $\boldsymbol{\lambda}$; in all the applications considered here, $\mathcal{N}$ represents the steady, incompressible Navier–Stokes equations, to be presented in section 1.4.1. In infinite dimensions the phase space H is a function space, for instance a Hilbert space, whilst in finite dimensions $H \subset \mathbb{R}^d$ ($d \in \mathbb{N}$).

When considering a deterministic system, *i.e.*, a system that will always lead to the same state when starting from a given initial condition, the knowledge of $\boldsymbol{x} = \boldsymbol{x}(\boldsymbol{r}, t)$ allows a complete description of the state of the system at any given time.

From the engineering point of view the interest lies in understanding the behaviour of the system both as $t \to \infty$ as well as during a "small" transient period.

As the observed phenomena depend on $\boldsymbol{\lambda}$, in a very schematic way, and considering as the sole parameter Re, the typical evolution of a fluid dynamic system can be described as follows:

Step 1. For small Re, say $\mathrm{Re} < \mathrm{Re}_1$, there exists a unique steady solution to the equation

$$\mathcal{N}(\boldsymbol{x}; \mathrm{Re}) = 0, \tag{1.2}$$

i.e., a unique fixed point $\boldsymbol{x} = \boldsymbol{s}_1(\boldsymbol{r})$. This steady solution is stable and attracts all the orbits, which means that

$$\boldsymbol{x}(\boldsymbol{r}, t) \to \boldsymbol{s}_1(\boldsymbol{r}) \quad \text{as} \quad t \to \infty,$$

for any $\boldsymbol{x}_0 \in H$.

Step 2. For larger values of Re, say $\mathrm{Re}_1 < \mathrm{Re} < \mathrm{Re}_2$, other solutions to (1.2) appear, while $\boldsymbol{s}_1$ loses its stability. At this point there are two possible scenarios:

(i) if other steady solutions $\boldsymbol{s}_2, \boldsymbol{s}_3, \ldots$, appear, a steady state bifurcation has occurred at $\mathrm{Re} = \mathrm{Re}_1$. Typically, for $t \to \infty$, $\boldsymbol{x}$ will converge to one of the steady solutions

$$\boldsymbol{x}(\boldsymbol{r}, t) \to \boldsymbol{s}_i(\boldsymbol{r}) \quad \text{for some } i \neq 1, \text{ as} \quad t \to \infty,$$

with i depending on $\boldsymbol{x}_0$. Each steady solution possesses a basin of attraction, *i.e.*, the set of all initial conditions which evolve towards the considered steady solution, and attracts all the solutions of (1.1) that start from within such a set.

(ii) Otherwise a Hopf bifurcation can occur: in this case, the flow never becomes steady. Instead, if the bifurcation is supercritical, the evolution of

the system will be determined by

$$\boldsymbol{x} - \boldsymbol{\phi} \to 0 \quad \text{as} \quad t \to \infty,$$

where $\boldsymbol{\phi} = \boldsymbol{\phi}(\boldsymbol{r}, t)$ is a *time-periodic* solution of (1.1), of period $\tau > 0$

$$\begin{cases} \dfrac{\partial \boldsymbol{\phi}}{\partial t} + \mathcal{N}(\boldsymbol{\phi}, \mathrm{Re}) & = 0, \quad \forall t \in \mathbb{R}^+, \\ \boldsymbol{\phi}(\boldsymbol{r}, t + \tau) & = \boldsymbol{\phi}(\boldsymbol{r}, t). \end{cases} \tag{1.3}$$

The value Re_1 where the bifurcation has occurred is a priori unknown, as is the solution $\boldsymbol{\phi}$ of (1.3) and even the period τ. In every instance, a detailed analysis is necessary to determine these quantities.

Indicating with $\boldsymbol{x}_1$ the value of $\boldsymbol{x}(\boldsymbol{r}, t)$ for which $\mathrm{Re} = \mathrm{Re}_1$, the couple $(\boldsymbol{x}_1, \mathrm{Re}_1)$ is called a *bifurcation point*. This is the first step that eventually leads to turbulence when approached from the dynamical systems point of view as pictured in the Ruelle–Takens route to chaos, [32]. Gallavotti [13] suggests that:

"We can audaciously hope that in the future the phenomena that appear at the onset of turbulence can become the blocks with which to construct the theory of "strong" turbulence, with many degrees of freedom. The possibility of this viewpoint emerged after the works of Ruelle–Takens and it seems supported by a large amount of experimental and theoretical checks."

This is an important motivation to the present investigation.

1.2 Bifurcation theory

As parameters are varied, changes, as the one depicted in the previous section, may occur in the qualitative structure of the solutions. These changes are called *bifurcations* and the parameter values at which they occur are called *bifurcation values*; in these points the system is said to be *structurally unstable*. The phase portrait of the dynamical system qualitatively changes when passing through a bifurcation point. More precisely the two phase portraits, separated by the bifurcation, are not *topologically equivalent*; this means that there is no homeomorphism that can map the orbits of the phase portrait before the bifurcation to those of the phase portrait after the bifurcation, preserving the direction of time [21].

The *codimension* of a bifurcation is the smallest dimension of the parameter space which contains the bifurcation in a persistent way, or, equivalently, it is the difference between the dimension of the parameter space and the dimension of the corresponding bifurcation boundary. There are four types of codimension one bifurcations: three of them are characterized by a real

eigenvalue that vanishes at the bifurcation point, this kind of bifurcation characterizes *Step 2*i; the fourth type has two complex conjugate eigenvalues which cross the imaginary axis, and it characterizes *Step 2*ii.

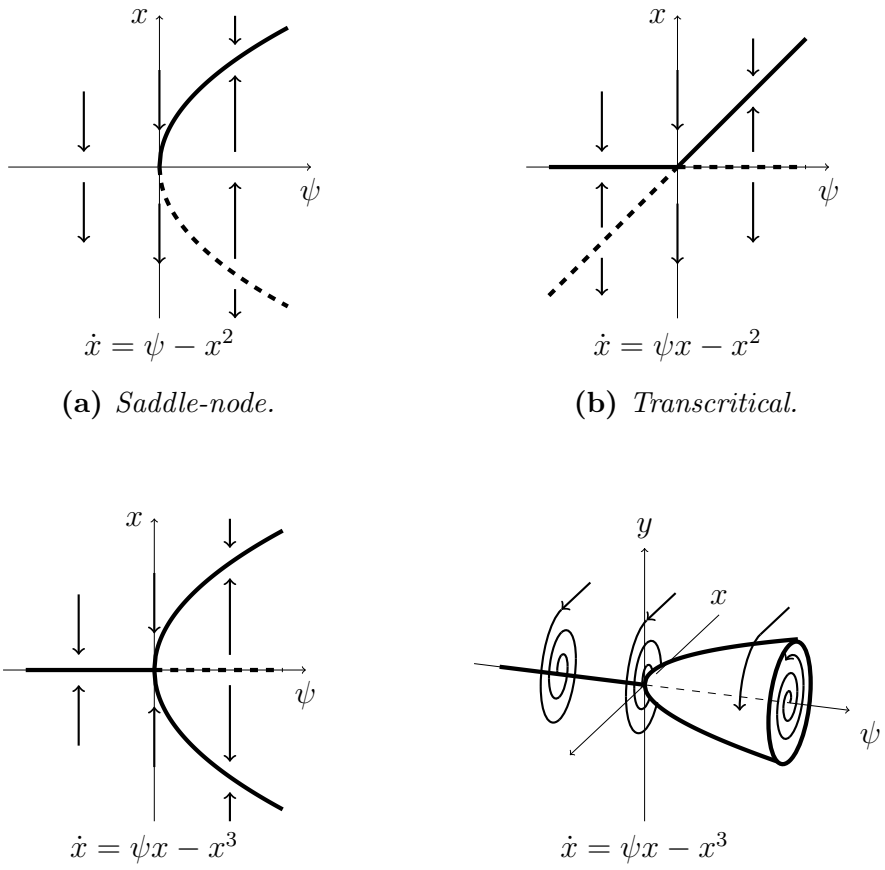

(a) *Saddle-node.* **(b)** *Transcritical.*

(c) *Pitchfork.* **(d)** *Supercritical Hopf.*

Figure 1.1 *Examples of codimension one bifurcation diagrams.*

A well known example is the flow around a circular cylinder which exhibits a Hopf bifurcation as first instability.

1.3 Navier–Stokes equations

Throughout this thesis the dynamical system of eq. (1.1) will be identified as the Navier–Stokes equations for an incompressible fluid of uniform density which can be written, in the standard convective form, as

$$\begin{cases} \dfrac{\partial \boldsymbol{u}}{\partial t} + (\boldsymbol{u}\cdot\boldsymbol{\nabla})\boldsymbol{u} - \dfrac{1}{\mathrm{Re}}\nabla^2\boldsymbol{u} + \boldsymbol{\nabla}p = 0, \\ \boldsymbol{\nabla}\cdot\boldsymbol{u} = 0, \end{cases} \tag{1.4}$$

where $\boldsymbol{u}(\boldsymbol{r},t)$ is the velocity vector with components $\boldsymbol{u} = (u_x, u_y, u_z)$, in Cartesian coordinates, and $\boldsymbol{u} = (u_r, u_\theta, u_z)$ in cylindrical coordinates; the (dimensionless) pressure has been rescaled dividing it by the Reynolds number Re. The equations are made dimensionless by choosing a characteristic length scale D^* and a reference velocity U^*, depending on the flow being investigated, which allow to define the Reynolds number

$$\mathrm{Re} = \frac{U^* D^*}{\nu^*}, \tag{1.5}$$

where ν^* is the kinematic viscosity of the fluid, assumed to be constant.

The problem is set on a finite domain Ω whose boundary is divided in two parts, $\partial\Omega = \Gamma_D \cup \Gamma_N$, to assign different boundary conditions on each Γ_i, as explained in the following section.

1.4 Linearized equations

The starting point of the linear stability analysis, whether modal or nonmodal, is the linearization of the Navier–Stokes equations in the neighbourhood of a fixed point $\boldsymbol{X} = (\boldsymbol{U}, P)$. The velocity and pressure fields are then considered as the linear combination of two fields, *i.e.*, $\boldsymbol{u} = \boldsymbol{U} + \boldsymbol{u}'$ and $p = P + p'$ which, substituted into the Navier–Stokes equations (1.4), lead to two systems of equations: one that describes the fixed point and one for the perturbation fields.

1.4.1 Base flow

The computation of the base flow, which is a fixed point for (1.4), involves the numerical solution of the steady-state Navier–Stokes equations. The problem can be stated in strong form as:

find a velocity field $\boldsymbol{U}(\boldsymbol{r})$ *and a pressure field* $P(\boldsymbol{r})$, *defined up to an additive constant, such that:*

$$\begin{cases} (\boldsymbol{U}\cdot\boldsymbol{\nabla})\boldsymbol{U} - \dfrac{1}{\mathrm{Re}}\nabla^2\boldsymbol{U} + \boldsymbol{\nabla}P = 0, \\ \boldsymbol{\nabla}\cdot\boldsymbol{U} = 0, \\ \boldsymbol{U} = \boldsymbol{b}, & \forall \boldsymbol{r} \in \Gamma_D; \\ \dfrac{1}{\mathrm{Re}}\dfrac{\partial \boldsymbol{U}}{\partial \hat{\boldsymbol{n}}} - P\hat{\boldsymbol{n}} = \boldsymbol{a}, & \forall \boldsymbol{r} \in \Gamma_N; \end{cases} \tag{1.6}$$

where $\hat{\boldsymbol{n}}$ is the outward pointing normal, $\boldsymbol{b}(s)$ and $\boldsymbol{a}(s)$ are assigned vector functions, and Γ_D and Γ_N are portions of the boundary $\partial\Omega$ such that $\Gamma_D \cup \Gamma_N = \partial\Omega$ and $\mathring{\Gamma}_D \cap \mathring{\Gamma}_N = \emptyset$, where the circle $\mathring{\cdot}$ indicates the inner portion of a set.

The boundary condition on Γ_D is of Dirichlet type and assigns all the velocity components (but it does not involve the pressure); on the other hand, the boundary condition on Γ_N is of Neumann type and is equivalent to a stress-free boundary condition only on still, solid surfaces.

The expression of the viscous stresses, relative to a surface with generic normal, is in fact (see [29]):

$$\boldsymbol{s}_{\hat{\boldsymbol{n}}}(\boldsymbol{u}) = \bar{\mu}[2(\hat{\boldsymbol{n}}\cdot\nabla)\boldsymbol{u} + \hat{\boldsymbol{n}} \times \boldsymbol{\nabla}\times\boldsymbol{u}],$$

which, only in the case of a non moving, rigid body can be simplified to:

$$\boldsymbol{s}|_{\text{n.m.b.}} = \bar{\mu}(\hat{\boldsymbol{n}}\cdot\nabla)\boldsymbol{u}|_{\text{n.m.b.}},$$

which, in turn, means that the total stresses on a still, solid surface are:

$$\boldsymbol{t}|_{\text{n.m.b.}} = [\bar{\mu}(\hat{\boldsymbol{n}}\cdot\nabla)\boldsymbol{u} - p\hat{\boldsymbol{n}}]|_{\text{n.m.b.}},$$

but this expression is not valid on a generic border of the domain.

1.4.2 Direct and adjoint LNSE

After dropping nonlinear terms, the equations for the perturbation, known as Linearized Navier–Stokes Equations (LNSE), read:

find a velocity field $\boldsymbol{u}'(\boldsymbol{r},t)$ *and a pressure field* $p'(\boldsymbol{r},t)$*, defined up to an additive constant, such that:*

$$\begin{cases} \dfrac{\partial \boldsymbol{u}'}{\partial t} + (\boldsymbol{U}\cdot\boldsymbol{\nabla})\boldsymbol{u}' + (\boldsymbol{u}'\cdot\boldsymbol{\nabla})\boldsymbol{U} - \dfrac{1}{\mathrm{Re}}\nabla^2\boldsymbol{u}' + \boldsymbol{\nabla}p' = 0, \\ \boldsymbol{\nabla}\cdot\boldsymbol{u}' = 0, \\ \boldsymbol{u}' = \boldsymbol{b}, \qquad\qquad \forall \boldsymbol{r} \in \Gamma_D; \\ \dfrac{1}{\mathrm{Re}}\dfrac{\partial \boldsymbol{u}'}{\partial \hat{\boldsymbol{n}}} - p'\hat{\boldsymbol{n}} = \boldsymbol{a}, \qquad \forall \boldsymbol{r} \in \Gamma_N; \end{cases} \tag{1.7}$$

supplemented by the initial condition $\boldsymbol{u}'(\boldsymbol{r},0) = \boldsymbol{u}'_0(\boldsymbol{r})$. Typical boundary conditions impose a null velocity perturbation on solid walls $\boldsymbol{u}'(\boldsymbol{r},t)|_{\Gamma_w} = 0$, and decaying perturbations at infinity.

The adjoint linearized Navier–Stokes system of equations is obtained from the direct one by multiplying it by two test functions, $\boldsymbol{v}'$ and q', and integrating by parts. After standard mathematical manipulation, the adjoint LNSE read:

find a velocity field $\boldsymbol{v}'(\boldsymbol{r},t)$ *and a pressure field* $q'(\boldsymbol{r},t)$*, defined up to an additive constant, such that:*

$$\begin{cases} \dfrac{\partial \boldsymbol{v}'}{\partial t} + (\boldsymbol{U}\cdot\boldsymbol{\nabla})\boldsymbol{v}' - (\boldsymbol{\nabla}\boldsymbol{U})\cdot\boldsymbol{v}' + \dfrac{1}{\mathrm{Re}}\nabla^2\boldsymbol{v}' + \boldsymbol{\nabla}q' = 0, \\ \boldsymbol{\nabla}\cdot\boldsymbol{v}' = 0, \\ \boldsymbol{v}' = \boldsymbol{b}, \qquad\qquad \forall \boldsymbol{r} \in \Gamma_D; \\ \dfrac{1}{\mathrm{Re}}\dfrac{\partial \boldsymbol{v}'}{\partial \hat{\boldsymbol{n}}} - q'\hat{\boldsymbol{n}} = \boldsymbol{a}, \qquad \forall \boldsymbol{r} \in \Gamma_N; \end{cases} \tag{1.8}$$

supplemented by the initial condition $\boldsymbol{v}'(\boldsymbol{r},0) = \boldsymbol{v}'_0(\boldsymbol{r})$.

1.5 Modal stability

As a first step in the investigation of the behaviour of a dynamical system in the neighbourhood of a fixed point, the study of the stability properties of the linearized system allows the determination of its local characteristics. Lyapunov's theorem states that an equilibrium point $\boldsymbol{X}$ for equation (1.1) is *asymptotically stable* if all the eigenvalues of the Jacobian matrix of the

system, *i.e.*, $\mathcal{J}|_{\boldsymbol{X}} = \nabla_{\boldsymbol{x}}\mathcal{N}(\boldsymbol{X})$, have a strictly negative real part. This, though, simply means that the system is stable to infinitesimal perturbations, and does not account for finite amplitude perturbations which could render the flow unstable.

The modal (or normal[1]) stability properties of the system are investigated by computing the eigenfunctions of the linearized problem in the neighbourhood of the fixed point $\boldsymbol{X}$. The objective of this analysis is to describe the instability, the shape of the unstable modes and to find out where the instability mechanism is located in the flow field (*structural sensitivity analysis*, which will be explained in section 1.6). Moreover, after computing the most unstable modes, the hyperbolicity of the fixed point can be ascertained[2] and in the event of a bifurcation point, the kind of the bifurcation can be determined.

The starting point of the modal stability analysis is the computation of the fixed point $\boldsymbol{X} = (\boldsymbol{U}, P)$, whose stability is to be investigated. Once the base flow has been computed, the second step consists in the solution of the linearized problem (1.7); under the assumption of normal modes, the velocity and pressure perturbations can be written as

$$\boldsymbol{u}'(\boldsymbol{r},t) = e^{\lambda t}\hat{\boldsymbol{u}}(\boldsymbol{r}), \qquad p'(\boldsymbol{r},t) = e^{\lambda t}\hat{p}(\boldsymbol{r}),$$

the direct LNSE result in the following non-symmetric generalized eigenvalue problem in the unknowns λ_j, $\hat{\boldsymbol{u}}_j$ and $\hat{p}_j$:

$$\begin{cases} \lambda_j\hat{\boldsymbol{u}}_j + (\boldsymbol{U}\cdot\boldsymbol{\nabla})\hat{\boldsymbol{u}}_j + (\hat{\boldsymbol{u}}_j\cdot\boldsymbol{\nabla})\boldsymbol{U} - \dfrac{1}{\mathrm{Re}}\nabla^2\hat{\boldsymbol{u}}_j + \boldsymbol{\nabla}\hat{p}_j = 0, \\ \boldsymbol{\nabla}\cdot\hat{\boldsymbol{u}}_j = 0, \end{cases} \tag{1.9}$$

where λ_j is the eigenvalue and $\hat{\boldsymbol{x}}_j = (\hat{\boldsymbol{u}}, \hat{p})_j$ is the eigenfunction of the direct problem.

To perform the structural sensitivity analysis, the adjoint eigenfunctions are also needed, therefore the adjoint eigenvalue problem is here introduced. Starting from the adjoint linearized Navier–Stokes equations (1.8), and repeating the same steps used for the direct one, the corresponding eigenvalue problem is easily obtained and reads:

$$\begin{cases} -\lambda_j\hat{\boldsymbol{v}}_j + (\boldsymbol{U}\cdot\boldsymbol{\nabla})\hat{\boldsymbol{v}}_j - (\boldsymbol{\nabla}\boldsymbol{U})\cdot\hat{\boldsymbol{v}}_j + \dfrac{1}{\mathrm{Re}}\nabla^2\hat{\boldsymbol{v}}_j + \boldsymbol{\nabla}\hat{q}_j = 0, \\ \boldsymbol{\nabla}\cdot\hat{\boldsymbol{v}}_j = 0. \end{cases} \tag{1.10}$$

[1] As pointed out by Trefethen and Embree (see [44]) it was a mistake, during the past century, to use the terms "linear stability analysis" and "eigenvalue analysis" with the same meaning; confusing the two, in fact, leaves no room for nonnormal linear effects.

[2] An hyperbolic fixed point is a point where the system has no eigenvalues on the imaginary axis.

where, again, λ_j is the eigenvalue and $\hat{\boldsymbol{y}}_j = (\hat{\boldsymbol{v}}, \hat{q})_j$ is the eigenfunction of the adjoint problem. As for the direct problem, the adjoint velocity eigenfunctions satisfy homogeneous Dirichlet boundary conditions on solid walls, and decay at infinity.

After the problem discretisation, the resulting finite dimensional linear operators can be represented by matrices; the adjoint of a finite dimensional linear operator is the Hermitian matrix (conjugate transposed matrix), a property which greatly simplifies the computation of the adjoint modes; this approach is illustrated in sections 2.1.2 and 2.3.

1.6 Structural sensitivity

The structural sensitivity analysis is a relatively new technique, first proposed in 2007 [15]. What motivates it is that the region where the instability mechanism acts cannot be identified from the study of the direct and adjoint eigenfunctions separately. This is because, in general, there is quite a large difference in the spatial structure of the direct and adjoint modes. The aim of this analysis is thus to investigate in what region of the flow field the 'wavemaker' is located, more precisely, where in space a modification in the structure of the problem, represented by a localized velocity feedback, is able to produce the greatest drift of the least stable eigenvalue. This, in fact, is the 'core' of the instability mechanism. Note that the sensitivity of the eigenvalue (and in general of the entire spectrum) depends on the level of non-normality of the linear operator used for the discretization of the problem [5].

The idea is that, as the eigenvalue problem depends on the fixed point $\boldsymbol{X}$ being investigated, the introduction of a perturbation to the base flow modifies both eigenvalues and eigenvectors. The use of spatially localized perturbations allows then to find the most sensitive region of the flow, simply by studying how the eigenvalue problem is modified by the perturbation.

The mathematical steps, that lead to the definition of a measure function, start from the knowledge of the base flow to be investigated, $\boldsymbol{X} = (\boldsymbol{U}, P)$, and its direct and adjoint eigenvalue problems. By introducing a perturbation to the base flow, *i.e.*, $\boldsymbol{U} \leftarrow \boldsymbol{U} + \tilde{\boldsymbol{U}}$ and $P \leftarrow P + \tilde{P}$, the eigenvalue problem has to be modified by substituting the perturbed quantities: $\lambda_i + \tilde{\lambda}_i$, $\hat{\boldsymbol{u}}_i + \hat{\tilde{\boldsymbol{u}}}_i$ and $\hat{p}_i + \hat{\tilde{p}}_i$. After a few manipulations and thanks to the adjoint eigenvalue problem, the conclusion is that the linearized system is most sensitive to perturbations represented by a spatially localized feedback located in the maximum(a) of the function

$$s(\boldsymbol{r}) = \frac{\|\hat{\boldsymbol{v}}_i(\boldsymbol{r})\| \; \|\hat{\boldsymbol{u}}_i(\boldsymbol{r})\|}{|\int_\Omega \hat{\boldsymbol{v}}_i \cdot \hat{\boldsymbol{u}}_i|}, \tag{1.11}$$

here referred to as *structural sensitivity parameter* [15].
($\hat{\boldsymbol{u}}_i$ and $\hat{\boldsymbol{v}}_i$ are the velocity parts of the eigenvectors of the direct and adjoint eigenvalue problems presented in (1.9) and (1.10)).

1.7 Transient growth

The second kind of linear analysis adopted in the present investigation is the study of *transient growth* of initial perturbations near the fixed point. This technique may be necessary because sometimes, even for a modally stable flow, some perturbations can take the flow out of the basin of attraction of the fixed point [35]; or, more generally, because if a problem is far from normal, conclusions based on eigenvalues may not be robust [44].

Hydrodynamic instability mechanisms have been investigated, for decades, by linearizing the Navier–Stokes equations and testing for unstable eigenvalues of the linearized problem. The results of such investigations, in many cases, agree poorly with experiments. The usual simplification in these stability calculations is the assumption of an exponential time dependence, also referred to as the normal-mode approach. This ansatz allows the transformation of the linear initial-value problem into a corresponding eigenvalue problem, as seen in section 1.5. It is a fact of linear algebra, though, that even if all the eigenvalues of a linear system are distinct and lie well inside the $\mathbb{R}^-$ half-plane, inputs to that system may be amplified by arbitrarily large factors if the eigenfunctions are not orthogonal to one another; the amplification, then, depends on how much the *ε-pseudospectrum* protrudes in the $\mathbb{R}^+$ half-plane. These mechanisms may trigger an instability in a modally stable base flow by exciting the nonlinear dynamics which have not been considered in the linearized framework; in some cases they may also lead the system out of the basin of attraction of said modally stable fixed point. This implies that the time-asymptotic fate, as well as the shape of the least stable mode, may be irrelevant to the overall perturbation dynamics, as this limit may never be reached, or it could be reached only under artificial conditions.

For weakly nonparallel flows (see *e.g.* section 3.3) these limitations are so severe that the normal-global mode theory is of little help. For certain flows, then, the eigenvalue spectrum turns out to be a poor proxy for the study of the disturbance behaviour as it only describes the asymptotic fate of the perturbation and fails to capture the short-term characteristics that determine the evolution of such flows.

These observations created the need to redefine stability in a broader sense because eigenvalues do not always govern the transient behaviour of a nonnormal system, nor the asymptotic behaviour in the presence of

nonlinear terms, inhomogeneous forcing data, or other complications [45, 44, 5, 35]. There exist three approaches to the study of nonnormality, *i.e.*, *pseudoresonance*, *destabilizing perturbations* and *transient growth*, only the latter will be here presented.

The transient growth analysis answers the questions of which is the initial condition that produces the largest transient growth of perturbations, after how long such a maximum is reached and how much the initial perturbation has been amplified. To perform this analysis, a measure function has to be chosen in order to compare the effects of different initial conditions. This necessity does not stem only from physical considerations, as the mathematical framework into which the analysis is cast also requires a measure. In this thesis the norm induced by the L^2 inner product has been chosen due to its link with the kinetic energy of the perturbation. The measure function is then defined as:

$$\begin{aligned} G(\boldsymbol{u}_0', t) &= \frac{\mathrm{E_k}(\boldsymbol{u}'(t))}{\mathrm{E_k}(\boldsymbol{u}_0')} = \frac{(\boldsymbol{u}'(t), \boldsymbol{u}'(t))}{(\boldsymbol{u}_0', \boldsymbol{u}_0')} \\ &= \frac{\displaystyle\int_\Omega |\boldsymbol{u}'(t)|^2 \,\mathrm{d}\Omega}{\displaystyle\int_\Omega |\boldsymbol{u}_0'|^2 \,\mathrm{d}\Omega} = \frac{\|\boldsymbol{u}'(t)\|_{L^2}^2}{\|\boldsymbol{u}_0'\|_{L^2}^2}. \end{aligned} \tag{1.12}$$

Formally eliminating the pressure variable p from (1.7), the Linearized Navier–Stokes Equations can be written in compact form as:

$$\frac{\partial \boldsymbol{u}'}{\partial t} = \boldsymbol{\mathcal{L}}_{NS} \boldsymbol{u}', \tag{1.13}$$

where $\boldsymbol{\mathcal{L}}_{NS}$ is a linear operator representing the LNSE. This allows to write the solution to the initial value problem as:

$$\boldsymbol{u}'(t) = e^{t\boldsymbol{\mathcal{L}}_{NS}} \boldsymbol{u}_0'.$$

Substituting this relation in (1.12), the problem becomes:

$$G_{\max}(\tau) = \max_{\boldsymbol{u}_0'} \frac{\|e^{\tau \boldsymbol{\mathcal{L}}_{NS}} \boldsymbol{u}_0'\|_{L^2}^2}{\|\boldsymbol{u}_0'\|_{L^2}^2}, \tag{1.14}$$

where both $G_{\max}(\tau)$ and $\boldsymbol{u}_0'$, such that G is maximized for a given τ, have to be computed.

Obviously, the $\boldsymbol{\mathcal{L}}_{NS}$ operator has to be discretized; the numerical technique adopted in this thesis is presented in section 2.4.

1.8 Critique

As argued by Waleffe [47, 48], *"the question of transition is really a question of existence and basin of attraction of nonlinear self-sustaining solutions that have little contact with the nonnormal linear problem."*

The proposed reason is that nonlinear effects unrelated to the transients play a major role, at least at the moderate Reynolds numbers where transition is observed, and that the linear transient amplification does not significantly select a most amplified disturbance; this implies that a precise predictions about the onset of turbulence cannot be achieved without detailed consideration of the nonlinear effects.

With this in mind, the linear part of the analysis conducted on coaxial jets, presented in Chapter 4, has been backed with Direct Numerical Simulations and guided by the experimental results retrieved from the literature.

CHAPTER 2

Numerical solution

This Chapter is devoted to a description of the strategies employed to discretize the analysis methods employed in this work.

2.1 Galerkin method and Finite Elements discretization

The exposition presented in this section is by no means exhaustive, excellent books on the subject are, for example, [11, 16, 43]. Most importantly, the notation used in the present and in the following chapters is here clearly defined

Both the base flow and the linearized equations (1.6), (1.7) and (1.8), have been discretized using the Finite Element Method. The discretization procedure starts from the weak variational formulation of the respective partial differential problems and leads to a system of algebraic equations.

The incompressible Navier–Stokes equations have been discretized using triangular $\mathbb{P}_2 - \mathbb{P}_1$ (Taylor–Hood) Finite Elements, and a direct solver [1] has been used to solve the algebraic linear systems. The unknowns $\boldsymbol{u}$ and p of the original partial differential problem are approximated by their discrete counterparts

$$\boldsymbol{u}_h(\boldsymbol{r},t) = \sum_{j=1}^{N_h} \boldsymbol{\varphi}_j(\boldsymbol{r}) u_j(t) \qquad \text{and} \qquad p_h(\boldsymbol{r},t) = \sum_{k=1}^{M_h} \phi_k(\boldsymbol{r}) p_k(t), \quad (2.1)$$

where $N_h = \dim\left(\boldsymbol{H}_h^1(\Omega)\right)$ and $M_h = \dim\left(L_h^2(\Omega)\right)$; $\boldsymbol{\varphi}_j(\boldsymbol{r})$ and $\phi_k(\boldsymbol{r})$ represent the base functions defined on these spaces; $\mathsf{u} = [u_j] \in \mathbb{R}^{N_h}$ and $\mathsf{p} = [p_k] \in \mathbb{R}^{M_h}$ are the numerical vector unknowns.

The following bilinear and trilinear forms are also introduced here for clarity:

$$\begin{aligned} a(\boldsymbol{u},\boldsymbol{v}) &= \frac{1}{\mathrm{Re}}\int_\Omega \boldsymbol{\nabla v} : \boldsymbol{\nabla u}, \\ b(\boldsymbol{u},q) &= -\int_\Omega q\boldsymbol{\nabla\cdot u}, \\ c(\boldsymbol{u},\boldsymbol{v},\boldsymbol{w}) &= \int_\Omega \boldsymbol{w}\cdot(\boldsymbol{u}\cdot\boldsymbol{\nabla})\boldsymbol{v}, \\ n_{_{BC}}(\boldsymbol{a},\boldsymbol{v}) &= \int_{\Gamma_N} \boldsymbol{v}\cdot\boldsymbol{a}, \qquad\qquad \forall \boldsymbol{u},\boldsymbol{v},\boldsymbol{w} \in \boldsymbol{H}^1(\Omega) \text{ and } \forall q \in L^2(\Omega); \end{aligned} \tag{2.2}$$

after the discretization of the unknowns, these linear forms will have a discrete counterpart represented by the following matrices and vector:

$$\begin{aligned} \mathsf{A}_{ij} &= a(\boldsymbol{\varphi}_j,\boldsymbol{\varphi}_i) && \in \mathbb{R}^{N_h\times N_h}, \\ \mathsf{B}_{kj} &= b(\boldsymbol{\varphi}_j,\phi_k) && \in \mathbb{R}^{M_h\times N_h}, \\ \mathsf{C}^{\mathsf{u}}_{ij} &= c(\boldsymbol{\varphi}_j,\mathsf{u},\boldsymbol{\varphi}_i) && \in \mathbb{R}^{N_h\times N_h}, \\ \mathsf{C}_{\mathsf{u},ij} &= c(\mathsf{u},\boldsymbol{\varphi}_j,\boldsymbol{\varphi}_i) && \in \mathbb{R}^{N_h\times N_h}, \\ \mathsf{C} &= \mathrm{C}^{\mathsf{u}} + \mathrm{C}_{\mathsf{u}} && \in \mathbb{R}^{N_h\times N_h}, \\ \mathsf{n}_{_{BCi}} &= n_{_{BC}}(\mathsf{a},\boldsymbol{\varphi}_i) && \in \mathbb{R}^{N_h}, \end{aligned} \tag{2.3}$$

the mass matrix will also be used:

$$\mathsf{M}_{ij} = \left(\boldsymbol{\varphi}_j,\boldsymbol{\varphi}_i\right) \qquad \in \mathbb{R}^{N_h\times N_h}. \tag{2.4}$$

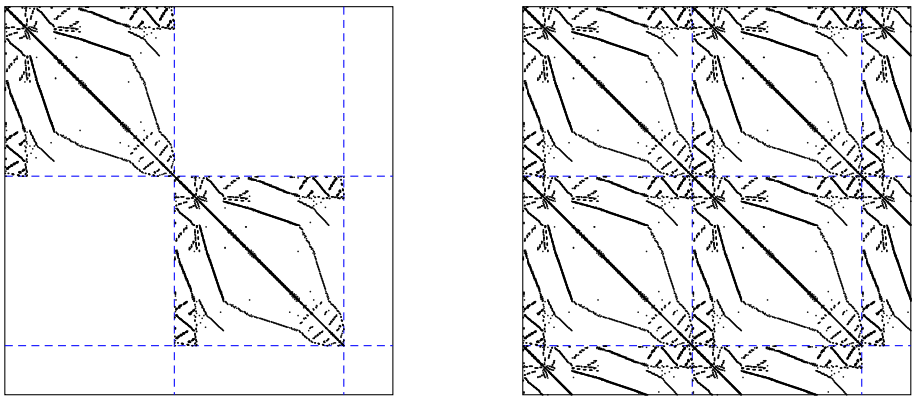

(a) *Mass operator.*

(b) *Linearized Navier–Stokes operator.*

Figure 2.1 *Sparsity patterns for mass and $\mathcal{L}_{NS}$ operators on a grid consisting of 128 elements in the 2D Cartesian case. The 3D axisymmetric case presents the same sparsity patterns, it simply has one more velocity component.*

Attention must be paid to the difference between 2D Cartesian and 3D cylindrical coordinates. In particular, the laplacian term, integrated by parts, assumes two quite different formulations due to the difference in the expression of the gradient of a vector field in the two reference systems:

$$\boldsymbol{\nabla u} \underset{\text{2D Cart.}}{=} \begin{pmatrix} \dfrac{\partial u_x}{\partial x} & \dfrac{\partial u_x}{\partial y} \\ \dfrac{\partial u_y}{\partial x} & \dfrac{\partial u_y}{\partial y} \end{pmatrix}, \tag{2.5}$$

$$\begin{aligned} \breve{\boldsymbol{\nabla}} \boldsymbol{u} \underset{\text{3D cyl.}}{=} & \frac{\partial u_r}{\partial r} \boldsymbol{e}_r \otimes \boldsymbol{e}_r + \frac{1}{r}\left(\frac{\partial u_r}{\partial \theta} - u_\theta\right) \boldsymbol{e}_r \otimes \boldsymbol{e}_\theta + \frac{\partial u_r}{\partial z} \boldsymbol{e}_r \boldsymbol{e}_z \\ & + \frac{\partial u_\theta}{\partial r} \boldsymbol{e}_\theta \otimes \boldsymbol{e}_r + \frac{1}{r}\left(\frac{\partial u_\theta}{\partial \theta} + u_r\right) \boldsymbol{e}_\theta \otimes \boldsymbol{e}_\theta + \frac{\partial u_\theta}{\partial z} \boldsymbol{e}_\theta \boldsymbol{e}_z \\ & + \frac{\partial u_z}{\partial r} \boldsymbol{e}_z \otimes \boldsymbol{e}_r + \frac{1}{r} \frac{\partial u_r}{\partial \theta} \boldsymbol{e}_z \otimes \boldsymbol{e}_\theta + \frac{\partial u_z}{\partial z} \boldsymbol{e}_z \boldsymbol{e}_z. \end{aligned} \tag{2.6}$$

This difference does not influence the stiffness term very much:

$$\begin{aligned} \boldsymbol{\nabla v} : \boldsymbol{\nabla u} \underset{\text{2D Cart.}}{=} & \frac{\partial v_x}{\partial x} \frac{\partial u_x}{\partial x} + \frac{\partial v_x}{\partial y} \frac{\partial u_x}{\partial y} \\ & + \frac{\partial v_y}{\partial x} \frac{\partial u_y}{\partial x} + \frac{\partial v_y}{\partial y} \frac{\partial u_y}{\partial y}, \end{aligned} \tag{2.7}$$

$$\begin{aligned}\breve{\boldsymbol{\nabla}}\boldsymbol{v} : \breve{\boldsymbol{\nabla}}\boldsymbol{u} \underset{\text{3D cyl.}}{=} & \frac{\partial v_r}{\partial r}\frac{\partial u_r}{\partial r} + \frac{1}{r^2}\left(\frac{\partial v_r}{\partial \theta} - v_\theta\right)\left(\frac{\partial u_r}{\partial \theta} - u_\theta\right) + \frac{\partial v_r}{\partial z}\frac{\partial u_r}{\partial z} \\ & + \frac{\partial v_\theta}{\partial r}\frac{\partial u_\theta}{\partial r} + \frac{1}{r^2}\left(\frac{\partial v_\theta}{\partial \theta} + v_r\right)\left(\frac{\partial u_\theta}{\partial \theta} + u_r\right) + \frac{\partial v_\theta}{\partial z}\frac{\partial u_\theta}{\partial z} \\ & + \frac{\partial v_z}{\partial r}\frac{\partial u_z}{\partial r} + \frac{1}{r^2}\frac{\partial v_z}{\partial \theta}\frac{\partial u_z}{\partial \theta} + \frac{\partial v_z}{\partial z}\frac{\partial u_z}{\partial z},\end{aligned} \tag{2.8}$$

but makes the quasi stress-free boundary term $\frac{1}{\mathrm{Re}}\frac{\partial \boldsymbol{u}}{\partial \hat{\boldsymbol{n}}} - p\hat{\boldsymbol{n}}$ (as $\frac{\partial \boldsymbol{u}}{\partial \hat{\boldsymbol{n}}} = \hat{\boldsymbol{n}} \cdot \boldsymbol{\nabla}\boldsymbol{u}$) quite intricated as, in cylindrical coordinates, it depends on the position and orientation of the boundary.

2.1.1 Base flow

Starting from the strong form presented in section 1.4.1 and after standard mathematical manipulation, not reported here for conciseness, the weak formulation for the base flow reads:

find $\boldsymbol{U} \in \boldsymbol{H}^1(\Omega)$ *and* $P \in L^2(\Omega)$ *such that:*

$$\begin{cases} \displaystyle\int_\Omega \boldsymbol{v} \cdot (\boldsymbol{U} \cdot \boldsymbol{\nabla})\boldsymbol{U} + \frac{1}{\mathrm{Re}}\int_\Omega \boldsymbol{\nabla}\boldsymbol{v} : \boldsymbol{\nabla}\boldsymbol{U} - \int_\Omega P\boldsymbol{\nabla}\cdot\boldsymbol{v} = \int_{\Gamma_N} \boldsymbol{v}\cdot\boldsymbol{a} \\ \displaystyle\int_\Omega q\boldsymbol{\nabla}\cdot\boldsymbol{U} = 0, \\ \boldsymbol{U} = \boldsymbol{b}, \qquad\qquad \forall \boldsymbol{r} \in \Gamma_D; \\ \displaystyle\frac{1}{\mathrm{Re}}\frac{\partial \boldsymbol{U}}{\partial \hat{\boldsymbol{n}}} - P\hat{\boldsymbol{n}} = \boldsymbol{a}, \qquad \forall \boldsymbol{r} \in \Gamma_N; \end{cases} \tag{2.9}$$

$\forall \boldsymbol{v} \in \boldsymbol{H}^1_{\Gamma_D}(\Omega)$ *and* $\forall q \in L^2(\Omega)$; $\boldsymbol{b} \in \boldsymbol{H}^{1/2}_{\Gamma_D}(\Omega)$, $\boldsymbol{a} \in \boldsymbol{L}^2(\Gamma_N)$.

These equations are nonlinear due to the presence of the convective term. In order to compute the solution, Newton's method has been employed, as explained in the following pages. Newton's method has been preferred to a time marching procedure because of its efficiency: just a few iterations are needed to reach convergence, provided the initial guess is chosen not too far from the solution, while a time stepping technique may reach the steady state only if it is asymptotically stable and the number of time steps increases as a bifurcation point is approached.

Algebraic formulation After substituting the series expansions of the unknowns (2.1), in the weak form of the problem (2.9), the discrete formulation for the base flow reads:

$$\begin{bmatrix} \mathsf{A} + \mathsf{C_u} & \mathsf{B}^\mathsf{T} \\ \mathsf{B} & 0 \end{bmatrix} \begin{bmatrix} \mathsf{u} \\ \mathsf{p} \end{bmatrix} = \begin{bmatrix} \mathsf{n}_{BC} \\ \mathsf{0} \end{bmatrix}, \tag{2.10}$$

which is a nonlinear system of equations in the unknowns u_j and p_j as the matrix in the left hand side depends on the solution. This nonlinear system has been solved by a Newton iterative method, as reported in the following section.

The three formulations of Newton's method This paragraph presents the application of Newton's method to the base flow equations written in strong form for clarity. The same algorithm can be straightforwardly applied also to the equations in weak form or to their discretization. An in-depth analysis of this method applied to a FE discretization can be found, for instance, in [16].

To start, it is useful to introduce a shorthand for the strong form of the base flow equations (1.6):

$$\mathcal{N}(\boldsymbol{x}) = 0,$$

where $\boldsymbol{x} = (\boldsymbol{u}, p)$, and $\mathcal{N}(\boldsymbol{x})$ is a nonlinear operator representing the steady Navier–Stokes equations (see eq. (1.1)) which can be expressed as

$$\mathcal{N}(\boldsymbol{x}) = \mathcal{Q}(\boldsymbol{x}, \boldsymbol{x}) + \mathcal{L}(\boldsymbol{x}) = 0,$$

where the bilinear quadratic form $\mathcal{Q}(\boldsymbol{x}, \boldsymbol{x})$ has been separated from the linear form $\mathcal{L}(\boldsymbol{x})$:

$$\mathcal{Q}(\boldsymbol{x}, \boldsymbol{y}) = \begin{pmatrix} (\boldsymbol{u} \cdot \nabla)\boldsymbol{v} & 0 \\ 0 & 0 \end{pmatrix}, \qquad \mathcal{L}(\boldsymbol{x}) = \begin{pmatrix} -\dfrac{1}{\mathrm{Re}}\nabla^2 \boldsymbol{u} & \boldsymbol{\nabla} p \\ \boldsymbol{\nabla} \cdot \boldsymbol{u} & 0 \end{pmatrix},$$

where $\boldsymbol{y} = (\boldsymbol{v}, q)$.

To obtain Newton's algorithm, $\mathcal{N}(\boldsymbol{x})$ needs to be expanded in Taylor series, truncated at first order, in the neighbourhood of an approximate solution $\boldsymbol{x}_n$:

$$\mathcal{N}(\boldsymbol{x}) \approx \mathcal{N}(\boldsymbol{x}_n) + \mathcal{J}|_{\boldsymbol{x}_n}(\boldsymbol{x} - \boldsymbol{x}_n) = 0,$$

where $\mathcal{J}|_{\boldsymbol{y}}$ represents the Jacobian matrix of the system computed in $\boldsymbol{y}$:

$$\begin{aligned}\mathcal{J}|_{\boldsymbol{y}} &= \nabla_{\boldsymbol{x}}\mathcal{N}(\boldsymbol{y}) \\ &= \mathcal{Q}(\boldsymbol{y}, \dots) + \mathcal{Q}(\dots, \boldsymbol{y}) + \mathcal{L} \\ &= \begin{pmatrix} (\boldsymbol{v}\cdot\nabla)\ \dots + (\dots\ \cdot\nabla)\boldsymbol{v} - \dfrac{1}{\mathrm{Re}}\nabla^2\ \dots & \boldsymbol{\nabla}\dots \\ \boldsymbol{\nabla}\cdot\ \dots & 0 \end{pmatrix}.\end{aligned}$$

After defining the increments as:

$$\delta\boldsymbol{x}_{n+1} = \boldsymbol{x}_{n+1} - \boldsymbol{x}_n \quad \text{and} \quad \delta\boldsymbol{x}_n = \boldsymbol{x}_n - \boldsymbol{x}_{n-1},$$

three versions of Newton's algorithm can be defined:

- *non-incremental formulation*: $\mathcal{J}|_{\boldsymbol{x}_n}(\boldsymbol{x}_{n+1}) = \mathcal{Q}(\boldsymbol{x}_n, \boldsymbol{x}_n)$,
- *incremental formulation*: $\mathcal{J}|_{\boldsymbol{x}_n}(\delta\boldsymbol{x}_{n+1}) = -\mathcal{N}(\boldsymbol{x}_n)$,
- *bi-incremental formulation*: $\mathcal{J}|_{\boldsymbol{x}_n}(\delta\boldsymbol{x}_{n+1}) = -\mathcal{Q}(\delta\boldsymbol{x}_n, \delta\boldsymbol{x}_n)$.

All of the above formulations have been implemented in the software but the *bi-incremental*, being the most elegant and efficient, is the one actually used in the iterations, while the other ones are used to start the algorithm when an increment is missing. Newton's algorithm is stopped when the residual, computed as $\|\mathcal{N}(\boldsymbol{x}_n)\|_{L^\infty} = \|\mathcal{Q}(\delta\boldsymbol{x}_n, \delta\boldsymbol{x}_n)\|_{L^\infty}$, is found to be lower than a chosen tolerance, usually set to 10^{-15}.

Newton's algorithm is started either from the solution of the Stokes problem or from a previously computed solution for a different value of the parameters characterizing the flow. In either cases, care must be paid to the correct treatment of non-homogeneous boundary conditions on the velocity field: if the *incremental* or *bi-incremental* formulations are being used the boundary conditions have to be applied to the increment $\delta\boldsymbol{x}_n$ or $\delta\boldsymbol{x}_{n+1}$. This means that in the simple case of the computation of a steady state solution, non-homogeneous boundary conditions will be applied to the solution of the Stokes problem, *i.e.*, $\boldsymbol{x}_0$, and the increments will only need homogeneous boundary conditions. On the other hand, in the more complicated case of the continuation of a previously computed solution, if the boundary conditions are changed between the two base flows, incremental boundary conditions need to be applied to the first step of Newton's algorithm, only then the program can proceed with homogeneous boundary conditions. An example of the second case is the tracking of the bifurcations presented by the flow around a circular rotating cylinder, see section 3.1.

2.1.2 Linearized equations

Starting from the strong form presented in section 1.4.2 and after simple algebraic manipulations, not reported here for conciseness, the weak formulation of the direct LNSE reads:

$$
\begin{aligned}
&\textit{find } \boldsymbol{u}' \in L^2\left(\mathbb{R}^+; \boldsymbol{H}^1(\Omega)\right) \textit{ and } p' \in L^2(\Omega) \textit{ such that:}\\
&\begin{cases}
\displaystyle\int_\Omega \boldsymbol{v}\cdot\frac{\partial \boldsymbol{u}'}{\partial t} + \int_\Omega \boldsymbol{v}\cdot(\boldsymbol{U}\cdot\boldsymbol{\nabla})\boldsymbol{u}' + \int_\Omega \boldsymbol{v}\cdot(\boldsymbol{u}'\cdot\boldsymbol{\nabla})\boldsymbol{U} \\
\qquad\qquad + \dfrac{1}{\mathrm{Re}}\displaystyle\int_\Omega \boldsymbol{\nabla v} : \boldsymbol{\nabla u}' - \int_\Omega p'\boldsymbol{\nabla}\cdot\boldsymbol{v} = \int_{\Gamma_N} \boldsymbol{v}\cdot\boldsymbol{a} \\
\displaystyle\int_\Omega q\boldsymbol{\nabla}\cdot\boldsymbol{u}' = 0, \\
\boldsymbol{u}' = \boldsymbol{b}, \qquad\qquad \forall \boldsymbol{r} \in \Gamma_D; \\
\dfrac{1}{\mathrm{Re}}\dfrac{\partial \boldsymbol{u}'}{\partial \hat{\boldsymbol{n}}} - p'\hat{\boldsymbol{n}} = \boldsymbol{a}, \qquad\qquad \forall \boldsymbol{r} \in \Gamma_N;
\end{cases}\\
&\forall \boldsymbol{v} \in \boldsymbol{H}^1_{\Gamma_D}(\Omega) \textit{ and } \forall q \in L^2(\Omega);\ \boldsymbol{b} \in \boldsymbol{H}^{1/2}_{\Gamma_D}(\Omega),\ \boldsymbol{a} \in \boldsymbol{L}^2(\Gamma_N).
\end{aligned}
\tag{2.11}
$$

The weak formulation of the adjoint LNSE (1.8) is obtained following the same steps but it is not presented here because a discrete adjoint approach has been used instead of discretizing the continuous adjoint equations, as explained in the following.

Algebraic formulation As seen for the base flow equations, after substituting the series expansions of the unknowns (2.1) in the weak form of the problem (2.11), the discrete formulation for the direct LNSE reads:

$$
\begin{bmatrix} \mathsf{M} & 0 \\ 0 & 0 \end{bmatrix}
\begin{bmatrix} \dot{\mathsf{u}}' \\ \dot{\mathsf{p}}' \end{bmatrix}
+
\begin{bmatrix} \mathsf{A}+\mathsf{C} & \mathsf{B}^\intercal \\ \mathsf{B} & 0 \end{bmatrix}
\begin{bmatrix} \mathsf{u}' \\ \mathsf{p}' \end{bmatrix}
=
\begin{bmatrix} \mathsf{n}_{BC} \\ \mathsf{0} \end{bmatrix}.
\tag{2.12}
$$

Employing the definition of the discrete adjoint of a linear operator, *i.e.*, the complex conjugate of the discretized operator, the discrete formulation for the adjoint LNSE is easily obtained:

$$
\begin{bmatrix} \mathsf{M} & 0 \\ 0 & 0 \end{bmatrix}
\begin{bmatrix} \dot{\mathsf{v}}' \\ \dot{\mathsf{q}}' \end{bmatrix}
+
\begin{bmatrix} \mathsf{A}+\mathsf{C}^\intercal & \mathsf{B}^\intercal \\ \mathsf{B} & 0 \end{bmatrix}
\begin{bmatrix} \mathsf{v}' \\ \mathsf{q}' \end{bmatrix}
=
\begin{bmatrix} \mathsf{n}_{BC} \\ \mathsf{0} \end{bmatrix}.
\tag{2.13}
$$

The discrete adjoint has been preferred over its continuous counterpart because it warrants the orthogonality of its eigenvectors with respect to the ones

of the direct operator, see sections 2.3 and 2.4, while the eigenvectors of the discretized adjoint equations satisfy the orthogonality condition only approximatively, with an error dependent on the truncation error.

To integrate in time these equations, the Implicit Euler and Crank–Nicolson methods have been employed, as reported in the following formulas in the case of the direct LNSE.

Implicit Euler

$$\begin{bmatrix} \frac{1}{\Delta t}\mathsf{M} + \mathsf{A} + \mathsf{C} & \mathsf{B}^\intercal \\ \mathsf{B} & 0 \end{bmatrix} \begin{bmatrix} \mathsf{u'}^{n+1} \\ \mathsf{p'}^{n+1} \end{bmatrix} = \begin{bmatrix} \frac{1}{\Delta t}\mathsf{M} & 0 \\ 0 & 0 \end{bmatrix} \begin{bmatrix} \mathsf{u'}^{n} \\ \mathsf{p'}^{n} \end{bmatrix} + \begin{bmatrix} \mathsf{n}_{BC} \\ \mathsf{0} \end{bmatrix}, \tag{2.14}$$

Crank–Nicolson

$$\begin{bmatrix} \frac{1}{\Delta t}\mathsf{M} + \frac{1}{2}(\mathsf{A} + \mathsf{C}) & \frac{1}{2}\mathsf{B}^\intercal \\ \mathsf{B} & 0 \end{bmatrix} \begin{bmatrix} \mathsf{u'}^{n+1} \\ \mathsf{p'}^{n+1} \end{bmatrix} = \begin{bmatrix} \frac{1}{\Delta t}\mathsf{M} - \frac{1}{2}(\mathsf{A} + \mathsf{C}) & -\frac{1}{2}\mathsf{B}^\intercal \\ 0 & 0 \end{bmatrix} \begin{bmatrix} \mathsf{u'}^{n} \\ \mathsf{p'}^{n} \end{bmatrix} + \begin{bmatrix} \mathsf{n}_{BC} \\ \mathsf{0} \end{bmatrix}. \tag{2.15}$$

It is useful to recall, in passing, that the Implicit Euler scheme is first order accurate, while the Crank–Nicolson scheme is second order accurate.

2.2 Continuation of solutions and bifurcation points

One useful feature implemented in the software developed during this work is the possibility to perform the continuation of solutions and bifurcation points.

The continuation of steady state solutions allows to use, as initial guess for Newton's algorithm, a base flow computed for different values of the parameters characterizing the flow. This point assures two fundamental advantages: it reduces the number of iterations needed to reach convergence with respect to those that are needed starting from the solution of the Stokes problem, and allows to compute base flows for high Reynolds numbers, which are impossible to converge upon if starting from the solution of the Stokes problem.

The continuation of steady state solutions and bifurcation points has been introduced in the code by interfacing it to the C library of continuation algorithms LOCA [33]. LOCA allows tracking solution branches and bifurcation points as a function of system parameters.

The adopted approach consists in adding the equations describing the bifurcation to those that define the steady state. Newton's method is then applied to the augmented system; however, instead of loading the Jacobian matrix for the entire augmented system, bordering algorithms are used to split the solution of the complete linear system into the solution of a number of smaller linear systems.

The aim of tracking bifurcation points is to identify the different regions of the parameter space where the system displays qualitatively different behaviours. Although, in principle, it would be possible to map these regions using only transient calculations, in practice it results unreliable: if, for example, multiple steady state solutions coexist, it is not possible to mathematically determine how many trials are needed in order to calculate the number of fixed points. Moreover, solving steady state equations is much more computationally efficient than integrating until a steady state is reached.

2.3 Eigenvalues and eigenvectors computation

The eigenvalues and eigenvectors, for both the direct and adjoint problems, have been computed by means of an interface to the ARPACK library [23]. ARPACK, which stands for ARnoldi PACKage, is based on the Implicitly Restarted Arnoldi procedure which is a technique for approximating a few eigenvalues and eigenvectors of a general $n \times n$ matrix.

After discretization by the Finite Element Method (described in section 2.1), the generalized eigenvalue problem (1.9) is replaced by the following set of algebraic equations:

$$\lambda \begin{bmatrix} \mathsf{M} & 0 \\ 0 & 0 \end{bmatrix} \begin{bmatrix} \hat{\mathsf{u}} \\ \hat{\mathsf{p}} \end{bmatrix} = - \begin{bmatrix} \mathsf{A} + \mathsf{C} & \mathsf{B}^{\mathsf{T}} \\ \mathsf{B} & 0 \end{bmatrix} \begin{bmatrix} \hat{\mathsf{u}} \\ \hat{\mathsf{p}} \end{bmatrix}, \tag{2.16}$$

which can be conveniently rewritten as follows:

$$\lambda \mathsf{D}\hat{\mathsf{x}} = \mathsf{E}\hat{\mathsf{x}}. \tag{2.17}$$

The shift and invert spectral transformation is used to accelerate convergence to the desired portion of the spectrum, and allows the computation of eigenvalues which would otherwise be out of reach. If $(\hat{\mathsf{x}}, \lambda)$ is an eigen-pair for (D, E) and $\sigma \neq \lambda$, then

$$(\mathsf{E} - \sigma\mathsf{D})^{-1}\mathsf{D}\hat{\mathsf{x}} = \hat{\mathsf{x}}\nu \qquad \text{where} \qquad \nu = \frac{1}{\lambda - \sigma}. \tag{2.18}$$

For a given number of Lanczos basis vectors, `ncv`, the computational work required is proportional to $\mathtt{n} \cdot \mathtt{ncv}^2$ FLOPs (where `n` is the dimension of E and D). The results presented in this work have been computed setting `ncv` = 2 `nev` + 2 (where `nev` is the number of requested eigenvalues); the value of `nev` and `ncv` leading to optimal performance depends very much on the problem and is not completely understood, as the authors of ARPACK write.

2.4 Computing transient growth

As seen in section 1.7, the optimal condition $\boldsymbol{u}'_0$ with maximum transient growth obeys the following relation:

$$G_{\max}(\tau) = \max_{\boldsymbol{u}'_0} \frac{\|e^{\tau \mathcal{L}_{NS}} \boldsymbol{u}'_0\|^2_{L^2}}{\|\boldsymbol{u}'_0\|^2_{L^2}}, \tag{2.19}$$

where $\mathcal{L}_{NS}$ is the linear operator representing the Linearized Navier–Stokes equations, (1.7) or (1.13).

After discretization by the Galerkin and Finite Element methods (see section 2.1), the operators in (1.13) are substituted by matrices and the unknowns by vector arrays, namely,

$$\frac{\partial \boldsymbol{u}'}{\partial t} = \mathcal{L}_{NS} \boldsymbol{u}' \quad \rightarrow \quad \mathsf{M}\dot{\mathsf{u}}' = \mathsf{L}\mathsf{u}', \tag{2.20}$$

therefore, the solution of the discretized system is:

$$\mathsf{u}'(\tau) = e^{\tau \mathsf{M}^{-1}\mathsf{L}} \mathsf{u}'_0 = \mathsf{L}_\tau \mathsf{u}'_0, \tag{2.21}$$

where the matrix L_τ has been introduced here just for compactness and ease of notation but is never assembled: it will, instead, be approximated by integrating the linearized equations in time as explained later in this section.

Four basic notions are necessary to proceed:

- the Cholesky decomposition of the mass matrix, which is symmetric positive-definite,

$$\mathsf{M} = \mathsf{C}^\intercal \mathsf{C}, \tag{2.22}$$

- the relation between L^2 and Euclidean norms

$$\|\mathsf{x}\|_{L^2} = \sqrt{\mathsf{x}^\intercal \mathsf{M} \mathsf{x}} = \sqrt{\mathsf{x}^\intercal \mathsf{C}^\intercal \mathsf{C} \mathsf{x}} = \|\mathsf{C}\mathsf{x}\|_2, \tag{2.23}$$

- the definition of the norm induced on an $m \times n$ matrix by the norm of a vector

$$\|\mathsf{A}\| = \max\left\{\frac{\|\mathsf{A}\mathsf{x}\|}{\|\mathsf{x}\|} : \mathsf{x} \in \mathbb{R}^n \text{ with } \mathsf{x} \neq 0\right\}, \tag{2.24}$$

  which, in the case of the Euclidean norm and $m = n$, is the *spectral norm*, *i.e.*, the largest singular value of A,

- the definition of the discretized adjoint operator with respect to the L^2 inner product

$$\begin{aligned}&(\boldsymbol{v}, \mathcal{A}\boldsymbol{u}) = \left(\mathcal{A}^\dagger \boldsymbol{v}, \boldsymbol{u}\right),\\ &\mathsf{A}^\dagger = \mathsf{M}^{-1}\mathsf{A}^\intercal\mathsf{M}.\end{aligned} \tag{2.25}$$

Now, starting from the definition of the energy function (2.19), and using (2.21) and (2.23),

$$G_{\max}(\tau) = \max_{\mathsf{u}_0'} \frac{\|\mathsf{L}_\tau \mathsf{u}_0'\|_{L^2}^2}{\|\mathsf{u}_0'\|_{L^2}^2} = \max_{\mathsf{C}\mathsf{u}_0'} \frac{\|\mathsf{C}\mathsf{L}_\tau \mathsf{u}_0'\|_2^2}{\|\mathsf{C}\mathsf{u}_0'\|_2^2}, \tag{2.26}$$

and, by the definition of the identity matrix, modifying the numerator,

$$G_{\max}(\tau) = \max_{\mathsf{C}\mathsf{u}_0'} \frac{\|\mathsf{C}\mathsf{L}_\tau\mathsf{C}^{-1}\mathsf{C}\mathsf{u}_0'\|_2^2}{\|\mathsf{C}\mathsf{u}_0'\|_2^2}, \tag{2.27}$$

it is now possible to recognize definition (2.24) for the vector $\mathsf{C}\mathsf{u}_0'$ which allows to write (also employing the definition of singular value and, again, the Cholesky decomposition for the mass matrix),

$$G_{\max}(\tau) = \|\mathsf{C}\mathsf{L}_\tau\mathsf{C}^{-1}\|_2^2 = \sigma_{\max}^2\left(\mathsf{C}\mathsf{L}_\tau\mathsf{C}^{-1}\right) = \lambda_{\max}\left(\mathsf{C}^{-\intercal}\mathsf{L}_\tau^\intercal\mathsf{M}\mathsf{L}_\tau\mathsf{C}^{-1}\right). \tag{2.28}$$

This leads to a standard eigenvalue problem for the vector $\mathsf{C}\mathsf{u}_0'$

$$\mathsf{C}^{-\intercal}\mathsf{L}_\tau^\intercal\mathsf{M}\mathsf{L}_\tau\mathsf{C}^{-1}\mathsf{C}\mathsf{u}_0' = \lambda\mathsf{C}\mathsf{u}_0' \tag{2.29}$$

that, after multiplying the previous equation on the left by C^{-1}, is equivalent to a standard eigenvalue problem for the vector u_0' in the form

$$\mathsf{M}^{-1}\mathsf{L}_\tau^\intercal\mathsf{M}\mathsf{L}_\tau\mathsf{u}_0' = \lambda\mathsf{u}_0', \tag{2.30}$$

which, recalling the definition of the discretized adjoint operator (2.25), can be rewritten as

$$\mathsf{L}_\tau^\dagger\mathsf{L}_\tau\mathsf{u}_0' = \lambda\mathsf{u}_0'. \tag{2.31}$$

This is the eigenvalue problem to be solved to compute both the maximum of the energy function $G_{\max}(\tau)$ and the initial condition u_0' that produces it.

The matrix exponential and the adjoint operator As already mentioned, the matrix exponential is not actually assembled, instead it is approximated by advancing the linearized equations in time using the Crank–Nicolson method (2.15). In fact, whichever algorithm is chosen for the solution of the eigenvalue problem, only the *action* of the adjoint and direct operators on a given vector has to be computed. This procedure requires to advance in time the system whose transition matrix is

$$\mathsf{L}_\tau^\dagger = \mathsf{M}^{-1}\mathsf{L}_\tau^\intercal\mathsf{M} = \mathsf{M}^{-1}e^{\tau\mathsf{L}^\intercal\mathsf{M}^{-1}}\mathsf{M}, \tag{2.32}$$

with the associated difficulty of creating a time stepper capable of using the matrices in inverse order. In the particular case under investigation, though, it can be demonstrated that

$$e^{\tau\mathsf{L}^\intercal\mathsf{M}^{-1}} = \mathsf{M}e^{\tau\mathsf{M}^{-1}\mathsf{L}^\intercal}\mathsf{M}^{-1},$$

which reduces (2.32) to

$$\mathsf{L}_\tau^\dagger = \mathsf{M}^{-1}e^{\mathsf{L}^\intercal\mathsf{M}^{-1}\tau}\mathsf{M} = e^{\tau\mathsf{M}^{-1}\mathsf{L}^\intercal}. \tag{2.33}$$

This not only simplifies the eigenvalue problem, eliminating the mass product and linear solve, but also allows to use the same time stepper for both the direct and the adjoint operators, by simply transposing one matrix.

As the eigenvalue problem (2.31) involves only the velocity vector and gets rid of the pressure field, whilst the time steppers presented in section 2.1.2 act on both velocity and pressure fields, the first step of the time integration employed to discretize the matrix exponential of eq. (2.21) has been performed using the Implicit Euler scheme and a reduced Δt, thus eliminating the need for an initial pressure field but maintaining the second order accuracy of the Crank–Nicolson scheme.

2.4.1 Initial guess

A random velocity field has been chosen as initial guess to assure the unbiasedness of the solution. Such a field, though, ought satisfy boundary conditions and the incompressibility constraint.

To generate the random guess, a routine has been written which initializes the Fortran 95 random seed generator using, as input parameters, the current date and time of the machine on which the program is being run and a few prime numbers. A random velocity value, with a normal distribution, is then assigned on each $\mathbb{P}_2$ node.

After this procedure, boundary conditions and null divergence are imposed on the field in the following way: let $\boldsymbol{u}_r$ be the random field generated, to

find a solenoidal velocity field $\boldsymbol{u}$ which is as close as possible to $\boldsymbol{u}_r$ in the L^2 norm but satisfies the incompressibility constraint and boundary conditions, the difference $\|\boldsymbol{u}-\boldsymbol{u}_r\|_{L^2}$ has to be minimized. The procedure consists in defining a functional J, which also enforces the solenoidality of $\boldsymbol{u}$ by means of a Lagrange multiplier λ, and minimizing it:

$$J = \frac{1}{2}\|\boldsymbol{u}-\boldsymbol{u}_r\|_{L^2} - \int_\Omega \lambda \boldsymbol{\nabla}\cdot\boldsymbol{u}.$$

The minimization is achieved by imposing a null variation of the functional where the variations $\delta\boldsymbol{u}$ and $\delta\lambda$ can be replaced with the corresponding test functions $\boldsymbol{v}$ and q to obtain the weak form of the projection step:

$$\begin{aligned}
&\textit{find } \boldsymbol{u}\in\boldsymbol{H}^1(\Omega) \textit{ and } \lambda\in L^2(\Omega) \textit{ such that:}\\
&\begin{cases}
\displaystyle\int_\Omega \boldsymbol{v}\cdot\boldsymbol{u} - \int_\Omega \lambda\boldsymbol{\nabla}\cdot\boldsymbol{v} = \int_\Omega \boldsymbol{v}\cdot\boldsymbol{u}_r\\
\displaystyle\int_\Omega q\boldsymbol{\nabla}\cdot\boldsymbol{u} = 0\\
\boldsymbol{u}=\boldsymbol{b}, \qquad \forall \boldsymbol{r}\in\Gamma_D;
\end{cases}\\
&\forall \boldsymbol{v}\in\boldsymbol{H}^1_{\Gamma_D}(\Omega) \textit{ and } \forall q\in L^2(\Omega).
\end{aligned} \tag{2.34}$$

2.4.2 Remarks

It is important to keep in mind that the curve given by $G_{\max}(\tau)$ represents the maximum possible energy amplification, which for each instant in time is optimized over all possible initial conditions. Therefore, the initial condition that optimizes the amplification factor might be different for different values of τ; this is why the curve $G_{\max}(\tau)$ should be thought of as the envelope of the energy evolution of individual initial conditions. It should also be noted that a given initial condition may reach higher energies after τ, but at time τ it will be the initial disturbance among all disturbances that reaches the maximum possible energy amplification [36].

CHAPTER 3

Validation cases

This chapter provides a complete validation of all of the parts of the code developed in this work. Several geometries, both 2D and 3D axisymmetric, and different reference flows have been used for the purpose.

The vortex shedding in the cylinder wake represents an example of oscillator-type flow, where intrinsic flow oscillations, observed in the nonlinear regime, are found to be linked to the presence of at least one unstable normal-global mode, which sets in through a Hopf bifurcation. In open shear flows, global instability is typically associated with the presence of a locally absolutely unstable flow region [5, 18], although feedback mechanisms may also be responsible for the flow destabilization.

By contrast, round viscous jets, unless sufficiently hot [25, 24], are prominent examples of amplifier-type flows, characterized by a stable global eigenspectrum. Consistent with the notion of local convective instability, nonnormal interaction of stable global modes may give rise to transient perturbation growth [5].

3.1 Flow around a circular rotating cylinder

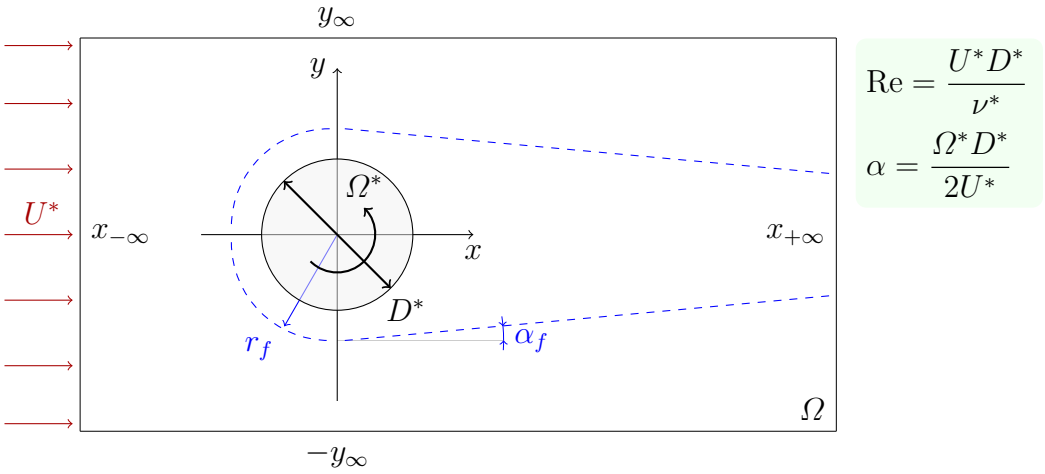

Figure 3.1 *Geometry and mesh structure of the flow around a circular rotating cylinder. $x_{-\infty}$, $x_{+\infty}$ and y_∞ are, respectively, the location of the inlet, outlet and lateral boundaries. The dashed (blue) lines enclose the area where the mesh has been refined; mesh data is reported in table 3.1.*

This test case has been chosen because it is very well documented in the literature and allows the validation of nearly all of the parts of the code. It has been used to validate the 2D base flow solver, the direct and adjoint eigenfunction computation, the bifurcation tracking algorithms and the computation of transient growth.

The boundary conditions used are: a uniform velocity profile, $U^* \boldsymbol{e}_x$, on the inflow and quasi stress-free both at the outflow and on lateral borders. Whilst in a DNS it would be impossible to impose Neumann type boundary conditions on lateral borders, not only a steady simulation allows their use, but also they render the flow a bit more representative of that around an isolated, *i.e.*, not confined, cylinder. Homogeneous Dirichlet boundary conditions for the velocity have been used on the surface of the cylinder, imposing the angular rotation Ω^*.

Base flow The capabilities of the 2D FEM solver have been tested by measuring the length and separation angle of the recirculating bubble behind the cylinder for $\alpha = 0$. Good agreement has been found with both theoretical-numerical and experimental results even when using a coarse mesh. The measurements on the computed base flows have been compared with those presented in [6] and are depicted in figure 3.2. This test has been performed

against experimental measures, not numerical computations, to verify how well the FEM solver compared with experiments.

Mesh	$x_{-\infty}$	$x_{+\infty}$	y_{∞}	r_f	α_f	h_c	n_{e}	$n_{\text{d.o.f.}}$
M_1	-20	50	20	0.7	10°	0.05	62 369	281 213
M_2	-60	200	30	1.5	1°	0.02	459 322	2 069 594
M_3	-20	50	20	1.5	5°	0.02	465 847	2 097 524
M_4	-45	125	45	0.2	1°	0.1	108 282	488 649

Table 3.1 *Characteristics of the meshes used for the flow around a circular rotating cylinder. $x_{-\infty}$, $x_{+\infty}$ and y_{∞} are, respectively, the location of the inlet, outlet and lateral boundaries. r_f and α_f are the parameters used to define the area of finer mesh (see figure 3.1). h_c is the length of the sides of the elements inside the refined area. n_e and $n_{d.o.f.}$ are the number of elements and the number of degrees of freedom of an unknown $\boldsymbol{x} = (u_x, u_y, p)$, respectively.*

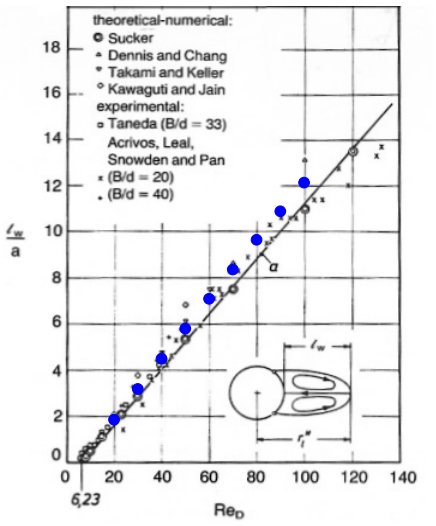

(a) *Length of the recirculating bubble.*

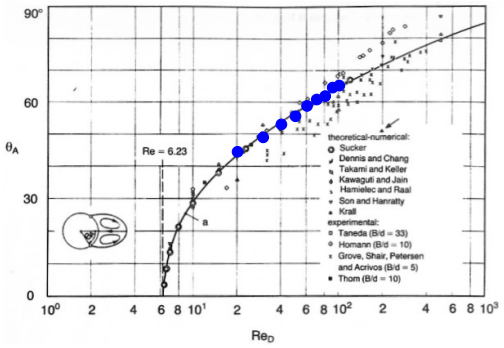

(b) *Separation angle.*

Figure 3.2 *Validation of the 2D steady FEM solver against the theoretical-numerical and experimental results presented in [6]. The mesh used for these computations is M_1.*

Eigenvalues and eigenvectors To validate the generalized non symmetric eigensolver, the results by Sipp and Lebedev [40] have been reproduced and are presented in figure 3.3. Sipp and Lebedev's spectrum, as presented in figure 3.3a, has been computed on a grid with the same spatial extents as those of mesh M_2, but only 864 514 degrees of freedom ($n_{\text{d.o.f.}}$), whilst the grid used

to validate the code featured a much finer mesh with $n_{\text{d.o.f.}} = 2\,069\,594$. The relevant test was to verify the correct computation of the marginally stable eigenvalue, highlighted in the plots, at the correct Reynolds number; as seen in figure 3.3, the correspondence is nearly perfect, within 1.5% of relative error. For what concerns the complete spectrum of the flow around the cylinder, the fact that Sipp and Lebedev's presents differences in the topology of the branches may lie in the different refinement of the computational domain used and in the different number of Lanczos vectors generated during the computation of the eigenvalues. In fact, the spectrum computed with mesh M_1, not reported here, is characterized by having less eigenvalues, due both to the fewer elements in the grid and the narrower boundaries, but presents smoother branches. Moreover, the leftmost branch is formed only by spurious modes, each group has the abscissa of the complex shift used when it was generated (this fact hadn't been pointed out in [40]).

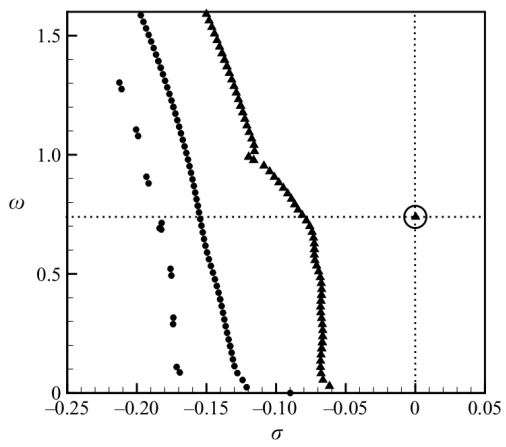

(a) *Eigenvalue spectrum computed by Sipp and Lebedev, as presented in [40], on a coarser mesh.*

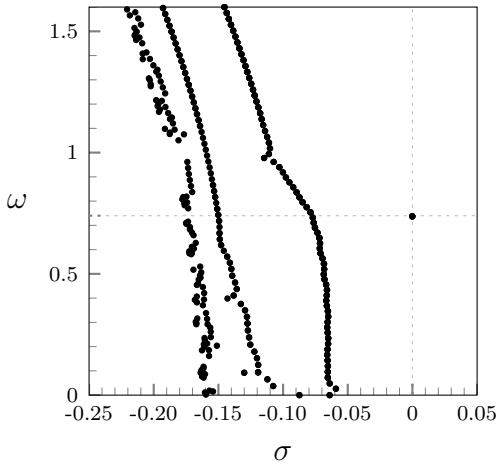

(b) *Eigenvalue spectrum computed with mesh M_2.*

Figure 3.3 *Eigenvalues of the cylinder flow in the (σ, ω) plane at $Re = 46.6$, $\alpha = 0$. The different topology of the branches may be due to the more refined mesh used during this thesis or to a difference in the number of Lanczos vectors generated. The leftmost branch (the "dashed" one) contains only spurious eigenvalues.*

The computation of both direct and adjoint eigenvectors has been verified by comparing the shape of the computed modes with those shown in [40], see figure 3.4. Once again, apart from the different scaling used for the eigenvectors, the results are in very good agreement with the reference ones.

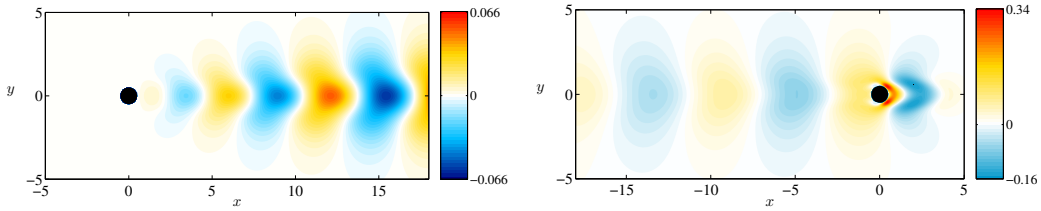

(a) *Direct eigenvector associated with the least stable eigenvector.*

(b) *Adjoint eigenvector associated with the least stable eigenvector.*

Figure 3.4 *Eigenvectors of the cylinder flow at* $Re = 46.6$, $\alpha = 0$. *The plots depict the real part of the vertical velocity component. The comparison has been done with the results of Sipp and Lebedev (see [40]) which are not reported here. Mesh* M_2, *only the portion of domain presented in the cited article is shown.*

Bifurcation tracking To test the bifurcation tracking capabilities of the program, the results by Pralits, Brandt and Giannetti [28] have been reproduced and are presented in figure 3.5. The bifurcation tracking analysis allowed the validation of the interface to the LOCA library and was one of the final checks to the code. It is well known that the flow around a nonrotating circular cylinder becomes first unstable at a Reynolds number Re = 46.6 where it exhibits a Hopf bifurcation. When increasing the angular velocity of the cylinder, the flow becomes stable again even for relatively high Reynolds numbers.

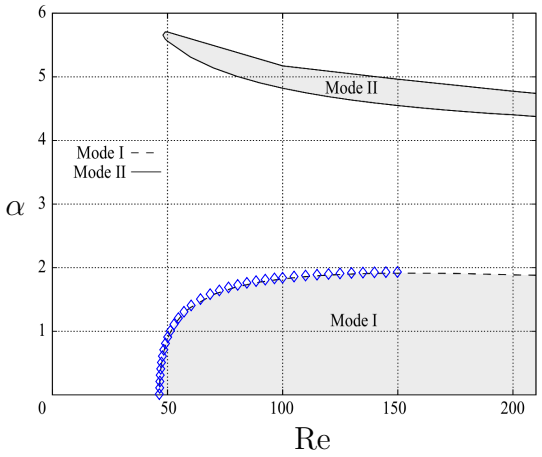

Figure 3.5 *Neutral curve of the flow around a circular rotating cylinder. The dashed (black) line is taken from [28], the diamonds (blue) are the present results. The grid used for the comparison is* M_3, *but even* M_1 *worked perfectly for* $Re \leq 100$. *Only Mode I has been reproduced.*

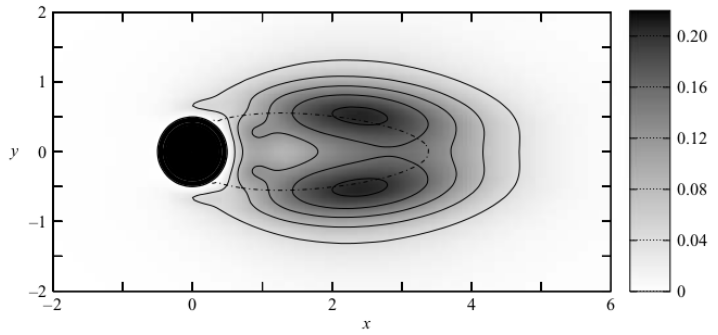

(a) *Structural sensitivity parameter computed by Giannetti and Luchini [15] using finite differences.*

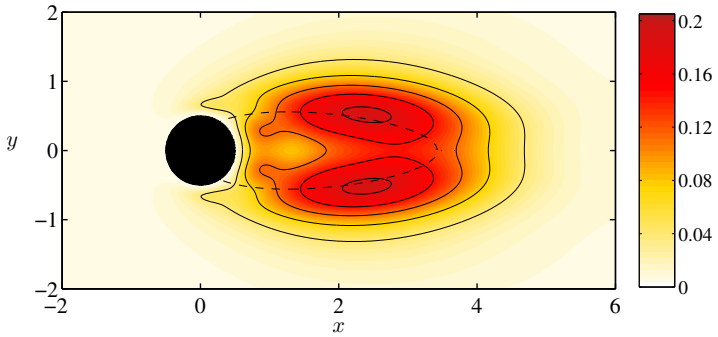

(b) *Structural sensitivity parameter computed with mesh M_3. Only the relevant portion of domain is shown.*

Figure 3.6 *Structural sensitivity of the base flow at $Re = 50$, $\alpha = 0$ computed with the developed code.*

Structural sensitivity To further validate the eigenvectors computation and to test the structural sensitivity algorithm, the results by Giannetti and Luchini [15], have been reproduced and are shown in figure 3.6 (only the structural sensitivity parameter is shown). The grid used is M_3 which features the same spatial extents as the one used in [15]; in terms of the number of elements, a direct comparison can not be made because the base flow solver used by Giannetti and Luchini is based on a finite difference, structured grid discretization of the problem; nevertheless, the results presented in their article, and reported in figure 3.6a, were computed on a grid which featured 50 points on the cylinder diameter, nearly the same precision has been obtained during this thesis using only 20 points for the FE discretization. Probably due to these differences in the discretization, there is a 12.5 % difference in the value of the maxima but the contours overlap perfectly.

Transient growth The nonrotating circular cylinder has also been used to validate the algorithm for the computation of the optimal initial disturbance. The results obtained with the developed program have been compared with those presented by Cantwell and Barkley [4] and are depicted in figure 3.7.

The computations have been carried out on mesh M_4, this mesh features the exact same extension as the one used in [4] due to the high sensitivity of quantitative results to domain size. Although M_4 is quite coarse, the results are in very good agreement with those computed by Cantwell and Barkley who have used a spectral element discretization. The time stepper used in this work employs the Crank–Nicolson method with a time step $\Delta t = 0.05$.

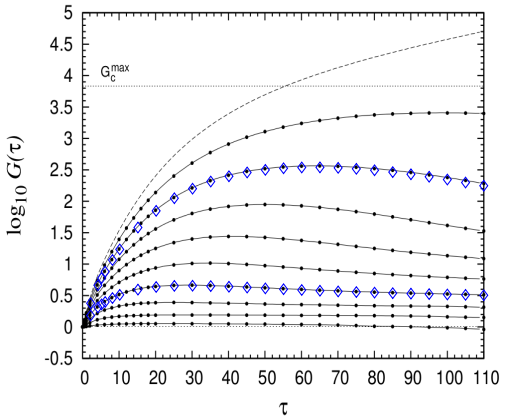

Figure 3.7 *Comparison of the optimal energy growth between the results presented in [4] (black points) and those obtained during this thesis (blue diamonds). Reynolds numbers are from* $Re = 5$ *to* $Re = 50$ *with increments of* $Re = 5$*. Only the curves at* $Re = 20$ *and* 40 *have been reproduced using mesh* M_4*.*

3.2 Flow produced in a cylindrical container by a rotating endwall

This section presents the results obtained with the first axisymmetric geometry used to verify the code. The comparison concerns the steady swirling flow produced by rotating one end wall in a closed cylindrical container completely filled with fluid. The flow behaviour is determined by two parameters: the height-to-radius ratio H^*/R^* and a rotation Reynolds number $\mathrm{Re} = \Omega^* R^{*2}/\nu^*$; H^* being the cylinder height, R^* its radius and Ω^* the angular velocity of the endwall. This test case has been chosen to validate the 3D axisymmetric FEM solver (section 2.1.1) and the algorithm for the continuation of solutions (section 2.2).

Base flow The configuration chosen is that with rotor-stator aspect ratio $H^*/R^* = 2$ at $\mathrm{Re} = 1\,850$ which is characterized by two recirculation bubbles, located on the axis at $z = 0$ and $z = 0.5$.

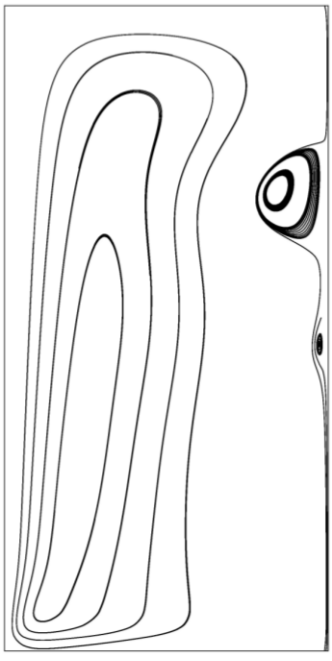

(a) *Streamlines of the velocity field taken from [2].*

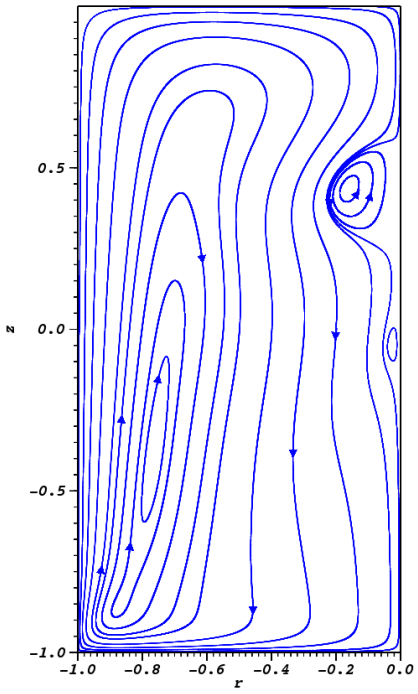

(b) *Streamlines of the velocity field computed by the 3D axisymmetric FEM solver.*

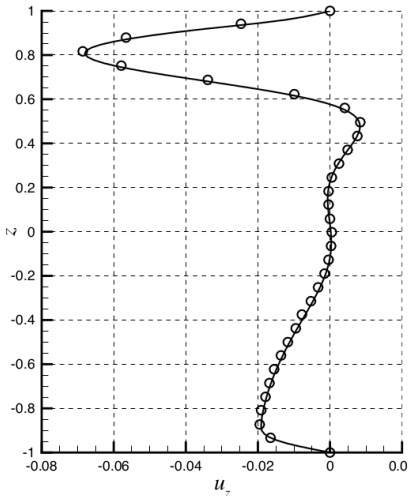

(c) *Axial velocity on the axis of rotation as reported in [2] (continuous line) and [9] (empty circles).*

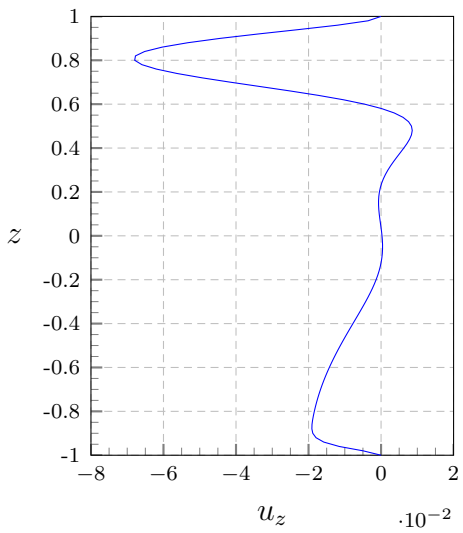

(d) *Axial velocity on the axis of rotation obtained by the 3D axisymmetric FEM solver.*

Figure 3.8 *Comparison of the results obtained for the flow produced in a cylindrical container by a rotating end wall. The physical parameters governing the flow are:* $H^*/R^* = 2$ *and* $Re = 1\,850$. *The mesh used consisted of* 46 742 *uniformly distributed elements. The steady state at* $Re = 1\,850$ *has been reached thanks to the algorithm for the continuation of solutions.*

The steady solution could not be reached by a Newton iteration employing as initial guess the solution of the Stokes problem. The algorithm for the continuation of solutions, instead, allowed to start from a low Reynolds number (200 in this case) and proceed by steps in ΔRe until reaching the desired value of 1 850. The comparisons have been done with the works presented in [2] and [12] using a uniform mesh with 46 742 elements for a total number of degrees of freedom $n_{\text{d.o.f.}} = 211\,852$.

The streamlines of the velocity field in the axial plane are shown in figure 3.8a and 3.8b, they compare very well with the results presented in [2] which have been obtained by an unsteady spectral solver for the primitive variables. A more quantitative comparison has been made by plotting the distribution of the axial velocity u_z on the cylinder axis, figures 3.8c and 3.8d; the plots are not overlapped for clarity, in fact [2] also report the values obtained by [9] (empty circles); as shown in the figure, there is a very good agreement between the profiles of u_z and, in particular, between the predicted position of the two recirculation bubbles.

3.3 Round viscous jet

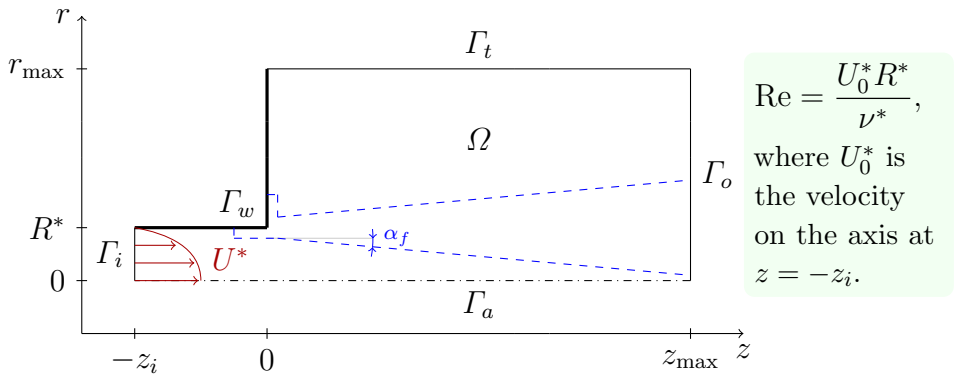

$$\mathrm{Re} = \frac{U_0^* R^*}{\nu^*},$$
where U_0^* is the velocity on the axis at $z = -z_i$.

Figure 3.9 *Geometry and mesh structure of the flow produced by a round viscous jet. Γ_i represents the inflow boundary, located at $z = -z_i$, the thick line, Γ_w, is a solid wall where no-slip boundary conditions have been assigned; Γ_t and Γ_o represent the far field and outflow boundaries, respectively, where the quasi stress-free boundary conditions have been imposed. The dashed (blue) lines enclose the area where the mesh has been refined.*

The flow produced by a round, viscous, laminar jet has been chosen to further test the program on axisymmetric geometries and to get acquainted with the behaviour of nearly parallel flows. Since the 3D axisymmetric Finite Element solver has already been tested (see previous section) the flow produced by the jet has been used to verify the computation of eigenvalues and eigenvectors and the transient growth algorithm for a problem in cylindrical coordinates.

Boundary conditions On the inflow, Γ_i, two different boundary conditions have been tested to analyze the effects of the velocity profile on the stability properties of the base flow. First, the same velocity profile used by Garnaud et al. [14], has been used to reproduce the results presented in their article,

$$\boldsymbol{u} = (U^*, 0, 0), \quad \text{where} \quad U^*(r) = \tanh\left(5\left(1 - \frac{r}{R^*}\right)\right); \tag{3.1}$$

this velocity profile, though, presents an inflection point at $r = R^*$ which could be at the origin of an instability, as shown in the next paragraph and figure 3.11. Then, the exact solution to the Navier–Stokes equations for the flow inside a round pipe (known as Poiseuille flow, see *e.g.* [29]) has been used:

$$U^*(r) = \frac{3}{2}\left(1 - \frac{r^2}{R^{*2}}\right). \tag{3.2}$$

The pressure gradient that determines the amplitude of this velocity profile has been chosen in order to have the bulk velocity $\bar{U}^* = 1$ and, in this case, the Reynolds number has been based on this quantity, *i.e.*, $\mathrm{Re} = \bar{U}^* R^* / \nu^*$. The comparison between the two velocity profiles is presented in figure 3.10.

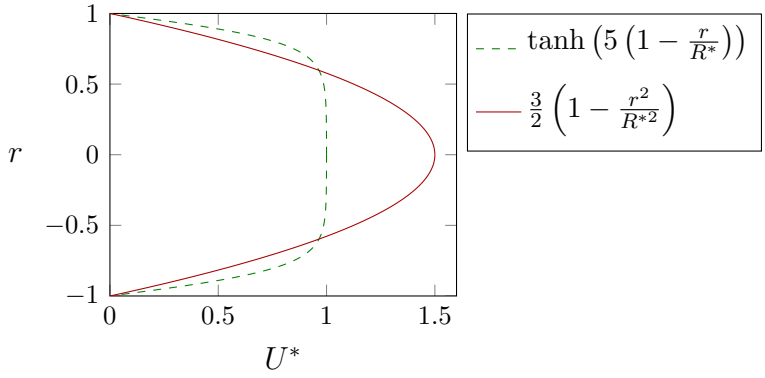

Figure 3.10 *Different velocity profiles adopted for the inflow boundary Γ_i. Dashed (green): velocity profile used in [14]; continuous line (red): exact solution to the Navier–Stokes equations known as Poiseuille flow.*

On Γ_w (thick lines), a no slip boundary condition has been assigned; on Γ_t and Γ_o, on the contrary, quasi stress-free boundary conditions have been assigned:

$$\frac{1}{\mathrm{Re}} \frac{\partial \boldsymbol{u}}{\partial \hat{\boldsymbol{n}}} - p\hat{\boldsymbol{n}} = 0.$$

As already explained in section 1.4.1, these boundary conditions are "purely mathematical" and derived from the weak variational formulation, they do represent only approximately a stress-free boundary condition because they are not applied on a surface with constant velocity. This type of boundary condition is enforced on Γ_t since it allows to correctly simulate the entrainment of fluid from infinity without having to impose an approximate velocity profile on this border.

Eigenvalues and eigenvectors The eigenvalue spectrum computed by Garnaud et al. [14] at $\mathrm{Re} = 1\,000$ has been reproduced. The spatial extent of the computational domain has been chosen taking into account the sensitivity of the problem to the length and width of the numerical domain studied in the cited article. Thus, $r_{\max}$ has been set to 10, and $z_{\max} = 60$; the mesh used featured 317 406 elements, which correspond to 2 072 740 degrees of freedom for each vector unknown $\boldsymbol{x} = (u_r, u_\theta, u_z, p)$.

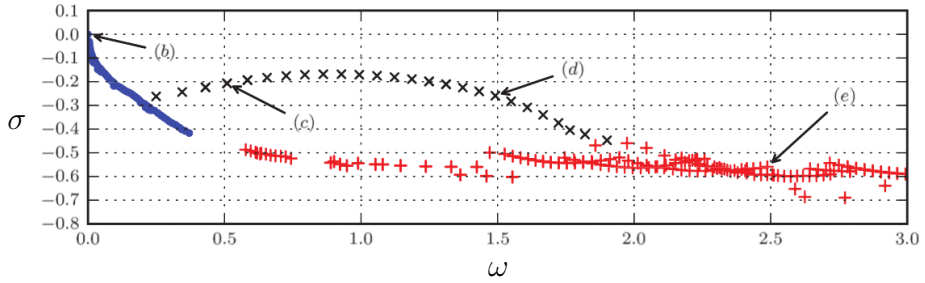

(a) *Spectrum computed by Garnaud et al. [14].*

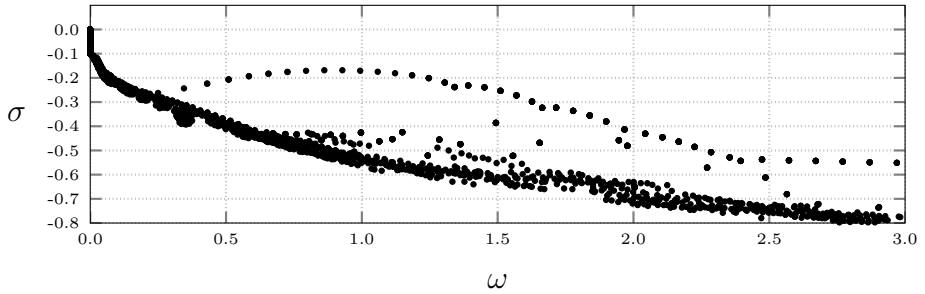

(b) *Spectrum computed using* (3.1) *as velocity profile at the inflow.*

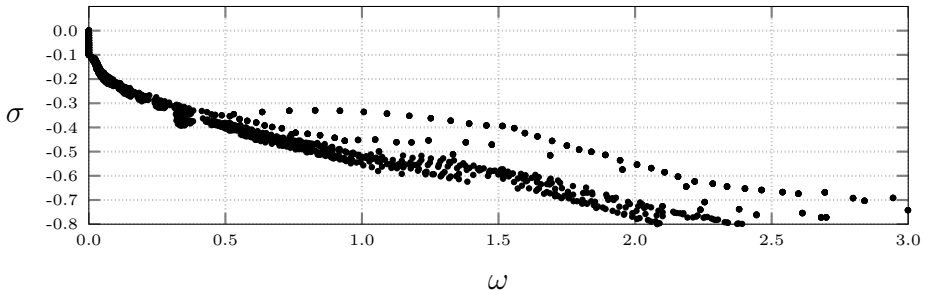

(c) *Spectrum computed using the Poiseuille velocity profile at the inflow.*

Figure 3.11 *Eigenvalues of the round, viscous jet flow in the* (σ, ω) *plane at* $Re = 1\,000$. *As noted in the case of the flow around a circular rotating cylinder (see section 3.1), the difference in the branches between* ***(a)*** *and* ***(b)*** *may be due to the different refinement of the mesh. Note how much the higher branch moves depending on the inflow velocity profile:* ***(a)*** *and* ***(b)*** *both use the velocity profile described by eq.* (3.1) *whilst* ***(c)*** *uses eq.* (3.2). *All of the eigenvalues with real part* $\sigma < -0.4$ *are spurious,* i.e., *they "move" when changing the shift.*

Transient growth As the flow produced by a round viscous jet is linearly stable (see, *e.g.* [14] and references therein) while experiments clearly show that it is unstable, the cause of its transition to turbulence can be sought for in transient growth. In fact, the transient amplification of perturbations, as shown in figure 3.12, can reach three orders of magnitude.

The reference results are those presented by Garnaud et al. [14] and have been obtained by a Finite Element discretization; the mesh used in the present work features the same spatial extents of the reference one. Due to time constraints, only the axisymmetric case has been reproduced.

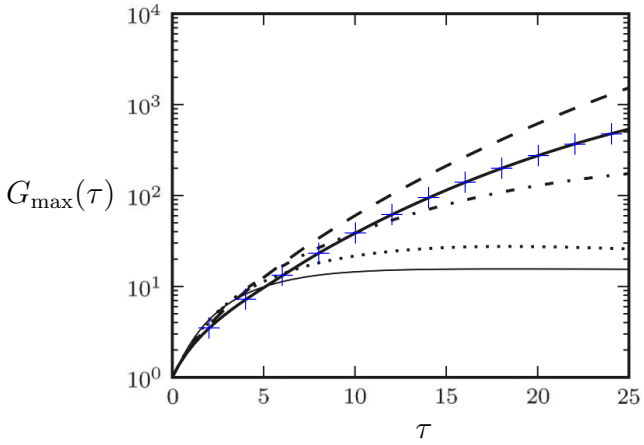

Figure 3.12 *Comparison of the optimal energy growth between the results presented in [14] (black solid line) and those obtained during this thesis (blue pluses). Note that, differently from the exposition in section 1.7, in this plot $G_{max}(\tau)$ is the square root of the ratio of kinetic energies. The Reynolds number is $Re = 1\,000$. Only the axisymmetric case has been reproduced.*

CHAPTER 4

Coaxial Jets

This Chapter describes the global stability properties of two incompressible coaxial jets. This flow has been studied by several authors, *e.g.* [8, 46, 41, 37, 39] in the past, and the aim of the present investigation is to provide new insight into the mechanisms at the origin of the observed behaviour. The tools employed in the investigation, except for the DNSs, are illustrated in Chapters 1 and 2, and have been implemented in a Fortran 2003/C code.

The exposition begins with a description of the adopted geometry and boundary conditions; a characterization of the steady state solution follows. The Hopf bifurcation encountered by the flow is discussed in section 4.3, where the results obtained by a modal stability approach are presented. The study of the bifurcation is developed in the following section, which is devoted to a portrait of the flow dynamics along the neutral curve in the Reynolds number-velocity ratio plane. The analysis of the structural sensitivity of the critical eigenmode is presented in section 4.5. Lastly, the linearly stable flow before the first bifurcation point is investigated in section 4.6 by means of transient growth analysis. The Chapter ends with a comparison of the results with DNSs and an study on the influence of domain truncation (sections 4.7, 4.8 resp.).

4.1 Geometry and boundary conditions

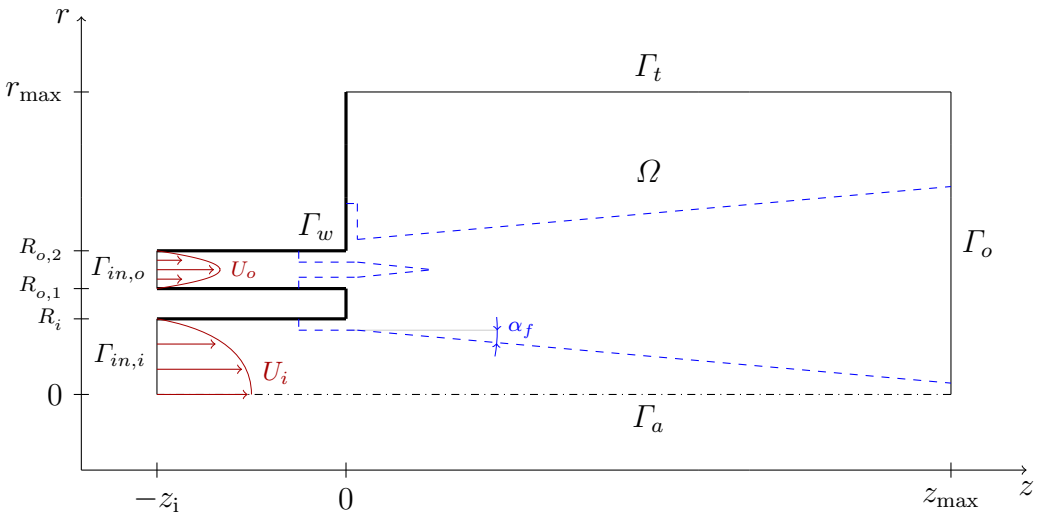

$$\mathrm{Re}_i = \frac{U_{0i} D_i}{\nu}, \qquad r_u = \frac{U_{0o}}{U_{0i}}, \qquad \beta = \frac{D_{o,2}}{D_i}, \qquad s = R_{o,1} - R_i,$$

where U_{0i} and U_{0o} are the peak velocities at $z = -z_i$

Figure 4.1 *Geometry and definition of the parameters characterizing the flow field. The dashed (blue) lines enclose the area where the mesh has been refined; mesh data is reported in table 4.1.*

The influence of the shape and thickness of the duct wall separating two coaxial jets expanding into unconfined, quiescent fluid has been investigated experimentally [3, 38, 39, 42], and by an inviscid analytical approximation [26, 41], by several authors. In particular, both a sharp and several rectangular walls have been tested and the difference between the two configurations analysed [37]. In this work the case of a wall with rectangular geometry is considered, since it provides better mixing efficiency and may lead the flow to a local or global absolute instability [41].

Geometry and discretization The same geometry used by Talamelli, Segalini et al. [38] has been employed for the computations, the only difference being the presence of a wall perpendicular to the nozzles. The set up features two converging nozzles that end in two straight pipes, the ratio between the external diameter of the annular duct and the diameter of the internal duct is fixed to $\beta = 2$, the separation wall has a thickness $s = D_i/10$.

A relevant portion of the pipes has been modelled, since their exclusion from the computational domain implies the incorrect computation of optimal

perturbations and adjoint eigenvectors. As jets are naturally described in cylindrical coordinates, only the flow field on a meridian semi-plane has been simulated, thus allowing for greatly reduced computational costs. The dashed (blue) lines in figure 4.1 enclose the area of higher mesh refinement. The characteristics of the computational grids employed are reported in table 4.1; all the meshes featured ten elements on the wall separating the two jets.

Mesh	z_i	z_max	r_max	n_e	$n_\mathrm{d.o.f.}$
M_1	5	40	5	196 530	1 287 172
M_2	5	60	5	261 295	1 709 681
M_3	5	80	5	326 344	2 134 043
M_4	5	100	5	389 588	2 546 571
M_5	5	120	5	454 746	2 971 638
M_6	5	140	5	519 612	3 394 807
M_7	5	160	5	584 999	3 821 366
M_8	5	100	10	455 805	2 977 209
M_9	5	100	15	529 701	3 457 757
M_{10}	10	100	5	452 219	2 959 731
M_{11}	15	100	5	515 040	3 374 126

Table 4.1 *Properties of the meshes used in the present work. z_i, z_{max} and r_{max} are, respectively, the location of the inlet, outlet and lateral boundaries. n_e and $n_{d.o.f.}$ are the number of elements and the number of degrees of freedom of an unknown $\boldsymbol{x} = (u_z, u_r, u_\theta, p)$, respectively.*

Boundary conditions As for the single round jet, two velocity profiles have been assigned at the inflow, to study their influence on the development of the flow field.

The first one is a family of velocity profiles depending on two parameters, b_i and b_o, determining the thickness of the boundary layer inside the pipes:

$$U_i(r) = \tanh\left(b_i\left(1 - \frac{r}{R_i}\right)\right), \tag{4.1a}$$

$$U_o(r) = \tanh\left(b_o\left(1 - \left|\frac{r - (R_{o,1} + R_{o,2})/2}{(R_{o,1} - R_{o,2})/2}\right|\right)\right). \tag{4.1b}$$

These functions have been chosen in order to reproduce the profiles measured in the experiments reported in [30, 37].

The second one is the exact solution of the Navier–Stokes equations known

as Poiseuille flow. For the central jet it assumes the usual form:

$$U_i(r) = \frac{3}{2}\left(1 - \frac{r^2}{R_i^2}\right)\bar{U}_i, \tag{4.2a}$$

which is the solution to the general equation with a single boundary condition on R_i. For the annular jet, due to the presence of the logarithmic term in the general equation and the need to impose no-slip boundary conditions both at $r = R_{o,1}$ and $r = R_{o,2}$, the solution leads to a more complicated expression:

$$U_o(r) = \frac{(R_{o,2} - R_{o,1})\left[r^2 + \frac{R_{o,2}^2 - R_{o,1}^2}{\log(R_{o,1}/R_{o,2})}\log\frac{r}{R_{o,2}} - R_{o,2}^2\right]}{R_{o,2}^2 R_{o,1} - \frac{2}{3}R_{o,2}^3 - \frac{R_{o,1}^3}{3} - \frac{R_{o,2}^2 - R_{o,1}^2}{\log(R_{o,1}/R_{o,2})}(R_{o,2} - R_{o,1} + R_{o,1}\log\frac{R_{o,1}}{R_{o,2}})}\bar{U}_o. \tag{4.2b}$$

These velocity profiles have been adimensionalised with the bulk velocity $\bar{U} = \int_0^R U(r)\,\mathrm{d}r$, which has consequently been used to define the Reynolds number, *i.e.*, $\mathrm{Re} = \bar{U}R/\nu$. However, the results obtained with the Poiseuille flow are still incomplete, therefore they are not included in this work.

The thick lines in figure 4.1, denoted by Γ_w, represent solid walls where a no-slip boundary condition has been assigned. On the outflow and radial borders (Γ_o and Γ_t respectively), the quasi stress-free boundary condition, discussed in section 1.4, has been enforced, namely,

$$\frac{1}{\mathrm{Re}}\frac{\partial \boldsymbol{u}}{\partial \hat{\boldsymbol{n}}} - p\hat{\boldsymbol{n}} = 0.$$

As the goal is to model jets expanding into free, quiescent air, assigning this boundary condition on the radial border allows to simulate the *entrainment* of air by the two jets without having to impose an analytical velocity profile (see, *e.g.* [34]) as far-field boundary condition.

4.2 Base flow

When employing the hyperbolic tangent profile (4.1), the velocity profile at the exit of the pipes is moderately different from the one imposed on Γ_{in}; in particular, the peak velocities are increased by 10%-30% and the shape of the profile tends to a parabola. This is due to the growth of the boundary layer inside the pipes, which is especially relevant at the low Reynolds numbers where the first instability is observed; this effect is depicted in figures 4.2a and 4.2b. Despite the substantial increase in peak velocity, the velocity ratio at the

nozzles is not significantly altered, as both jets are affected by a comparable boundary layer growth.

The effect of the rectangular duct wall is maximum close to the jet exit and it determines the presence of a backflow region typical of blunt bodies. Differently from wake flows, though, this effect is lost at approximately 40-100 diameters (depending on the Reynolds number) downstream of the nozzles, where the two jets merge and acquire the shape of a single jet.

The base flow is weakly nonparallel: the radial velocity component is approximately three orders of magnitude lower than the axial one. However, as shown in figure 4.2c, variations to the radial velocity profile are not as slow as they are usually assumed to be (see, *e.g.* [41]), especially in the proximity of the nozzles. This rapid variation is, of course, mainly due to the wake generated behind the blunt wall separating the jets, but it is also influenced by the entrainment of fluid caused by the faster jet.

The evolution of the base flow has been studied for different velocity ratios, the case of $r_u = 1$ is here briefly presented as an example. In this regime a first vortex ring is formed for $300 < \mathrm{Re}_i < 350$. This vortex ring is located in the lower part of the rectangular wall and is indicated with a in figure 4.2d. For higher Reynolds numbers ($\mathrm{Re}_i \approx 2\,000$) a second, slender ring appears behind the upper part of the wall, at a distance comparable to the height of the wall (indicated with b in figure 4.2d). When the Reynolds number is further increased, the second vortex ring stretches and approaches the wall but never reaches it, even for Re_i as high as 10 000.

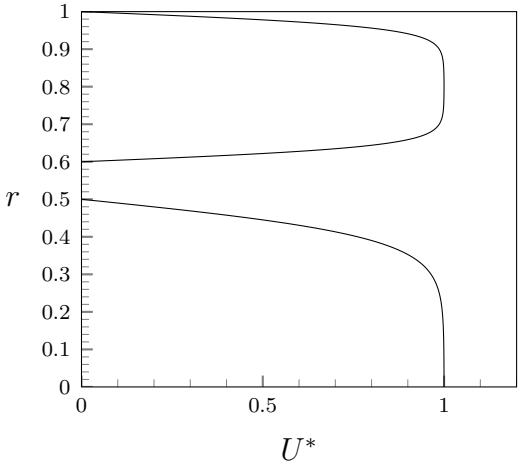

(a) *Inflow velocity profile* (4.1).

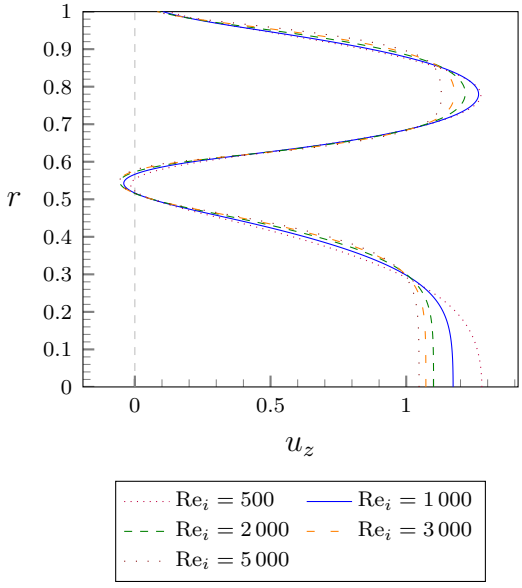

(b) *Velocity profile at* $z = 0.1$ *for different Reynolds numbers.*

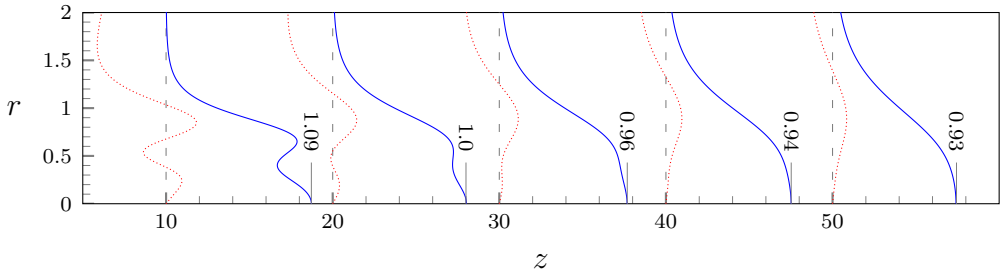

(c) *Axial (continuous blue line) and radial (dotted red line) velocity profiles at five axial positions. The magnitude of the radial velocity profile is amplified by a factor of 125 to make it visible. The Reynolds number is* $Re_i = 1\,000$.

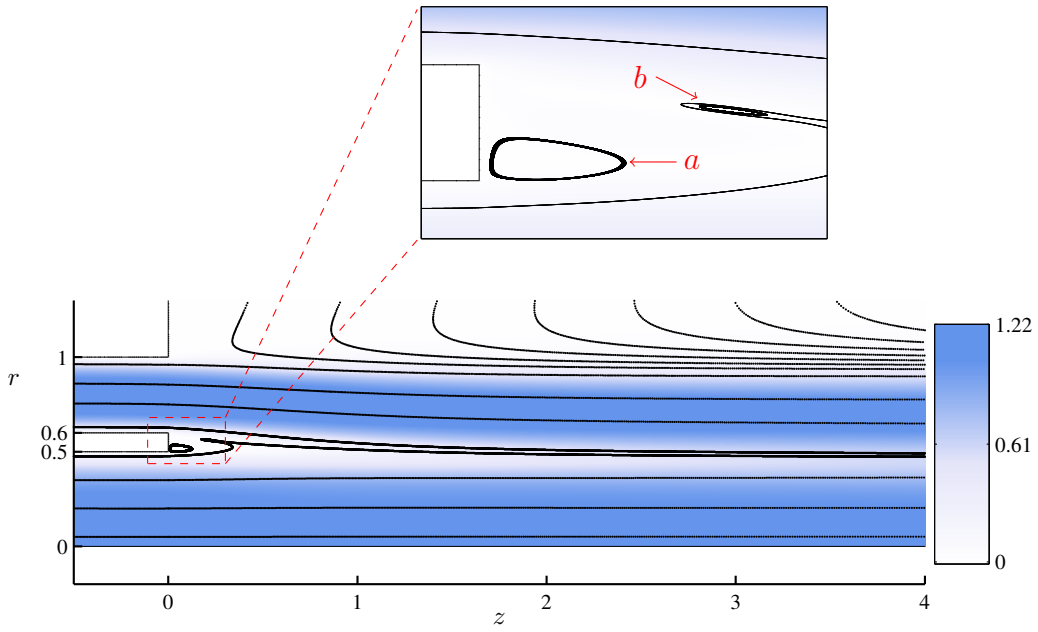

(d) *Velocity magnitude and streamlines at* $Re_i = 2\,000$, $r_u = 1$. *Two recirculating vortex rings are highlighted by* a *and* b. *The entrainment of fluid from the surrounding, quiescent medium can be observed.*

Figure 4.2 *Base flow properties for* $r_u = 1$. *The entrainment of the annular jet towards the central one can be observed by examining the radial velocity profiles in* ***(c)*** *(for* $z \leq 20$*) and the streamlines in* ***(d)***. *Mesh* M_{11}.

4.3 Hopf bifurcation and modal stability

The calculation of the eigenvalues associated with the linearized Navier–Stokes equations for $\mathrm{Re}_i = 1\,420$ and $r_u = 1$, revealed the presence of a marginally stable eigenvalue and three main groups of eigenvalues. This eigenspectrum is plotted in figure 4.3, where the critical eigenvalue, which in this configuration has imaginary part $\omega_c = 5.728$, is evidenced by the dotted lines, and the branches are labelled with b_i.

A first branch, starting at the origin and indicated in the figure by b_1, corresponds to vortical structures located in the region surrounding the jets. Eigenvalues of this kind are typical of nearly-parallel flows (see, *e.g.* [36]), they usually represent a discrete approximation of a continuous branch and are stable for any value of the parameters describing the flow field. A second branch (b_2) represents modes localized within the jets. This family of eigenvalues is highly sensitive to domain truncation effects, which are investigated in detail in section 4.8. Branches b_1 and b_2 are also present in the spectrum of a single jet, see section 3.3, and their eigenvalues are always fully resolved. The third branch (b_3) contains poorly converged eigenvalues which are not recovered when changing the shift.

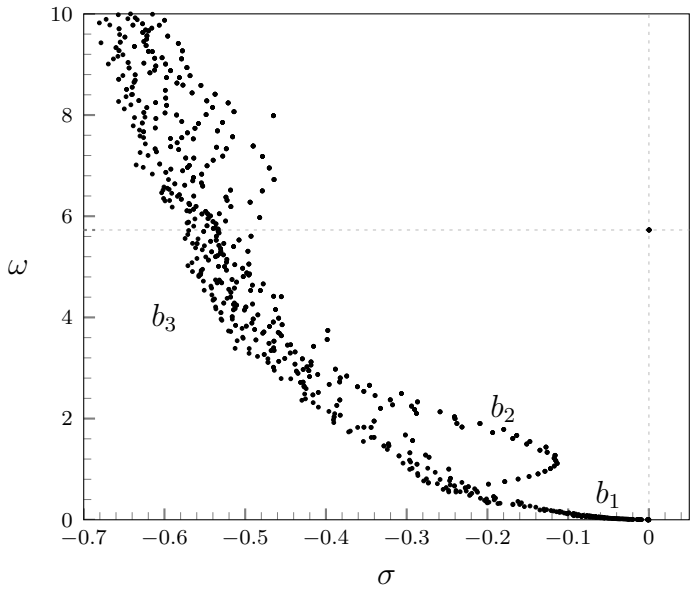

Figure 4.3 *Eigenspectrum for $Re_i = 1\,420$ and $r_u = 1$ (point A_2 in figure 4.5). A marginally stable eigenvalue exists for $\omega_c = 5.728$ (highlighted by the dotted lines). Mesh M_2.*

The frequency of the critical eigenvalue corresponds very well to the frequency of vortex shedding determined by Direct Numerical Simulation, see

section 4.7. Such an agreement is kept for quite a broad range of Reynolds numbers, at least up to $\mathrm{Re}_i = 2\,000$, since the frequency of the shedding remains nearly constant when moderately increasing Re_i while maintaining r_u constant, as shown in figure 4.14.

The velocity components corresponding to the real part of the direct eigenmode are depicted in figures 4.4a and 4.4b. This eigenvector represents an array of counter-rotating vortex rings which develop in the wake of the separation wall, similarly to what is observed for the evolution of the optimal disturbances, which will be presented in section 4.6. It can be observed that the eigenmode is strongest in the near-wake of the wall and reaches a maximum for $z \approx 11$; downstream of this location, the eigenmode is attenuated and slowly decays. This may be explained by considering the distribution of the axial velocity of the base flow, which is represented by continuous (blue) lines in figure 4.2c. In fact, it can be noticed that the counter-flow, which is responsible for the instability, is maximum in the near-wake and then slowly decreases due to viscous diffusion. A last observation is that the structure of the direct eigenvector is qualitatively unchanged across its axial span, even though the base flow velocity profile shifts from that of a coaxial jet configuration to that of a single jet.

The adjoint eigenvector is represented in figures 4.4c and 4.4d. It is localized in the $z < 1$ region and, in particular, inside the pipes. It reaches maximum intensity in the proximity of the wall, displaying two lobes nearly symmetrically distributed across the separation wall, then slowly decays in the upstream region. For $r_u = 1$, both direct and adjoint eigenvectors closely resemble those observed in flows around bluff bodies, this similarity is most certainly attributable to the rectangular geometry of the duct wall located in between the jets.

As already mentioned in section 1.6, the large spatial separation of the direct and adjoint eigenvectors is a consequence of the nonnormality of the LNSE operator, evidenced for this regime in section 4.6.

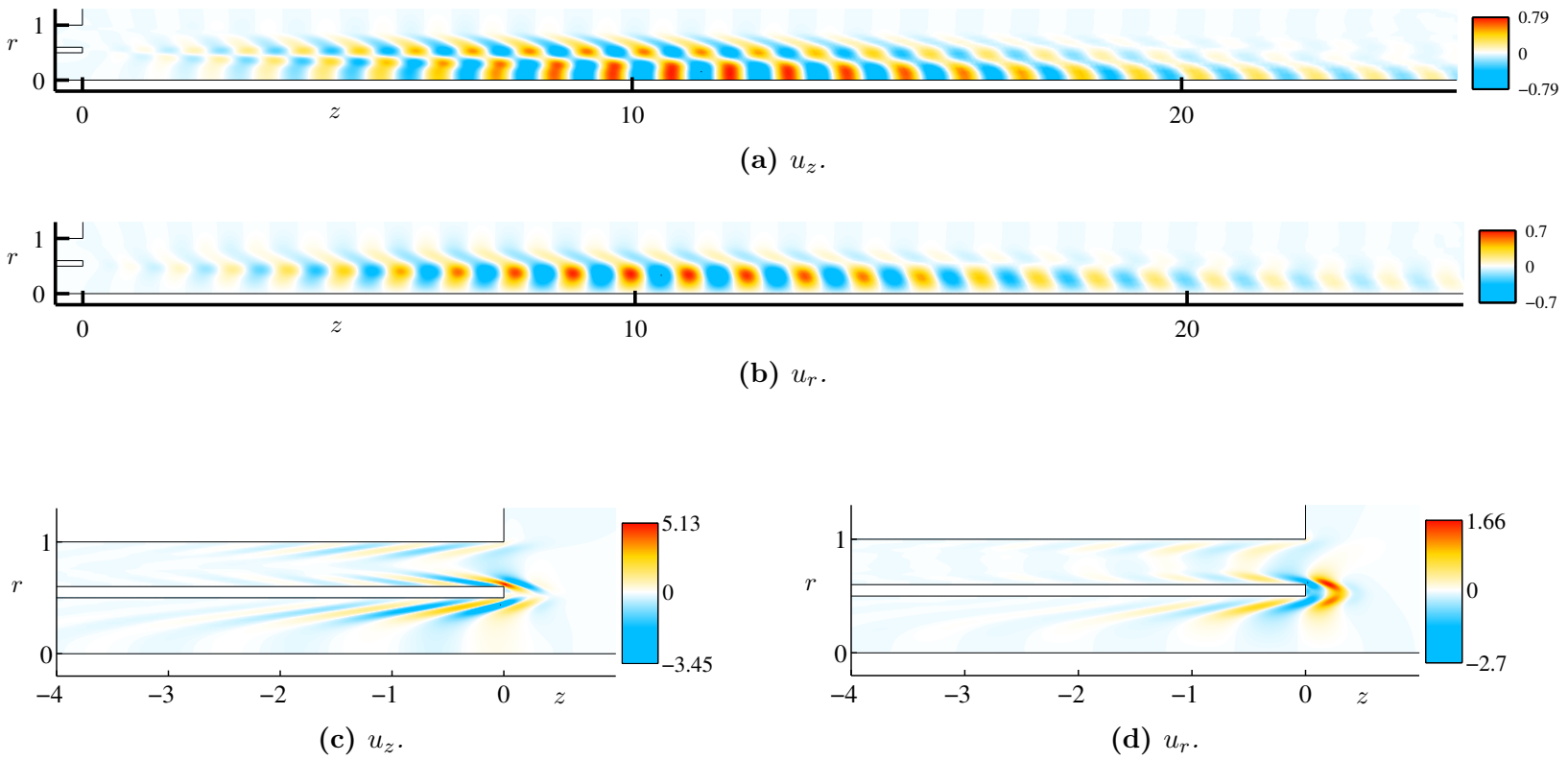

Figure 4.4 *Real part of the direct (**(a)** and **(b)**) and adjoint (**(c)** and **(d)**) critical eigenvectors for $Re_i = 1\,420$, $r_u = 1$. Point A_2 in figure 4.5. Mesh M_{11}.*

4.4 Tracking the bifurcation: influence of the velocity ratio

As illustrated in the previous section, coaxial jets undergo a Hopf bifurcation at $\mathrm{Re}_i = 1\,420$, $r_u = 1$. This is just one point in the four-dimensional space defined by the parameters characterizing the flow; to deeply understand the behaviour of coaxial jets, the parameter space should be thoroughly explored. This section describes the two-dimensional projection of the parameter space onto the $\mathrm{Re}_i - r_u$ plane, depicted in figure 4.5. This plane contains a neutral curve that separates the Stable semi-plane from the Unstable semi-plane.

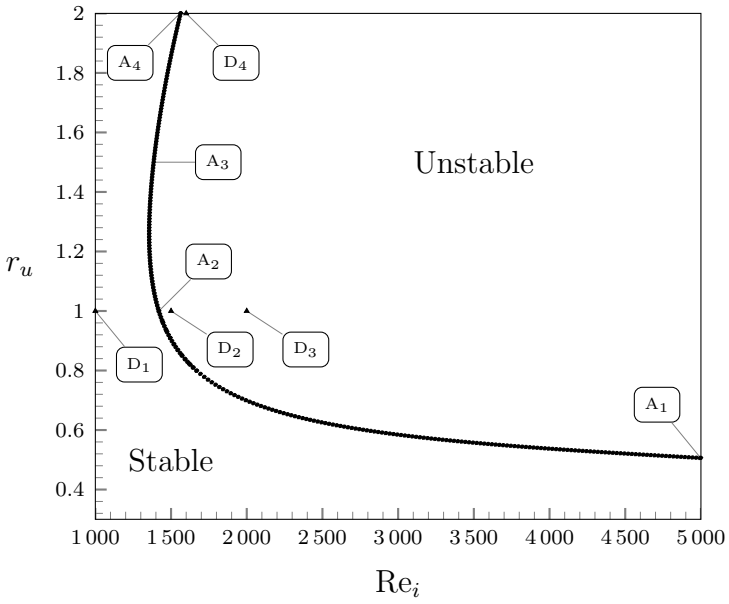

Figure 4.5 *Neutral curve in the $Re_i - r_u$ plane. The (nearly undistinguishable) points indicate the computed values. Labels A_i highlight the values at which the analysis presented in this chapter have been performed. Triangles D_i indicate points where DNSs have been performed. Meshes M_1, M_2 and M_4.*

The lower ($r_u < 1$) part of the neutral curve tends towards a horizontal asymptote, located at $r_u \approx 0.505$, where the flow approaches the single jet configuration. The presence of an asymptote agrees with the results obtained for isothermal jets, which are known to be linearly stable for all Reynolds numbers (see, *e.g.* [14] and the references therein). The eigenspectrum computed at point A_1 is depicted in figure 4.7, where the resemblance with the spectrum of a single jet can be observed (see section 3.3). The structural sensitivity of the critical eigenvalue computed in this configuration is presented and discussed in section 4.5.

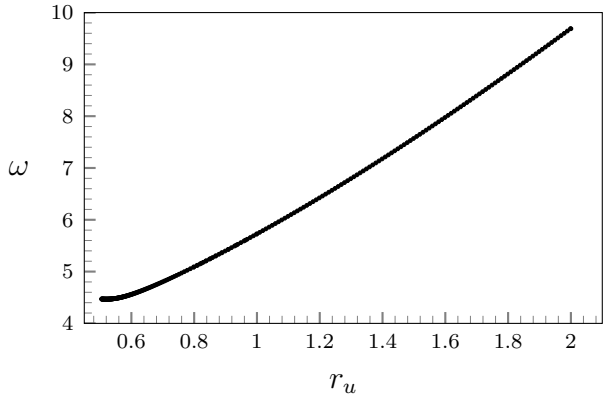

Figure 4.6 *Imaginary part of the marginally stable eigenvalue computed along the neutral curve, here plotted as a function of the velocity ratio. The trend is nearly linear, except for very low values of r_u where it appears to converge to $\omega_c = 4.47$.*

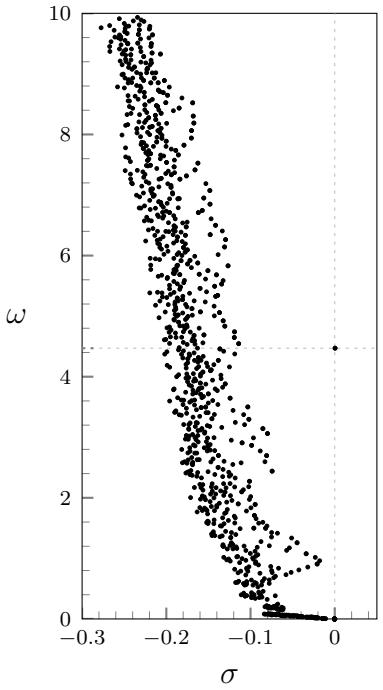

Figure 4.7 *Eigenspectrum for $Re_i = 5\,000$ $r_u = 0.5$ (point A_1 in figure 4.5). The imaginary part of the critical eigenvalue (highlighted by the dotted lines) is $\omega_c = 4.47$. In this configuration the eigenspectrum closely resembles that of a single jet, analysed in section 3.3. Mesh M_2.*

On the other hand, the upper part of the neutral curve ($r_u > 1$) presents a minimum Reynolds number ($\mathrm{Re}_i \approx 1\,356$). Below this value no instability occurs in the range of r_u explored during this research. This region of the neutral curve presents other characteristic features: as the velocity ratio is increased, the eigenspectrum changes. In particular, branch b_2 shifts towards the imaginary axis, reaching it, when using mesh M_2, for $r_u = 2$, $\mathrm{Re}_i = 1559$ (see fig. 4.8). Note however that, as explained in more detail in section 4.8, branch b_2 and its structural sensitivity are highly sensitive to domain truncation effects. As a consequence, the point on the neutral curve where branch b_2 becomes unstable is highly mesh-dependent. These observations suggest that the eigenvalues of branch b_2 are not representative of physical flow features and are probably a numerical artifact. At the moment of writing, a DNS is being performed in order study the nonlinear behaviour of the flow in this region of the neutral curve (point D_4). A frame of this simulation is depicted in figure 4.16.

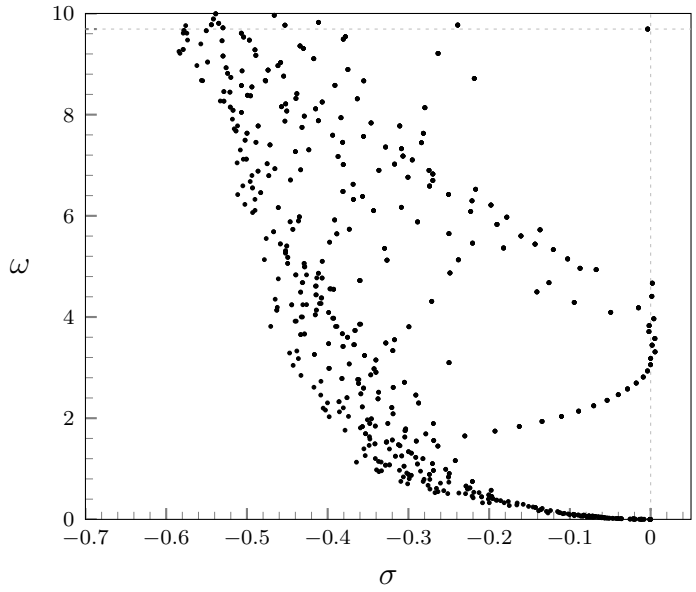

Figure 4.8 *Eigenspectrum for $\mathrm{Re}_i = 1\,559$ $r_u = 2$ (point A_4 in figure 4.5). The marginally stable eigenvalue has shifted to $\omega_c = 9.69$ (highlighted by the dotted lines) and branch b_2 has also become unstable. Mesh M_2.*

Another qualitative difference that occurs between points A_2 and A_4 is the change in the flow pattern originated by the instability behind the duct wall. DNSs show that the wake gradually switches from a von Kármán vortex-street to the pattern produced by a Kelvin–Helmoltz instability. In this configuration the shape of the critical eigenvectors is modified (compare figures 4.9 and 4.4) and also the spatial distribution of the structural sensitivity parameter is greatly altered (see fig. 4.10d).

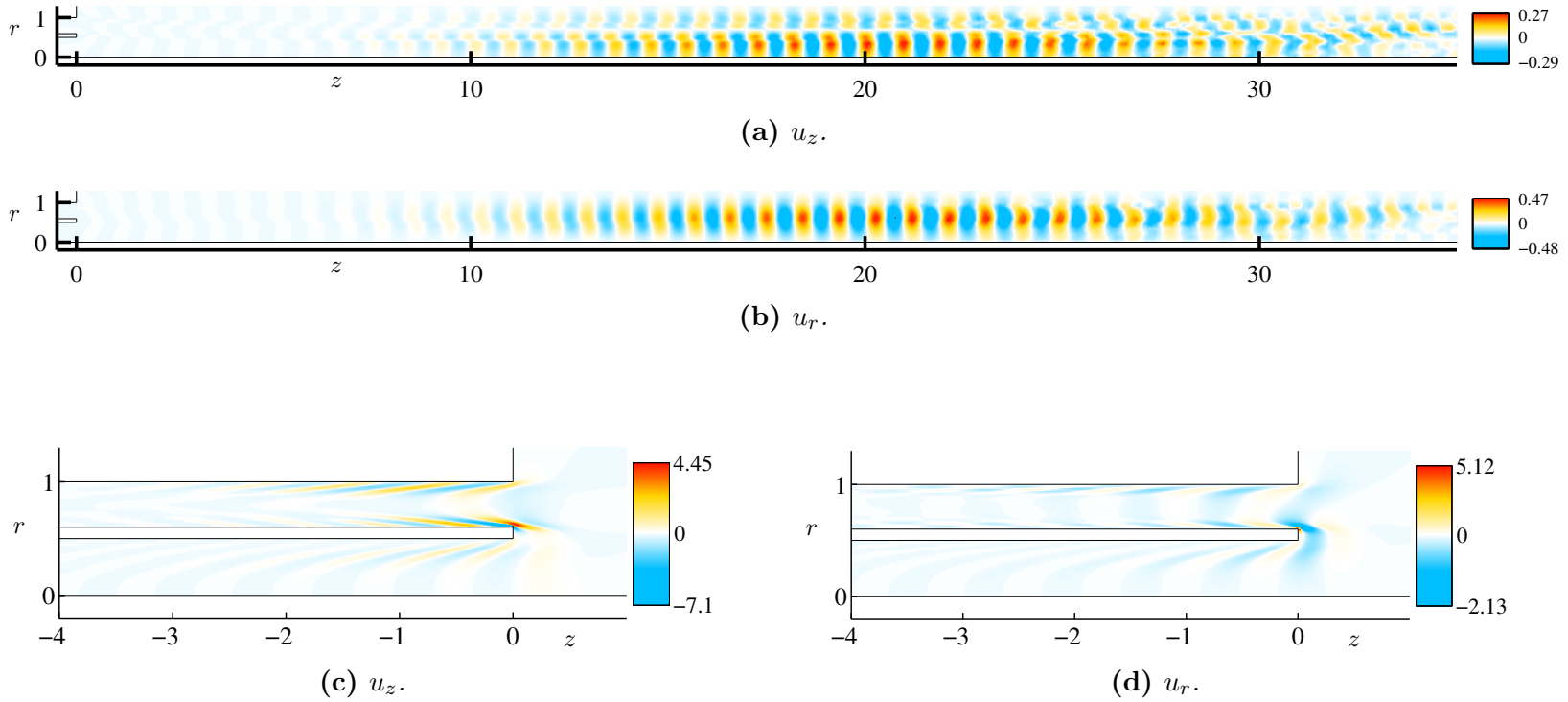

(a) u_z.

(b) u_r.

(c) u_z.

(d) u_r.

Figure 4.9 *Real part of the direct (**(a)** and **(b)**) and adjoint (**(c)** and **(d)**) critical eigenvectors for* $Re_i = 1\,559$, $r_u = 2$. *Point* A_4 *in figure 4.5. Mesh* M_{11}.

4.5 Structural sensitivity of the critical eigenmode

The large difference between the spatial structure of the direct and adjoint eigenvectors, evidenced in the two previous sections, prevents to draw relevant conclusions on the location of the core of the instability. Owing to these observations, an analysis of the structural sensitivity of the unstable eigenvalue to spatially localized velocity feedbacks is here presented. The objective of this study is to identify the location of the 'wavemaker', *i.e.*, the area of the flow field where the instability mechanism is acting.

Figure 4.10 depicts the scalar field of the structural sensitivity parameter, $s(\boldsymbol{r})$ defined in (1.11), computed at different points in the $\mathrm{Re}_i - r_u$ plane. The maxima of $s(\boldsymbol{r})$ are attained in two lobes located behind the edges of the separation wall. It can be observed that for $r_u = 1$, fig. 4.10b, they are disposed nearly symmetrically across the midline of the wall, similarly to what happens for bluff bodies. The symmetry is not perfect because the velocity profiles at the nozzles, and thus the boundary layers, are not symmetrical at low Reynolds numbers, as highlighted in figure 4.2b. Note that, in any case, the product of the direct and adjoint modes is small both in the pipes and far from the nozzles, showing that these areas of the flow are of little importance for the instability dynamics.

When varying the velocity ratio, the symmetry between the lobes is lost and the maximum of the structural sensitivity parameter shifts towards the jet flowing at higher speed. In these configurations the vortex dynamics resembles more and more the one produced by a Kelvin–Helmoltz instability. When the velocity ratio is increased above $r_u = 1.5$, fig. 4.10d, the value of the structural sensitivity parameter increases in the inner shear layer, highlighting a modification of the region where the 'wavemaker' is located. The peculiarities of this configuration have been highlighted in the previous section, where the eigenspectrum and the critical eigenvectors are also presented.

An analysis of the robustness of the structural sensitivity analysis with respect to the size of the computational domain has been performed studying the influence of domain truncation, as presented in section 4.8. It has been observed that the drift of the marginally stable eigenvalue is consistently small across the range of $z_{\max}$ tested; this is expected since all the domains used during this investigation entirely include the instability core.

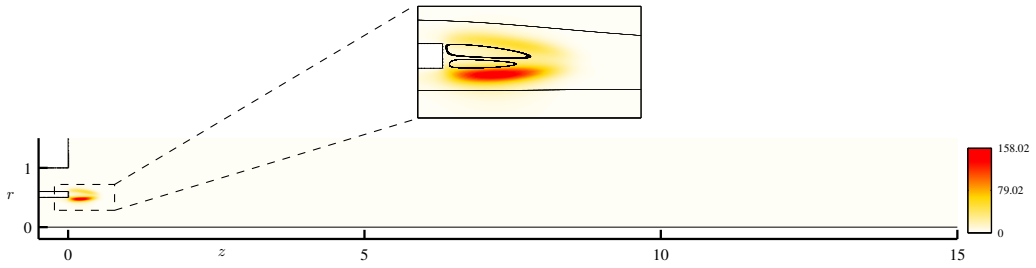

(a) $Re_i = 5\,000$, $r_u = 0.5$.

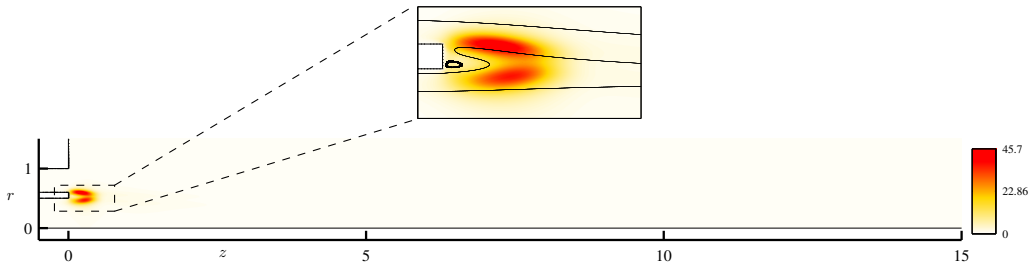

(b) $Re_i = 1\,420$, $r_u = 1$.

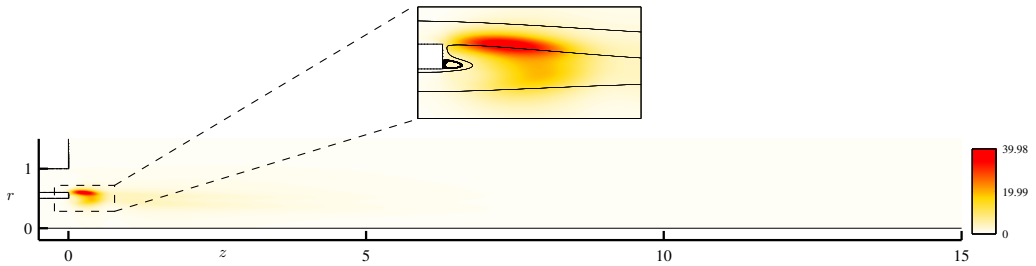

(c) $Re_i = 1\,386$, $r_u = 1.5$.

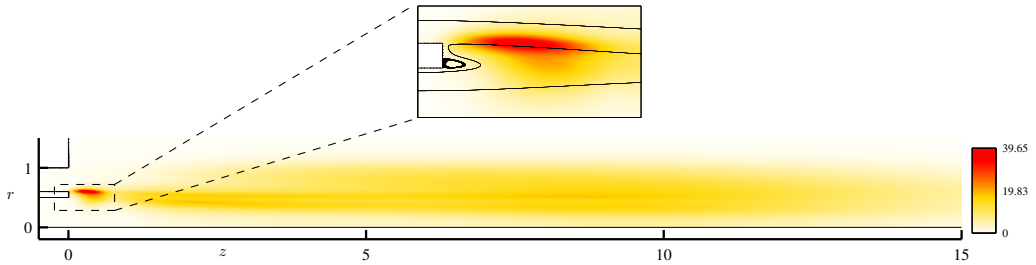

(d) $Re_i = 1\,559$, $r_u = 2$.

Figure 4.10 *Structural sensitivity of the marginally stable eigenvalue to a spatially localized feedback. Mesh* M_{11}*. In order, points* A_1 *to* A_4 *in fig. 4.5.*

4.6 Subcritical behaviour: transient growth analysis

The transient response of perturbations has been studied before the onset of the global mode described in section 4.3. This section presents the results attained for $r_u = 1$, when the development of a von Kármán vortex-street is observed in the wake of the separation wall for $\mathrm{Re}_i > 1420$.

Figure 4.11 depicts the optimal growth envelopes for three Reynolds numbers. It is observed that large transient growth may occur in this regime, in fact, the kinetic energy of infinitesimal perturbations is amplified by up to twelve orders of magnitude for the higher Reynolds number investigated. This substantial growth is representative of the amplifier nature of jet flows but is much higher than that of a single jet (see section 3.3). Unfortunately, no experimental observations for low Reynolds numbers have been found in the literature; it would be important, to understand jet dynamics, to know whether oscillations promoted by transient growth are observed before the bifurcation, or if the flow is stable as predicted by the modal stability analysis.

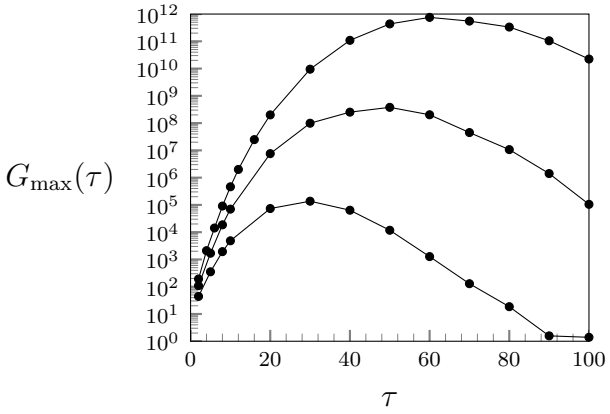

Figure 4.11 *Optimal energy growth at Reynolds numbers* $Re_i = 500, 750, 1\,000$ *(dotted, dashed and continuous lines respectively). The velocity ratio is* $r_u = 1$*. The mesh used to compute these values is* M_{11}*.*

The spatio-temporal evolution of perturbations has also been analysed. To do so, the optimal initial conditions calculated for maximum linear energy growth have been evolved via the Linearized Navier–Stokes equations (1.7). Even though, as was made clear in section 1.7, the initial condition and its subsequent evolution depend on the time horizon τ, the transient dynamics are qualitatively very similar in a substantial range of τ values, as can be observed by comparing figures 4.12 and 4.13. This suggests that similar flow dynamics are excited by initial conditions optimized across a large range of τ

values, and that the spatial structure of the optimal initial condition is nearly τ-independent.

Visualizations of the optimal condition and its evolution are reported in figures 4.12 and 4.13. The plots depict the kinetic energy, $|\boldsymbol{u}|^2/2$, of the initial condition and its evolution for $\mathrm{Re}_i = 500$, $\tau = 30$ (figures 4.12a, 4.12b) and $\mathrm{Re}_i = 1\,000$, $\tau = 60$ (figures 4.13a, 4.13b). It is observed that the initial condition is mainly localized on the outer edges of the nozzles of both jets, while the inner edge of the annular jet plays only a minor role. The perturbation evolves in a series of counter-rotating vortex rings which are advected downstream by the base flow. The streamlines relative to the superimposition of the base flow and of the perturbations are shown in figures 4.12c and 4.13c.

The importance of the outer annular edge, evidenced in figures 4.12a and 4.13a, is lost after the bifurcation, as explained in sections 4.3 and 4.5. It could be argued that, before the onset of the instability, both shear layers play a relevant role in the amplification of perturbations while, when the global mode sets in, it dominates the dynamics of the flow by significantly increasing the amplification characteristics of the wall wake and the inner shear layer. This conjecture is supported by the observations allowed by DNSs that will be presented in section 4.7.

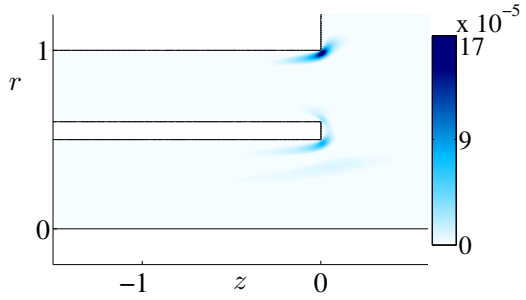

(a) *Kinetic energy of the optimal disturbance for* $Re_i = 500$, $\tau = 30$.

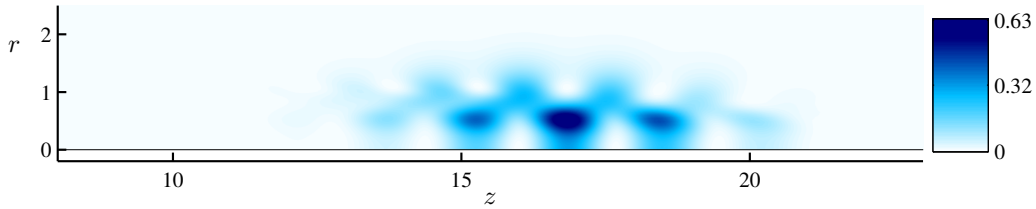

(b) *Kinetic energy of the evolution of the optimal initial condition depicted in* ***(a)***.

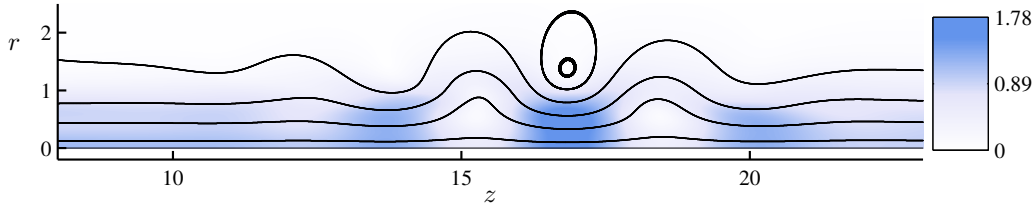

(c) *Velocity magnitude and streamlines of the superimposition of the base flow and of the optimal perturbation depicted in* ***(b)***, *namely* $\boldsymbol{U} + \epsilon \boldsymbol{u}'$, *where* $\epsilon = 8 \cdot 10^{-1}$.

Figure 4.12 *Optimal disturbance and its evolution for* $Re_i = 500$, $r_u = 1$. *Mesh* M_{11}.

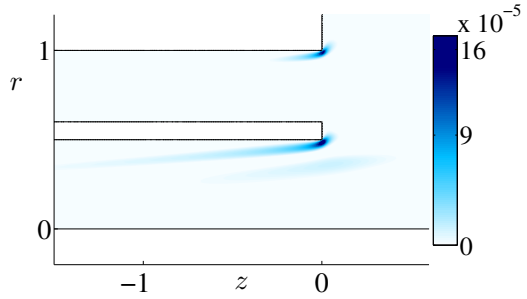

(a) *Kinetic energy of the optimal disturbance for* $Re_i = 1\,000$, $\tau = 60$.

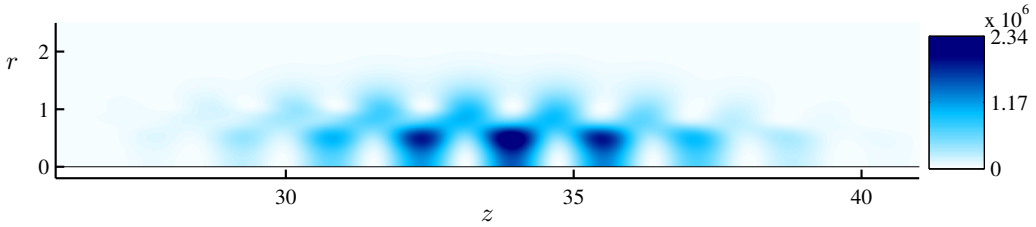

(b) *Kinetic energy of the evolution of the optimal initial condition depicted in* ***(a)***.

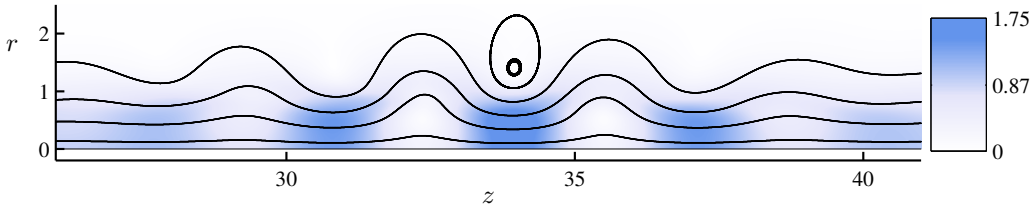

(c) *Velocity magnitude and streamlines of the superimposition of the base flow and of the optimal perturbation depicted in* ***(b)***, *namely* $\boldsymbol{U} + \epsilon \boldsymbol{u}'$, *where* $\epsilon = 4 \cdot 10^{-4}$.

Figure 4.13 *Optimal disturbance and its evolution* $Re_i = 1\,000$, $r_u = 1$. *Mesh* M_{11}.

4.7 Nonlinear simulations

Direct Numerical Simulations have been performed to assess the validity of the results attained with linear theory. In particular, the critical value of the parameters at which the bifurcation occurs and the dynamics of the unstable flow have been investigated.

Good agreement has been found in both cases: the fixed point represented by the steady state solution becomes unstable when crossing the neutral curve (fig. 4.5) and a new invariant set of the Navier–Stokes equations appears in the form of a stable limit cycle. This confirms the results of modal stability and bifurcation theory, which predict a Hopf bifurcation, with a period related to the imaginary part of the marginally stable couple of complex conjugate eigenvalues. In fact, the measured vortex-shedding frequency, plotted in figure 4.14 for $r_u = 1$, $\mathrm{Re}_i = 1\,500$, corresponds to an angular frequency $\omega_{DNS} = 5.84$ which differs from the imaginary part of the critical eigenvalue by only 1.85%.

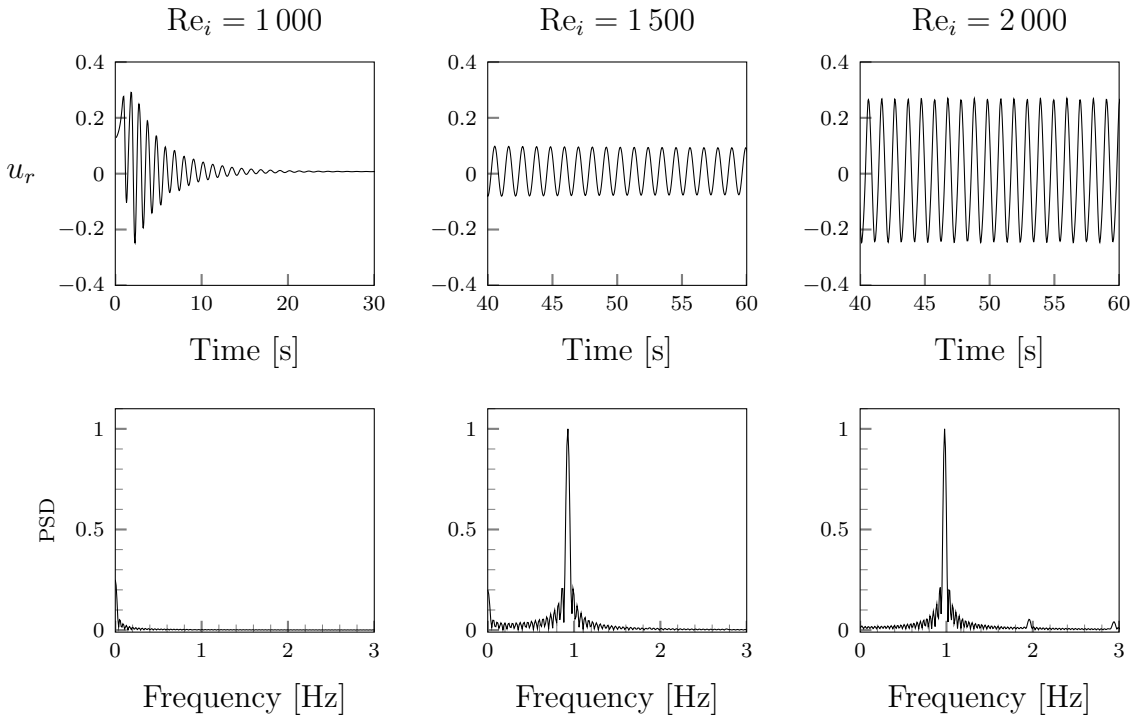

Figure 4.14 *Time signal of the radial velocity component for different Reynolds numbers measured at $z = 0.4$, $r = 0.51$ and related power spectral density. $r_u = 1$, points D_1, D_2, D_3 in fig. 4.5.*

Moreover, the oscillating flow field at $r_u = 1$, presents a pattern very similar to the one of the von Kármán vortex street behind a circular cylinder, see figure 4.15. This vortex dynamics is accurately captured by the shape of the direct critical eigenvector, which present a series of counter-rotating vortex rings.

On the other hand, in the DNS performed at $\mathrm{Re}_i = 1\,600$, $r_u = 2$, point D_4 in fig. 4.5, the von Kármán vortex-street is replaced by a flow pattern more similar to the one produced by a Kelvin–Helmoltz instability. This transition is associated with the modification of the direct eigenvector and of the structural sensitivity parameter corresponding to the marginally stable eigenvalue, as was evidenced in sections 4.4 and 4.5. Moreover, a recirculating bubble forms a few diameters downstream the nozzles. The appearance of this reverse flow region has been observed in experiments [30] for $5 < r_u < 8$. It has been evidenced, though, that the bubble oscillates and rotates, leading to the 3-dimensionality of the flow; ergo, an axisymmetric analysis might be inappropriate in this regime.

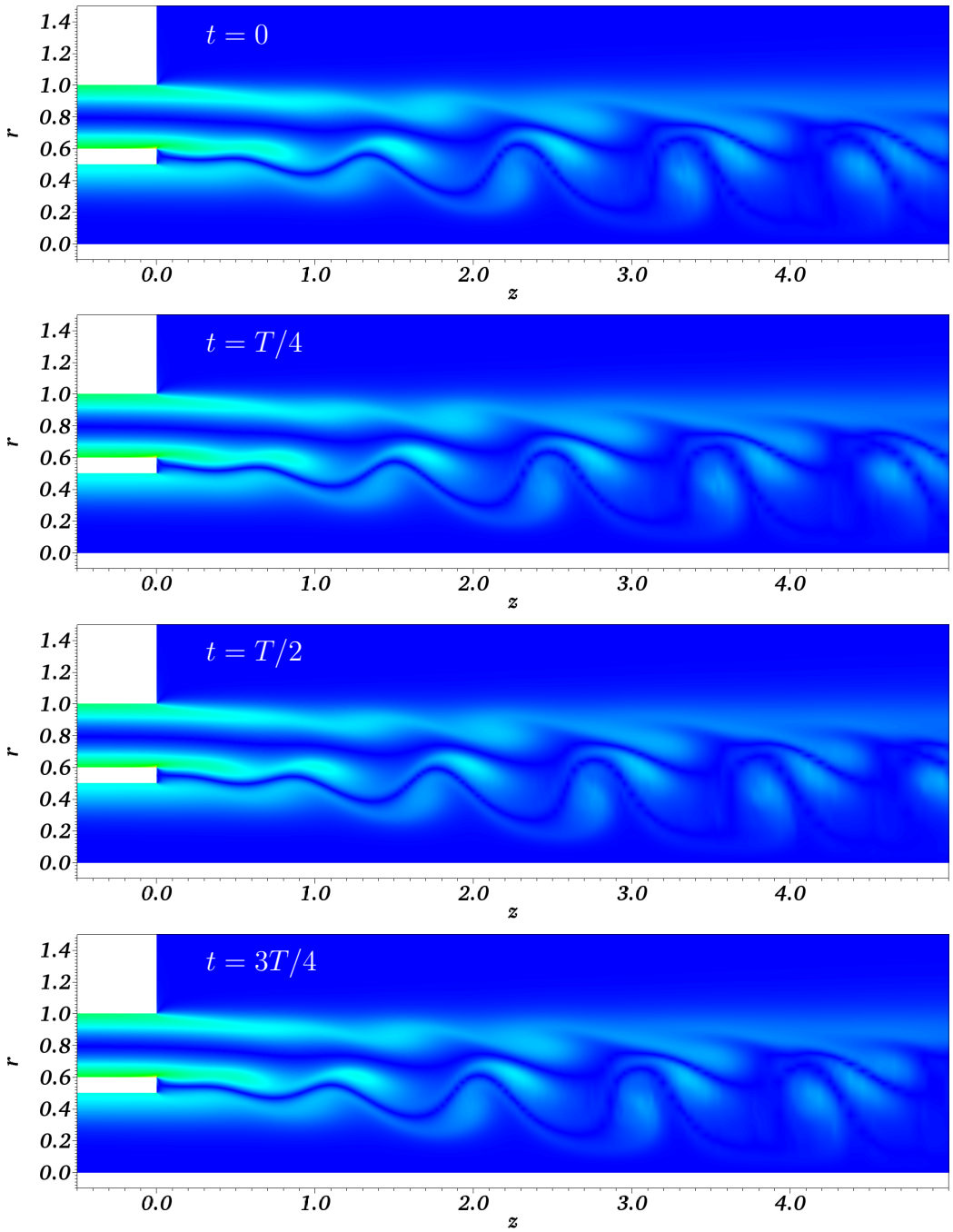

Figure 4.15 *Magnitude of the vorticity field during a shedding period.* $Re_i = 1500$, $r_u = 1$, *point* D_2 *in figure 4.5.*

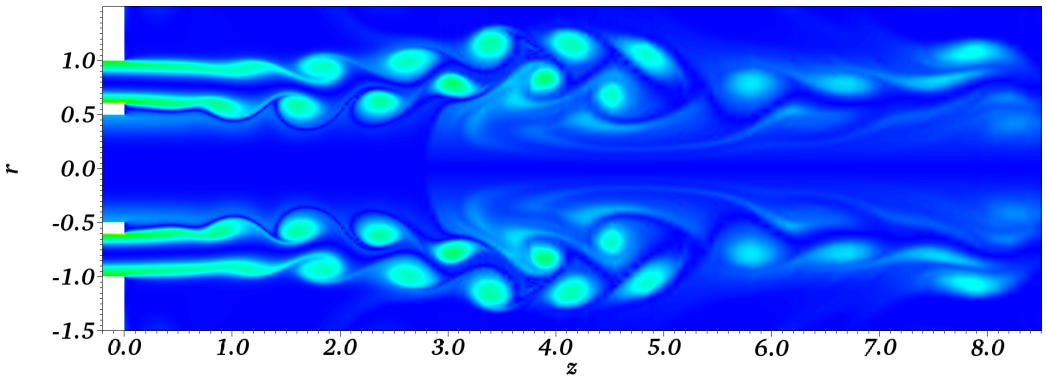

Figure 4.16 *Magnitude of the vorticity field, $Re_i = 1600$, $r_u = 2$, point D_4 in figure 4.5 A large recirculation bubble is observable at $z \approx 4$, the flow is believed to be non-axisymmetric in this regime. At the moment of writing, three-dimensional DNSs are still under way.*

4.8 Influence of domain truncation

To investigate the impact of the spatial extent of the computational domain on the results of the stability analysis, several studies have been performed with domain lengths ranging from $z_{\max} = 40$ to $z_{\max} = 160$, for domain heights ranging from $r_{\max} = 5$ to $r_{\max} = 5$ and for pipe lengths ranging from $z_{\mathrm{i}} = 5$ to $z_{\mathrm{i}} = 15$. The size of the elements has been kept constant across all the meshes used for these studies. Meshes with $z_{\max} \geq 120$ have proved critical: the values of transient energy amplification computed using these domains were not in line with the convergence trend shown by smaller meshes. The cause of this behaviour is still unclear.

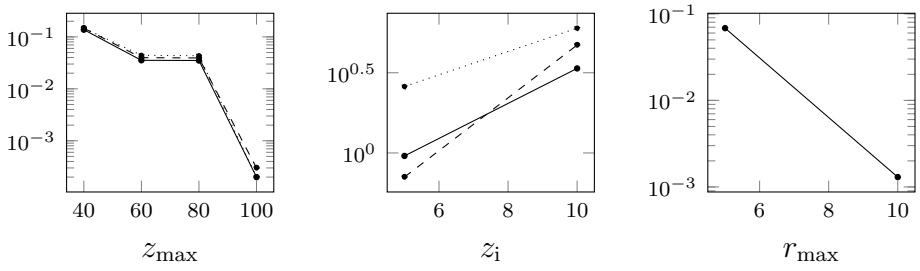

Figure 4.17 *Convergence of transient growth computations with respect to domain size. Points indicate the computed values. Percentage errors are shown relative to the calculations using $z_{max} = 120$, $z_i = 15$ and $r_{max} = 15$. The optimal growth is computed for $\tau = 12$ (continuous lines), $\tau = 16$ (dashed lines), $\tau = 20$ (dotted lines); $Re_i = 1\,000$, $r_u = 1$.*

The length of the pipes, z_{i}, is mainly relevant, as explained in [4], for the correct computation of the optimal perturbations but is also of fundamental importance to calculate the adjoint eigenvalues and thus the structural sensitivity parameter. The value of $G_{\max}(\tau)$ results only marginally dependent on $r_{\max}$, since the perturbations are confined within the two jets. The domain length and pipe lengths, instead, play a relevant role, especially for large τ. The convergence results are depicted in figure 4.17

In figure 4.18 the dependence of branch b_2 of the eigenspectrum on the length of the domain is depicted. The direct eigenvectors corresponding to this branch reach their maximum amplitude in the proximity of the outflow boundary, and do not appear to represent a physical feature of the flow. A strong dependence of these modes on the position of the boundary is therefore to be expected.

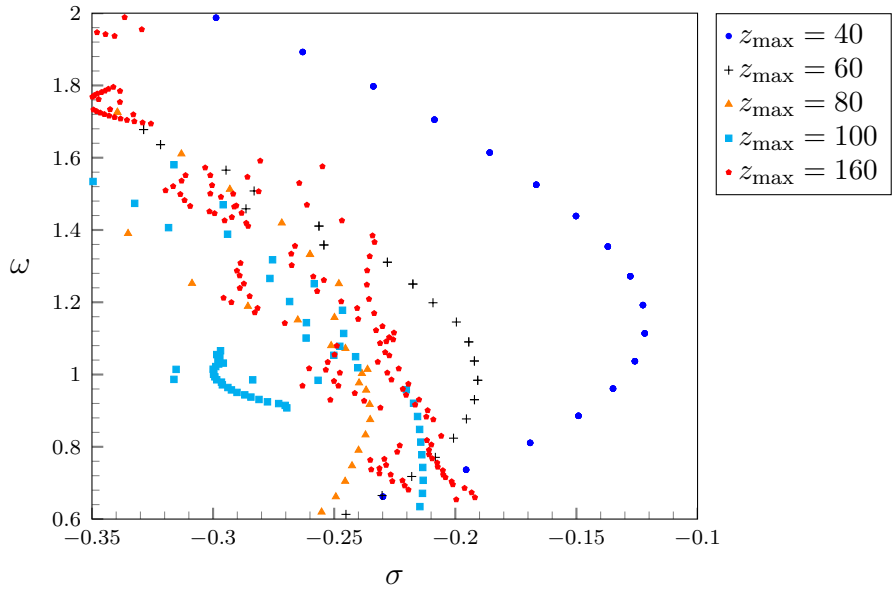

Figure 4.18 *Eigenvalues in the branch b_2 of figure 4.3 computed for different domain lengths. The eigenspectrum has also been computed for $z_{max} = 120, 140$ but calculations are not reported here for clarity. $Re_i = 1\,000$, $r_u = 1$.*

Nevertheless, when employing meshes with $z_{\max} > 100$, this branch seems to eventually converge to an approximately stable position, and becomes unstable when increasing the velocity ratio (as shown in figure 4.8). For this reason, a structural sensitivity analysis has been performed on the least stable eigenvalues of branch b_2. The results have proved inconclusive, as even the peaks of the structural sensitivity parameter result domain-dependent, see figure 4.19.

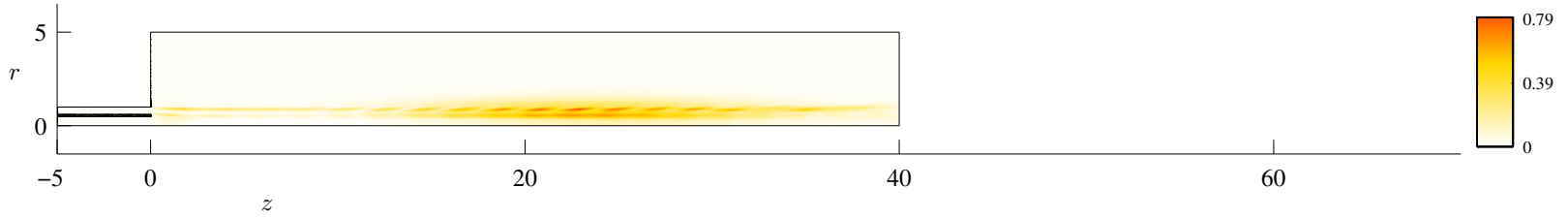

(a) $z_{max} = 40$.

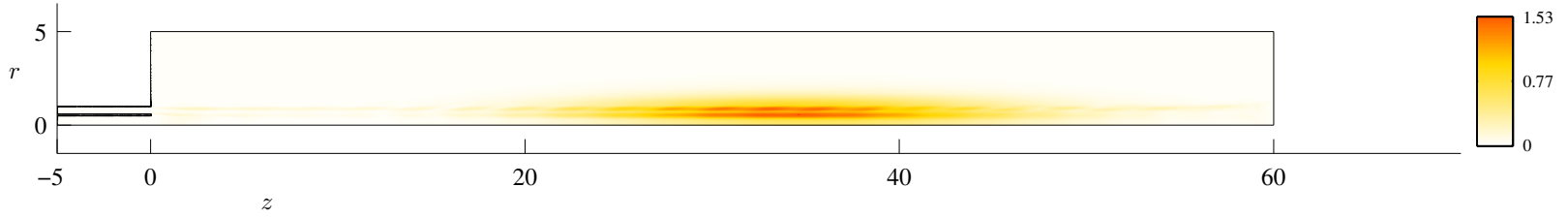

(b) $z_{max} = 60$.

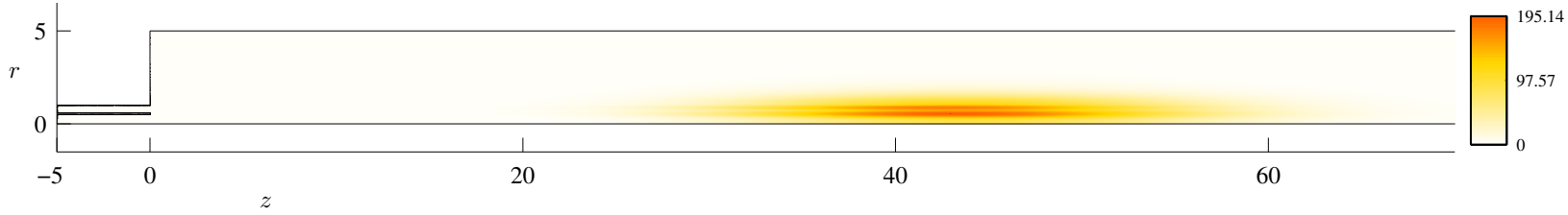

(c) $z_{max} = 100$.

Figure 4.19 *Structural sensitivity of the least stable eigenvalue of the useless branch.*

Summary and conclusions

Starting from a Finite Element solver designed for the computation of the base flow, the necessary tools for a global linear stability analysis have been developed and thoroughly validated.

The stability properties of two incompressible, coaxial jets have been numerically investigated for the first time, using the code developed during this thesis work. In addition, direct numerical simulations have been performed to compare the results attained by the linear stability analysis with the nonlinear behaviour of the flow, obtaining encouraging results. The dynamics of the jets have been studied as a function of two of the main parameters describing the flow, *i.e.*, the Reynolds number based on the inner jet Re_i, and the velocity ratio between the two streams r_u.

The geometry used during the investigation was characterized by the presence of a rectangular duct wall separating the two streams. The neutral curve corresponding to a Hopf bifurcation has been traced in the $\mathrm{Re}_i - r_u$ plane; when crossing this curve the real part of a pair of complex-conjugate eigenvalues becomes positive and the flow becomes linearly unstable. DNSs confirm the values of the parameters necessary for the instability and present flow patterns in agreement with those predicted by the modal stability analysis.

In the unstable regime, for $r_u = 1$, a von Kármán vortex-street is originated in the wake of the separation wall. In this condition the direct and adjoint critical eigenvectors are similar to those observed in the wake of a bluff body. On the other hand, when the velocity ratio is increased the vortex dynamics resembles more and more the one produced by a Kelvin–Helmoltz instability. This phenomenon, which is clearly observable in the DNS, results in a change of the shape of the unstable eigenmode and in a modification of the spatial

distribution of the structural sensitivity parameter. These flow patterns are also observed in experiments (see, *e.g.* [38]), however, the Reynolds number being higher, a direct comparison of the frequencies involved cannot be made.

A structural sensitivity analysis has been carried out to locate the region in the flowfield where the instability mechanism, associated with the critical eigenmode, acts. The results show that the 'wavemaker' is located near the rectangular separation wall, in the recirculation region, similarly to what happens for bluff bodies. Differently from symmetrical flow configurations, the maximum of the structural sensitivity parameter is biased towards the faster streaming jet, indicating the leading role of the fast shear layer in the instability mechanism. When the velocity ratio is raised above $r_u = 1.5$, the value of the structural sensitivity parameter increases in the inner shear layer, highlighting a modification of the region where the 'wavemaker' is located.

In addition, the results show that considerable transient growth may occur in the subcritical regime, amplifying the kinetic energy of perturbations by up to twelve orders of magnitude. In the $r_u = 1$ regime, the time evolution of the optimal perturbation results in a spatial pattern which resembles that of a von Kármán vortex-street. However, the lack of experiments at low Reynolds numbers and the lack of time to investigate the effect of optimal perturbations on the nonlinear flow prevents us from drawing conclusions on whether jets are unstable before the onset of a global mode.

The present research has been completed by a study on the influence of domain truncation, a relevant issue in weakly nonparallel flows. The requirement of a proper modelling of the pipes generating the flow has been highlighted in the context of modal and nonmodal stability, and the location of the outflow boundary has proved to be critical for the eigenspectrum and for the computation of transient dynamics at large time horizons.

Finally, a comment on the relevance of three-dimensional perturbations for the instability of the flow is in order. Several authors [8, 30] have observed experimentally the axisymmetry of the flow in the near field of the nozzles even at high Reynolds numbers, but no measures have been performed in the low Reynolds number regime. At the moment of writing, fully three-dimensional DNSs, performed in order to investigate the axisymmetric nature of the nonlinear flow, are still under way,

The computed results give new insight into the dynamics of incompressible, viscous, coaxial jets, but do not conclude the investigation. Several other points should be considered to fully understand the behaviour of coaxial jets for low Reynolds numbers. Possible developments include:

- the analysis of the nonlinear response to optimal perturbations and the computation of nonlinear optimal perturbations for subcritical values

of the parameters. This investigation would shed new light onto the linearly stable regime which would also need be observed experimentally,

- the study of the non-isothermal, compressible flow, which would highlight the impact of pressure waves and of temperature and density differences between the two jets on their stability properties,
- the extension of the present investigation to three-dimensional perturbations which would highlight the importance of such perturbations with respect to axisymmetric perturbations,
- an extension of the present investigation to the high velocity ratio regime.

APPENDIX A

Estratto in italiano

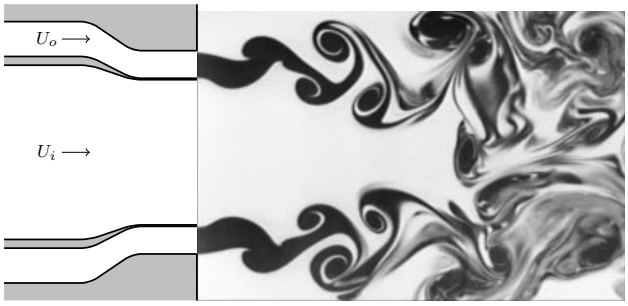

Figura A.1 *Visualizzazione tratta da [46]. Il getto anulare è inseminato con colorante fluorescente, il rapporto di velocità è* $r_u = U_o/U_i = 4$ *e il numero di Reynolds basato sul getto interno è* $Re_i = 1\,000$.

Introduzione Una coppia di getti coassiali viene formata dall'unione di due correnti: una interna, prodotta da un tubo di sezione circolare di diametro D_i e dotata di velocità U_i, e da una corrente esterna prodotta da un tubo a sezione di corona circolare di diametri interno $D_{o,1}$ ed esterno $D_{o,2}$, e dotata di velocità U_o.

I getti coassiali sono spesso utilizzati in applicazioni industriali in quanto costituiscono un sistema efficace per il mescolamento di due fluidi. Alcuni esempi sono il miscelamento di aria e combustibile nei motori a getto e la formazione di spray ad alta velocità. La geometria a getti coassiali è infatti sfruttata per la sua capacità di destabilizzare, frammentare e miscelare il

getto centrale con quello anulare [46]. Inoltre, grande interesse in campo aeronautico è volto all'efficace attenuazione del rumore ottenibile grazie a getti coassiali, le cui proprietà di smorzamento delle onde acustiche sono note da diversi anni (vedere, *e.g.* [49]).

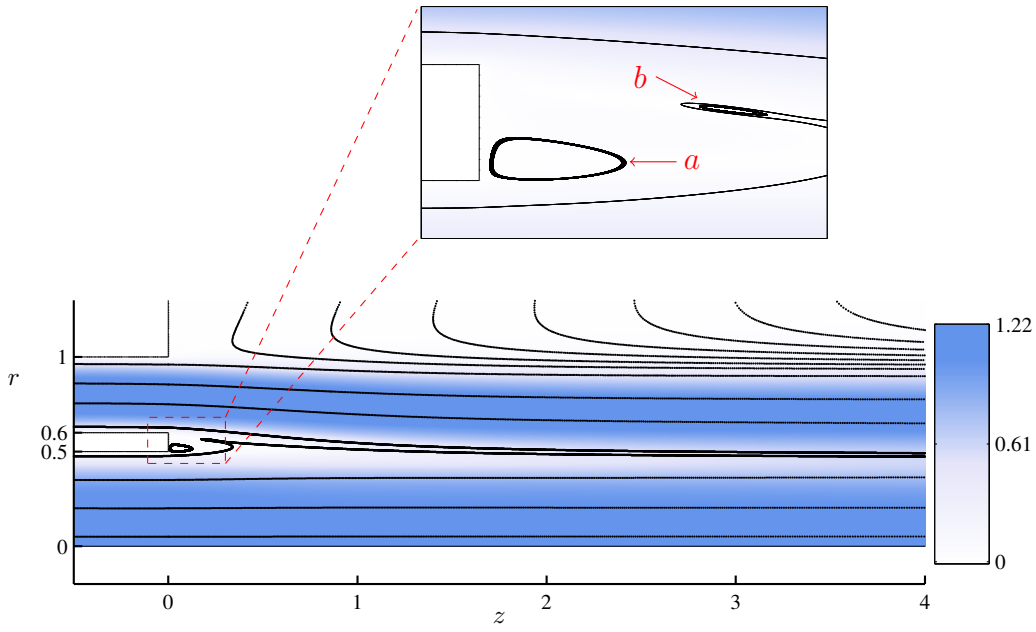

Figura A.2 *Modulo della velocità e linee di corrente del flusso base.* $Re_i = 2\,000$, $r_u = 1$. *Due anelli vorticosi sono evidenziati con* a *e* b. *Si può anche osservare il* trascinamento *di fluido dalla regione esterna ai getti verso la regione interna.*

È stato ipotizzato [31, 19] che il rumore generato dai getti coassiali sia legato alla dinamica delle strutture vorticose di grande scala, formatesi a causa dell'instabilità degli shear layers. È inoltre noto (vedere, *e.s.* [27]) che il mescolamento di grande scala è controllato da strutture coerenti di dimensioni rilevanti. È quindi importante capire nel dettaglio le dinamiche di queste strutture, anche in configurazioni semplici (*i.e.*, densità costante e bassi numeri di Reynolds).

I getti coassiali sono anche un esempio di corrente relativamente semplice ma governata da un numero non indifferente di parametri, permettono quindi uno studio del principio della turbolenza tramite una descrizione non unicamente basata sul numero di Reynolds. Le caratteristiche di stabilità di questa classe di correnti sono state studiate sperimentalmente da diversi autori [3, 37, 38, 39] in varie configurazioni geometriche e per diversi valori dei parametri menzionati. Tali autori hanno concluso, sia tramite esperimenti sia sviluppi analitici nell'approssimazione parallela e non viscosa [26, 41], che,

quando gli ugelli sono separati da un divisorio di geometria rettangolare, i getti presentano una regione di instabilità assoluta immediatamente a valle del divisorio.

Uno degli obiettivi di questa tesi è la verifica di questa affermazione e la caratterizzazione dei getti dal punto di vista della stabilità. La corrente viene approssimata come incomprimibile ed assialsimmetrica, inoltre le proprietà fluidodinamiche dei due getti vengono considerate identiche, e la temperatura è assunta uniforme.

Gli strumenti utilizzati per l'analisi di stabilità sono stati implementati in un codice scritto in Fortran 2003 e C e le operazioni più costose dal punto di vista computazionale sono state eseguite in parallelo utilizzando le librerie MPI ed OpenMP.

Getti coassiali Le caratteristiche di stabilità della corrente sono state studiate per la prima volta in questo lavoro per via numerica seguendo diversi approcci. La dinamica dei getti è stata studiata in funzione di due dei più importanti parametri che ne determinano il comportamento, *i.e.*, il numero di Reynolds ed il rapporto di velocità.

I risultati mostrano che un'ampia crescita transitoria può aver luogo nel regime subcritico, l'energia cinetica delle perturbazioni, infatti, viene amplificata di fattori che raggiungono 10^{12} per un numero di Reynolds pari a 1 000. La struttura delle perturbazioni assume la forma di una scia di von Kármán quando il rapporto delle velocità in ingresso è $r_u = 1$.

Tuttavia, la mancanza di esperimenti a bassi numeri di Reynolds e la mancanza di tempo per investigare l'effetto delle perturbazioni ottime sulla corrente non lineare, impedisce di concludere che i getti siano instabili prima dell'instabilità lineare.

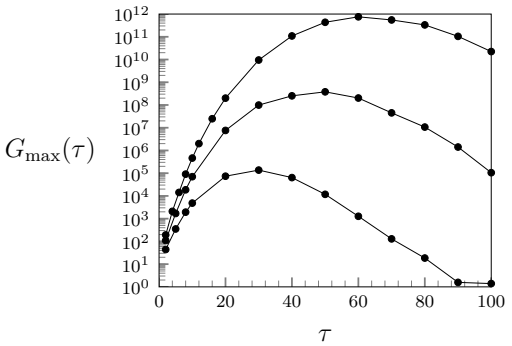

Figura A.3 *Crescita transitoria ottima a numeri di Reynolds* $Re_i = 500, 750, 1\,000$. *Il rapporto di velocità è* $r_u = 1$.

A fianco dell'analisi della crescita transitoria è stata tracciata la curva neutra corrispondente ad una biforcazione di Hopf nel piano $\mathrm{Re}_i - r_u$. Attraversando questa curva la parte reale di due autovalori complessi coniugati diventa positiva e la corrente diventa linearmente instabile. Per $r_u = 1$ l'autovettore diretto e l'autovettore aggiunto associati all'autovalore marginalmente stabile presentano una struttura simile a quella osservata nella scia di un corpo tozzo. Quando il rapporto di velocità viene incrementato, invece, le strutture vorticose assumono un aspetto sempre più simile al campo di perturbazione associato a un'instabilità di Kelvin–Helmoltz. Questo fenomeno è confermato da una variazione della forma dell'autovettore critico, da una modifica della struttura spaziale del campo di sensitività strutturale, ed è chiaramente osservabile nelle DNS.

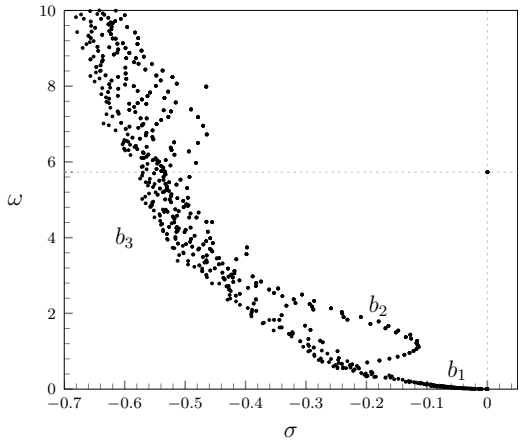

Figura A.4 *Spettro a $Re_i = 1\,420$ e $r_u = 1$ (punto A_1 in figura A.5. Le linee tratteggiate evidenziano un autovalore marginalmente stabile con $\omega_c = 5.728$, le etichette b_i indicano i principali gruppi di autovalori.*

È inoltre stata svolta un'analisi di sensitività strutturale con lo scopo di localizzare la regione del campo di moto in cui agisce il meccanismo di instabilità. I risultati mostrano che il 'wavemaker' si trova in prossimità del divisorio di geometria rettangolare, in particolare, nella regione ove il flusso base presenta degli anelli vorticosi, similmente a quanto osservato per i corpi tozzi in presenza di bolle di ricircolo. A differenza delle correnti simmetriche, però, il massimo del parametro di sensitività strutturale è spostato verso il getto dotato di maggior velocità, indicando una maggior rilevanza, per il meccanismo di instabilità, dello shear layer dotato di maggior velocità. Quando il rapporto di velocità supera la soglia di $r_u = 1.5$, il valore del parametro di sensitività strutturale aumenta notevolmente nello shear layer interno, evidenziando una modifica della regione in cui ha sede il 'wavemaker'.

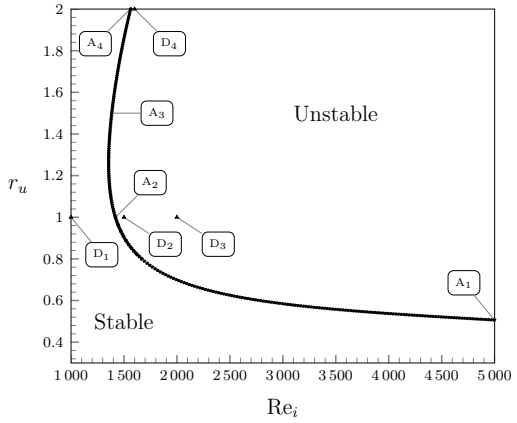

Figura A.5 *Curva neutra nel piano $Re_i - r_u$. I punti (ove distinguibili) corrispondono ai valori calcolati. Le etichette A_i evidenziano i valori a cui sono stati calcolati i risultati principali presentati in questa tesi. I triangoli D_i indicano i punti in cui sono state eseguite le DNS.*

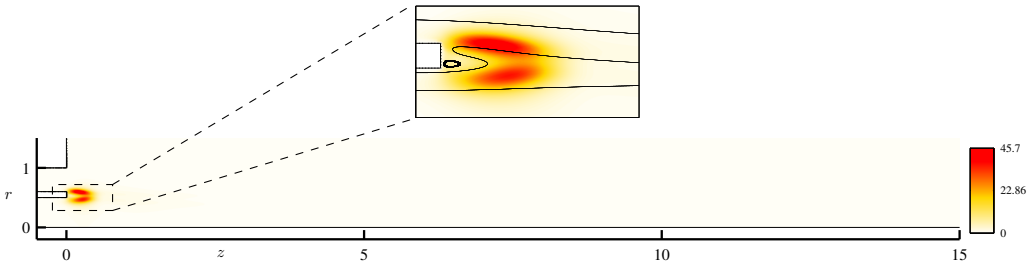

(a) $Re_i = 1\,420$, $r_u = 1$. *Punto A_2 in fig. A.5.*

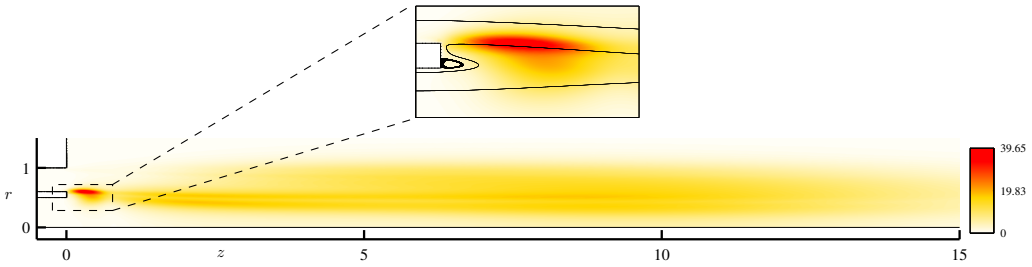

(b) $Re_i = 1\,559$, $r_u = 2$. *Punto A_4 in fig. A.5.*

Figura A.6 *Sensitività strutturale dell'autovalore marginalmente stabile a retroazioni localizzate in spazio.*

Questa ricerca è stata affiancata da uno studio sull'influenza del troncamento del dominio numerico, un aspetto importante nelle correnti debolmente non parallele. Lo studio ha evidenziato la necessità di un'appropriata modellazione dei condotti che generano i getti, sia nel contesto della stabilità modale sia in quello della stabilità non modale, e la posizione del bordo d'uscita si è rivelata critica sia nei riguardi dello spettro degli autovalori sia per quanto concerne il calcolo delle perturbazioni ottime per ampi orizzonti temporali.

Infine è necessario un commento sull'importanza di un'analisi del comportamento in presenza di perturbazioni tridimensionali. Diversi autori [8, 30] hanno osservato sperimentalmente un comportamento assialsimmetrico della corrente nella prossimità degli ugelli, anche a numeri di Reynlds elevati. Per verificare la validità dei risultati ottenuti nel caso assialsimmetrico, sono state lanciate delle DNS tridimensionali estremamente onerose dal punto di vista computazionale, sfortunatamente, al momento della stesura di questa tesi, i risultati non sono ancora stati ottenuti.

Bibliography

[1] R. Amestoy, I. Duff, and J.-Y. L'Excellent. Multifrontal parallel distributed symmetric and unsymmetric solvers. *Comput. Methods Appl. Math.*, 184:501–520, 2000.

[2] F. Auteri, M. Biava, and L. Quartapelle. Navier–Stokes Spectral Solver in a Finite Cylinder. *Comm. in Comput. Phys.*, 8:663–689, 2010.

[3] G. Buresti, P. Petagna, and A. Talamelli. Experimental characterization of the velocity field of a coaxial jet configuration. *Exp. Therm. Fluid Science*, 9:135–146, 1994.

[4] C. D. Cantwell and D. Barkley. Computational study of subcritical response in flow past a circular cylinder. *Phys. Rev.*, 82, 2010.

[5] J.-M. Chomaz. Global Instabilities in Spatially Developing Flows: Non-Normality and Nonlinearity. *Annu. Rev. Fluid Mech.*, 37:357–392, 2005.

[6] S. W. Churchill. *Viscous Flows*. Butterworths, 1988.

[7] C. da Silva, G. Balarac, and O. Metais. Transition in high velocity ratio coaxial jets analysed from direct numerical simulations. *Journal of Turbulence*, 4, 2003.

[8] W. J. A. Dahm, E. F. Clifford, and G. Tryggvanson. Vortex structure and dynamics in the near field of a coaxial jet. *J. Fluid Mech.*, 241:371–402, 1992.

[9] O. Daube. Resolution of the 2D Navier–Stokes equations in velocity–vorticity form by means of an influence matrix technique. *J. Comput. Phys.*, 103:402–414, 1992.

[10] T. Djeridane. *Contribution à l'étude expérimentale de jets turbulents axisymétriques à densité variable*. PhD thesis, Aix-Marseille II, 1994.

[11] A. Ern and J.-L. Guermond. *Theory and Practice of Finite Elements*. Springer, 2004.

[12] M. P. Escudier. Observations of the flow produced in a cylindrical container by a rotating end wall. *Experiments in Fluids*, 2:189–196, 1984.

[13] G. Gallavotti. *Foundations of Fluid Mechanics*. Springer–Verlag, 2002.

[14] X. Garnaud, L. Lesshafft, P. J. Schmid, and P. Huerre. Modal and transient dynamics of jet flows. *Phys. Fluids*, 25, 2013.

[15] F. Giannetti and P. Luchini. Structural sensitivity of the first instability of the cylinder wake. *J. Fluid Mech.*, 581:167–197, 2007.

[16] V. Girault and P. A. Raviart. *Finite Element Methods for Navier–Stokes Equations*. Springer–Verlag, 1986.

[17] J. Guckenheimer and P. Holmes. *Nonlinear Oscillations, Dynamical Systems, and Bifurcations of Vector Fields*. Springer, 1983.

[18] P. Huerre and P. A. Monkewitz. Local and global instabilities in spatially developing flows. *Annu. Rev. Fluid Mech.*, 22:473–537, 1990.

[19] A. K. M. F. Hussain. Coherent Structures and Turbulence. *J. Fluid Mech.*, 173:303–356, 1986.

[20] N. W. M. Ko and A. S. H. Kwan. The initial region of subsonic coaxial jets. *J. Fluid Mech.*, 73:305–332, 1976.

[21] Y. A. Kuznetsov. *Elements of Applied Bifurcation Theory*. Springer–Verlag, 2004.

[22] A. S. H. Kwan and N. W. M. Ko. The initial region of subsonic coaxial jets. Part 2. *J. Fluid Mech.*, 82:237–287, 1977.

[23] R. B. Lehoucq, D. C. Sorensen, and C. Yang. ARPACK Users Guide: Solution of Large-Scale Eigenvalue Problems with Implicitly Restarted Arnoldi Methods. *SIAM*, 1998.

[24] L. Lesshafft, P. Huerre, and P. Sagaut. Frequency selection in globally unstable round jets. *Phys. Fluids*, 19, 2007.

[25] L. Lesshafft, P. Huerre, P. Sagaut, and M. Terracol. Nonlinear global modes in hot jets. *J. Fluid Mech.*, 554:393–409, 2006.

[26] A. Michalke. On the influence of a wake on the inviscid instability of a circular jet with external flow. *Eur. J. Mech.*, 12:579–595, 1993.

[27] S. B. Pope. *Turbulent Flows*. Cambridge University Press, 2000.

[28] J. O. Pralits, L. Brandt, and F. Giannetti. Instability and sensitivity of the flow around a rotating circular cylinder. *J. Fluid Mech.*, 650:513–536, 2010.

[29] L. Quartapelle and F. Auteri. *Fluidodinamica Iincomprimibile*. Casa Editrice Ambrosiana, 2013.

[30] H. Rehab, E. Villermaux, and E. J. Hopfinger. Flow regimes of large-velocity-ratio coaxial jets. *J. Fluid Mech.*, 345:357–381, 1997.

[31] A. Roshko. Structure of Turbulent Shear Flows: A New Look. *AIAA Journal*, 14, 1976.

[32] D. Ruelle and F. Takens. On the Nature of Turbulence. *Commun. math. Phys.*, 20:167–192, 1971.

[33] A. G. Salinger, N. M. Bou-Rabee, R. P. Pawlowski, E. D. Wilkes, E. A. Borroughs, L. R. B., and L. A. Romero. LOCA, Library Of Continuation Algorithms: Theory and Implementation Manual. *SAND*, 2002.

[34] H. Schlichting. *Boundary-Layer Theory*. McGraw–Hill, 1968.

[35] P. J. Schmid. Nonmodal Stability Theory. *Annu. Rev. Fluid Mech.*, 39:129–162, 2007.

[36] P. J. Schmid and D. S. Henningson. *Stability and Transition in Shear Flows*. Springer, 2001.

[37] A. Segalini. *Experimental analysis of coaxial jets: instability, flow and mixing characterization*. PhD thesis, Università di Bologna, 2010.

[38] A. Segalini and A. Talamelli. Experimental analysis of dominant instabilities in coaxial jets. *Phys. Fluids*, 23, 2011.

[39] A. Segalini and A. Talamelli. Main Instabilities of Coaxial Jets. *SPPHY*, 141:139–142, 2012.

[40] D. Sipp and A. Lebedev. Global stability of base and mean flows: a general approach and its applications to cylinder and open cavity flows. *J. Fluid Mech.*, 593:333–358, 2007.

[41] A. Talamelli and I. Gavarini. Linear stability characteristics of incompressible coaxial jets. *Flow Turb. Combust.*, 76:221–240, 2006.

[42] A. Talamelli, A. Segalini, R. Orl u, and G. Buresti. A note on the effect of the separation wall in the initial mixing of coaxial jets. *Exp. Fluids*, 54, 2013.

[43] R. Temam. *Navier–Stokes equations: theory and numerical analysis*. North-Holland Publishing Company, 1977.

[44] L. N. Trefethen and M. Embree. *Spectra and Pseudospectra. The Behavior of Nonnormal Matrices and Operators*. Princeton University Press, 2005.

[45] L. N. Trefethen, A. E. Trefethen, S. C. Reddy, and T. A. Driscoll. Hydrodynamic Stability Without Eigenvalues. *Science*, 261:578–584, 1993.

[46] E. Villermaux and H. Rehab. Mixing in coaxial jets. *J. Fluid Mech.*, 425:161–185, 2000.

[47] F. Waleffe. Hydrodynamic Stability and Turbulence: Beyond Transients to a Self-Sustaining Process. *Studies in Appl. Math.*, 95:319–343, 1995.

[48] F. Waleffe. Transition in shear flows: non-linear normality versus non-normal linearity. *Phys. Fluids*, 7:3060–3066, 1995.

[49] T. J. Williams, M. R. M. H. Ali, and J. S. Anderson. Noise and flow characteristics of coaxial jets. *J. Mech. Eng. Sci.*, 11:133–142, 1969.